論文 / 著書情報
Article / Book Information

題目(和文)	
Title(English)	Case studies on environmental evaluations of ground surface in paddy fields and deep subsurface under a coal mine
著者(和文)	TouchSamphors
Author(English)	Samphors Touch
出典(和文)	学位:博士（学術）, 学位授与機関:東京工業大学, 報告番号:甲第9899号, 授与年月日:2015年3月26日, 学位の種別:課程博士, 審査員:竹村　次朗,大即　信明,日野出　洋文,高橋　章浩,阿部　直也,ﾃｨﾗﾎﾟﾝ
Citation(English)	Degree:, Conferring organization: Tokyo Institute of Technology, Report number:甲第9899号, Conferred date:2015/3/26, Degree Type:Course doctor, Examiner:,,,,,
学位種別(和文)	博士論文
Type(English)	Doctoral Thesis

Case studies on environmental evaluations of ground surface in paddy fields and deep subsurface under a coal mine

Samphors Touch

(Abstract)

Problem associated with soil salinity in paddy field and risk evaluation against floor heaving of deep subsurface under a coal mine are the global environmental problems, which have drawn much attention from many researchers, organizations, and local government. In northeastern Thailand, soil salinity is the most widespread land degradation problem that reduces crop yields and agricultural productivity. This study aims to search the significant bands of vegetation indices that can indicate the relationships between electrical conductivity of soil and field hyperspectral reflectance of rice. In Mae Moh lignite mine, the control of groundwater pressure in deep-seated aquifers with high elevation becomes important for stability assessment against floor heave. Therefore, the 3D groundwater modeling is needed to construct in order to understand the behavior of groundwater and establish the rational dewatering program from the aquifer to reduce adverse groundwater pressure for the safe excavation with minimum impact on the surrounding environment.

For the evaluation of the soil salinity using remote sensing, the field investigations of various paddy fields in northeastern Thailand were carried out in late November 2010 during the ripening season just before harvest in an attempt to realise the applications of

the field hyperspectral technique for monitoring the spread of saline soils and estimation of the effects of soil salinity on rice plants. Jasmine rice and glutinous rice were two different rice species selected for this study. Rice plant investigations were conducted by collecting data on crop length, panicle length, canopy openness, leaf area index, and digital photos of plant conditions from each site. The statistical analyzes revealed that the changes in soil EC were significantly sensitive to the ripening stages of both jasmine rice and glutinous rice planted at different levels of soil salinity.

For the evaluation of groundwater environment of open pit mine, the Mae Moh mine, one of the largest open-pit mines in the region where deposits cover an area of more than 38 km^2, was selected as the study area. The current deepest level of pit is about 300 meters in the northeast mine area, while the final depth will be 490 meters at the end of production. Due to a huge volume of overburden excavation of about 60-80 million cubic meters per year, many engineering problems caused by the deep open-cut have been reported and handled. The critical areas were determined by calculation for safety factor by weight-pressure balance. The numerical method used for solving the groundwater flow equations was the finite difference method. The model prediction is for 8 years (2007 to 2018). Minimum groundwater discharge rate required for safety factor is greater than 1. In conclusion, it is required that at least 12,000 cum. of water must be extracted from 3 wells each day for 8 years to control the groundwater piezometric head down to +200 m above the mean sea level.

This work is dedicated to my family, without whose love and support, I could never have been attempted, much less completed.

Acknowledgements

I am deeply indebted to many people who have kindly supported me from the beginning to the end of my studies and research.

Foremost, I would like to express my sincere gratitude to my academic advisor Associate Professor Dr. Jiro TAKEMURA and my former academic advisor Associate Professor Thirapong PIPATPONGSA, who, despite their heavy workload, spent their valuable time for supporting, encouraging and inspiring me during academic years, provided research guidance which plays a vital role in the completion of this dissertation. Without them, I would not be able to achieve this work.

Besides my advisor, I also would like to thank Professor Dr. Nobuaki OTSUKI, Professor Dr. Hirofumi HINODE, Professor Dr. Akihiro TAKAHASHI and Associate Professor Dr. Naoya ABE, my thesis evaluation committee, for their time reviewing my work, their important comments, their constructive advices and opinions which provide me interesting way to improve the contents of the thesis.

Additionally, my cordial appreciation goes to colleagues and friends, especially all members in Thirapong Lab, to Mr. Pornchai PONGPANLARP, and to the Electricity Generating Authority of Thailand (EGAT) who have provided assistances relating to research's activities.

Similarly, I am also thankful to Assistant Professor Dr. Takeyama and Prof. Dr. Masaki KITAZUME for his precious time, his kind help, his invaluable guidance, and his generous support during coursework and as well as my research.

I owe my great thank to all professors and staffs of Tokyo Tech for their invaluable knowledge gave to me, their treatment and encouragement which have made Tokyo Tech my home.

I would like to acknowledge the scholarship from the AUN/SEED-Net project with support from Japan International cooperation Agency (JICA), which offers me the honorable opportunity to pursue my postgraduate study in Japan.

Finally, I would like to express my deepest appreciation to my parents, my brother and sisters for their endless love, encouragement and support, which gave me idea, motivation, strength and power to conquer any obstacle.

TABLE OF CONTENTS

LIST OF FIGURES

LIST OF TABLES

List of Symbols

ASD	Analytical spectral devices
CAI	Cellulose absorption index
EC	Electrical conductivity
EGAT	Electricity Generating Authority of Thailand
GIS	Geographical information systems
HL	Huai Luang Formation
HK	Huai King Formation
HRS	Hyperspectral remote sensing
LiDAR	Light detection and ranging
LDD	Land development department, the Ministry of Agriculture and Cooperative of Thailand
MIR	Mid infrared
MODIS	Moderate-resolution Imaging Spectroradiometer
MPA	Multipurpose analyzer
MRS	Multiresolution image segmentation
MTVI	Modified transformed vegetation index
NDSI	Normalized difference spectral index
NDVI	Normalized difference vegetation index
NDWI	Normalized difference water index
NIR	Near infrared
NK	Na Khaem Formation
NPCI	Normalized pigment chlorophyll index
NPQI	Normalized phaeophytinization index
NW	Northwest
OB	Overburden
OSAVI	Optimal soil-adjusted vegetation index
PRI	Photochemical reflectance index
SLR	Simple linear regression
RADAR	Radio detection and ranging
RMSE	Root mean squares error
SD	Standard deviation

SDE	Standard deviation of the error distribution
SDR	Second derivative reflectance
SE	Southeast
SEP	Standard error of prediction
SGSD	Slope gradient standard deviation
SPOT	Systeme Pour l'Observation de la Terre
SW	southwest
SWIR	Shortwave infrared
UB	Underburden
WI	Water index
γ_s	Unit weight of
γ_w	Unit weight of water
k_h	Horizontal hydraulic conductivity
k_v	Vertical hydraulic conductivity
S_s	Specific storage
S_y	Specific yield

CHAPTER 1 INTRODUCTION

1.1. Background and problem statements

Environmental sustainability is a core issue for world development. The secure sufficient quality in the short and the long term of ecosystems, natural resources, the plant diversity, animal species, and the human living environment are very important (Vlek and Steg 2007). Impact of human activities (electric power industry, industry, mining and mineral processing, agriculture and forestry) and natural processes (geological, hydrological, and biological process) are the main causes of environmental problems. The global character of some serious environmental problems can be identified (Hoel 1991). There are many kinds of environmental problem which have drawn much attention from many researchers, organizations, institutes, and local governments such as climate change, environmental degradation, overpopulation, pollution, land degradation, and groundwater problem. Among environmental problems, this research aims to investigate environmental evaluations of soil salinity and groundwater behavior in deep subsurface under a coal mine. The common environmental problems of this research are soil erosion, soil acidification, and buildup of dangerous chemicals, etc.

1.1.1. Soil salinity

Soil salinity is a global environmental problem and the most widespread land degradation problem (Eswaran et al. 2001). Soil salinity refers to the accumulation of salt in the soil especially on the surface or near-surface; principally chlorides, calcium, magnesium, sulphates, and carbonates of sodium (Tanji 2002). The excessive salt concentrations have detrimentally influenced the soil's chemical and physical properties (Ramoliya et al. 2006) and have hastened land degradation phenomena that reduce crop yields together with agricultural productivity (Boyer 1982). Salinity problem mostly take place in arid and semiarid regions, where precipitation is too low to maintain a regular percolation of rainwater through the soil. The soil salinization is classified into primary (natural processes) and secondary (human activities) salinization, which respectively affect 955 and 77 million hectares(Metternicht and Zinck 2003). In

Southeast Asia, 5.8 million hectares of land areas are harmed by soil salinity, one-quarter of which are located in Thailand, represented 2.7 percent of the country's land area (Shrestha 2006) as presented in Figure 1.1. The food productivity demand is very high due to rapidly increasing population, therefore, the effective agriculture practice is promoted. Results of poor agricultural management can be leaded to accelerate salinization process. Thus, timely detection of salinization, assessment of its effect and the extent, is vital (Farifteh et al. 2006).

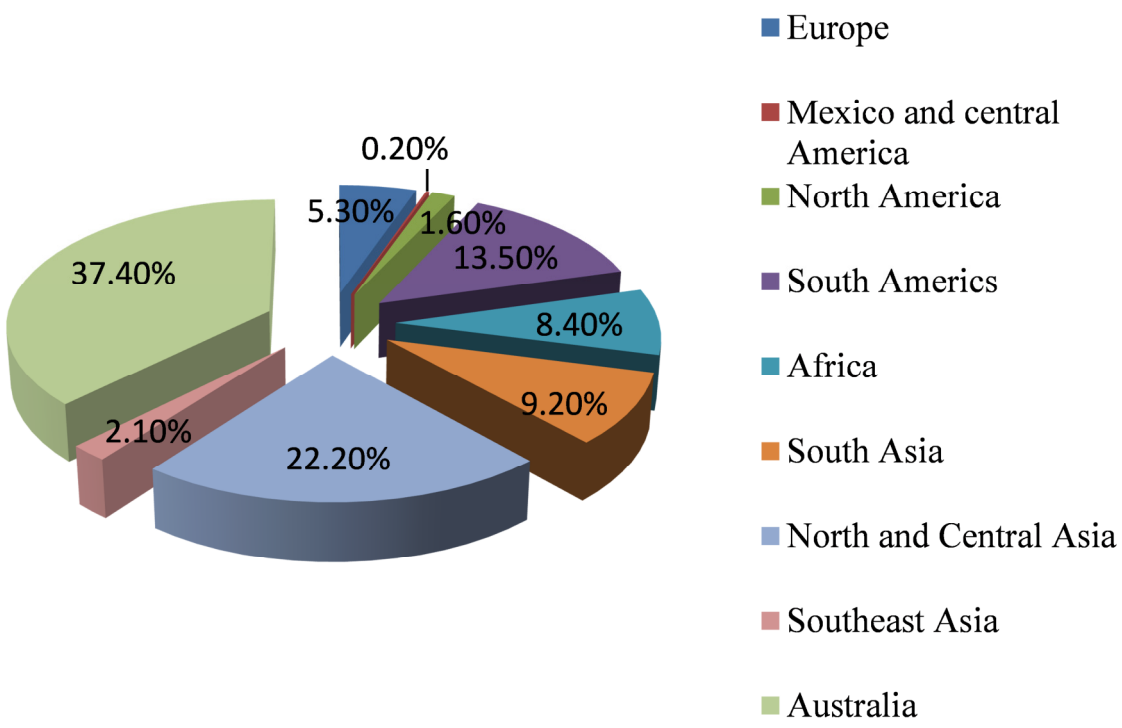

Figure 1.1 The extent of salt-affected soils in the world adopted (Szabolcs 1994)

1.1.2. Environmental problems in open pit mining

Global energy consumption growth has continued which is not good for the environment as presented in Figure 1.2. Currently, more than 85% of the world's energy consumptions are met through fossil fuels such as coal, oil and natural gas. As predicted, the demand of world energy will be expanded by 45% between now and 2030 as an average rate of increase of 1.6% per year, presented more than a third of the overall rise is coal resources. The speedily growing energy use has already become a major concern over supply difficulties, exhaustion of energy resources and heavy

environmental impacts (Pérez-Lombard et al. 2008). In mining, deep excavation is needed in order to get sufficient energy resources. Problems associated the mining operation in deep level is floor heave influenced by groundwater and other environmental concerns. The groundwater flow in huge mining area is very complex because of geological condition in the deep subsurface. The topology of the pit area might be changed from time to time. The control of groundwater pressure in deep-seated aquifers with high elevation becomes important for stability assessment. In addition, the potential of increasing heavy mental in particular arsenic has also become as one of the main environmental concern. For this reason, the effective dewatering plan is needed to investigate in order to secure the excavation process for long term usage.

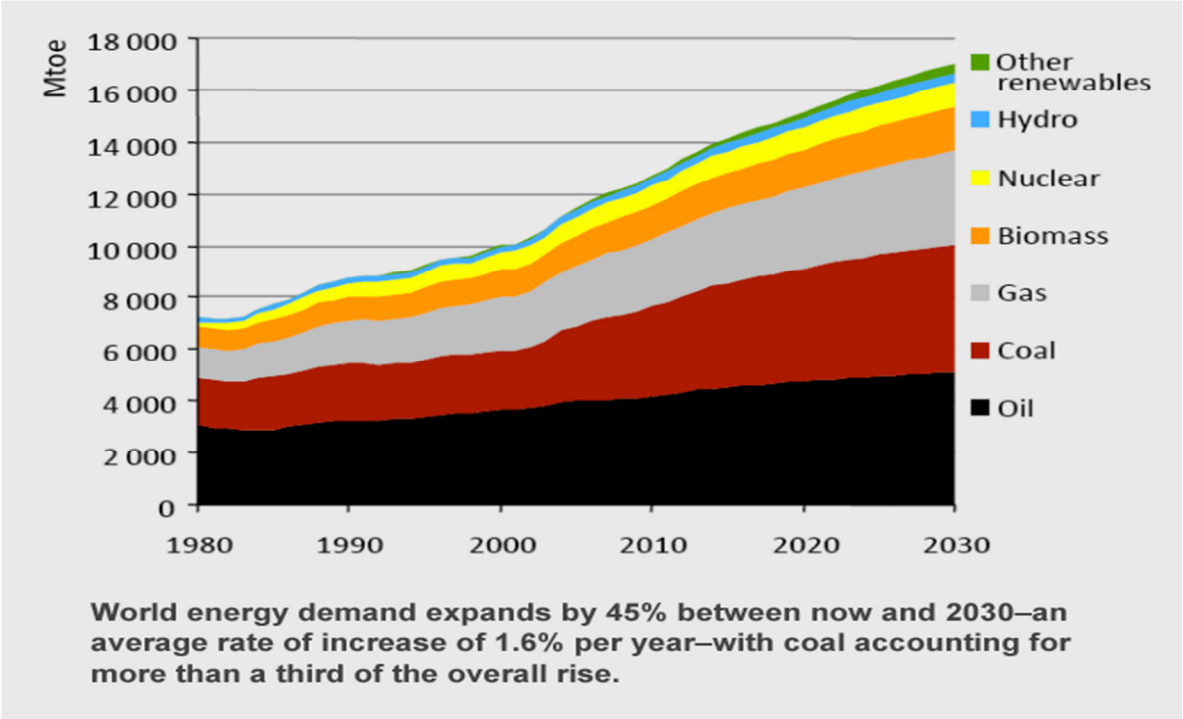

Figure 1.2 Global energy consumption from 1980 to 2030 (expected)

(Source: EIA, World Energy Outlook 2009)

1.2. Objectives and scope of the study

1.2.1. Soil salinity

This study aims to investigate whether salt stress in the rice can be detected by field reflectance or not during repining stage just before harvest, and evaluate cost-effective

methods for enhanced monitoring of soil salinity in the paddy field at early stage. To achieve the goal, the soil salinity analysis using remote sensing technique was examined. The electrical conductivity (EC) of soil is selected as the salinity indicator while field hyperspectral technique is chosen for spectral reflectance measurement. The results of this study might be useful for those who are working in the fields of remote sensing and crop science for monitoring the spread of saline soils and estimation of the effects of soil salinity on rice plants.

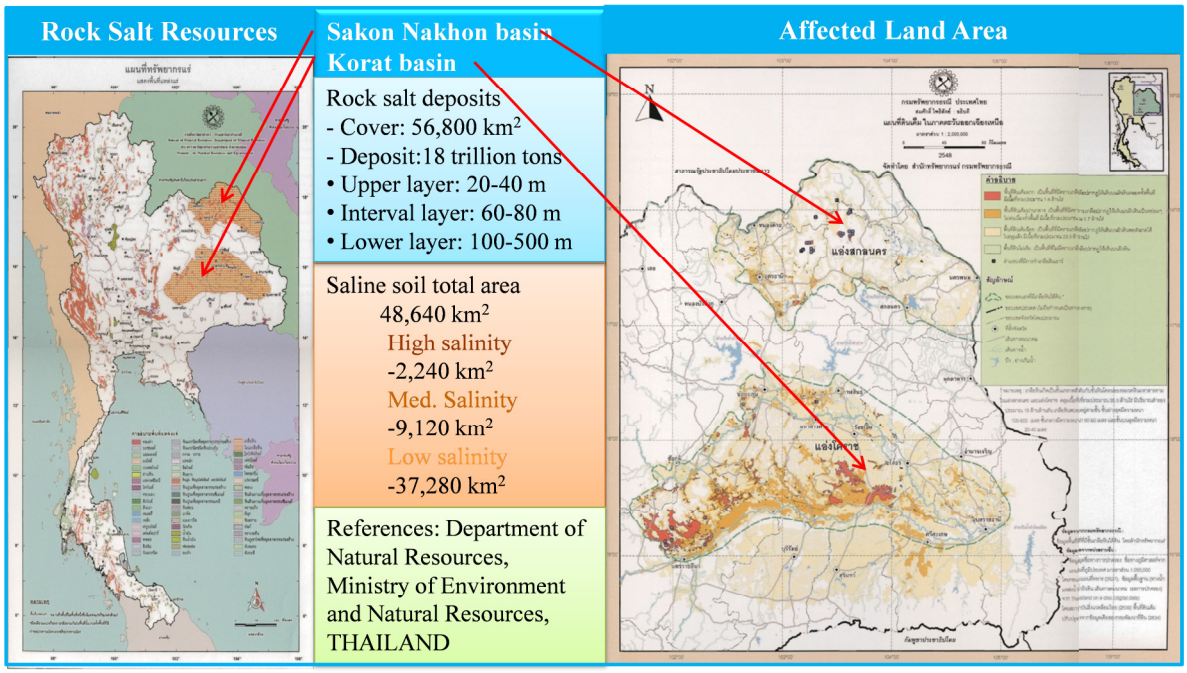

Figure1.3 Spread of soil salinity in Thailand (Referenced from Department of Natural Resources, Ministry of Environment and Natural Resources, Thailand).

According to various maps and information from Thai authorities, it is reported that the saline soil affected land area is 48640 km^2 from a total area of Thailand 513100 km^2; whereas, the areas that suffered from high, medium and low salinity are 2240, 9120 and 37280 km^2 respectively. Most of the affected area, which leads to unsatisfactory agricultural utilization, is located in the northeastern part of Thailand as shown in Figure1.3 where rock salt is deposited in the Khorat and Sakon Nakhon basins. The majority of the population depends on agriculture in this region, but it has relatively very low crop yield productivity if compared to other regions due to its low soil fertility.

One of the reasons for such low productivity is soil salinity. It is thus a matter of concern that salinity problem should be managed and controlled in the area to ensure sustainable agricultural productivity. Hence, the rapid monitoring of the spread of soil salinity and estimation of the effects of soil salinity on rice plants is important. Because rice cultivars (jasmine rice and glutinous rice) which are planted as the major rice crops are suffered from soil salinity in the northeastern part, the paddy field has been selected for field hyperspectral experiments in this study as presented in Figure1.4.

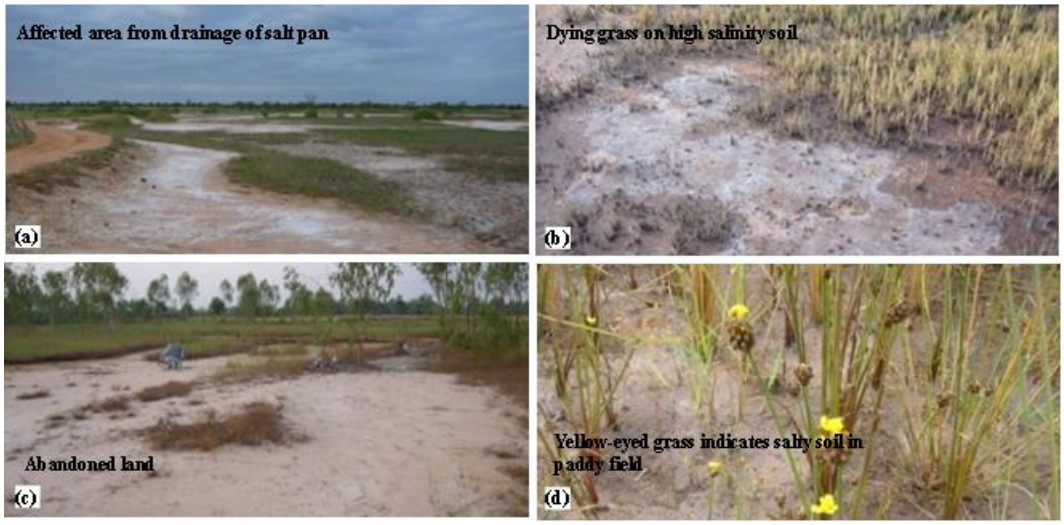

Figure1.4 Site condition in northeastern Thailand: (a) Kham Thale, Nakhon Ratchasima Province, (b) Ban Phai, Khon Kaen Province, (c) Phang Khon, Sakon Nakhon Province, and (d) Ban Dung, Udon Thani Province.

Actually, rice spectral responses are affected by many factors such as plant features, soil properties, and climate, or even soil background; therefore, the relationship of soil EC to spectral characteristics could not be definitely isolated in this study due to the limitation of field measurements. However, efforts were made to minimize the effects of these factors by choosing the same age of rice in the focused areas of investigations with the selective categories of rice.

1.2.2. Environmental problems in open pit mining

Figure1.5 shows the Mae Moh coal lignite mine, one of the largest open-pit mines in the region where deposits cover an area of more than 38 km^2, has been planned and

operated by the Electricity Generating Authority of Thailand (EGAT) since 1955. Mae Moh mine supplies up to 50,000 tons of lignite to daily feed the power plants located in the mining area. The current deepest level of the pit is about 300 meters in the northeast mine area while the final depth will be 490 meters at the end of production.

Figure1.5 Overview of the excavation area at Mae Moh lignite mine, Lampang province (as of September 2010).

Due to a huge volume of the overburden excavation of about 60-80 million cubic meters per year, many engineering problems caused by the deep open-cut have been reported and handled. The first alarm of the groundwater problem in Mae Moh was found in mid of 1988 when the numerous hydrological investigations were equipped in basement (Doi Chang formation). It has been confirmed that high-grade lignite seams (K and Q seams) are situated a very deep layer where the geological structures are complex. Based on the geotechnical investigations, the Basement formation located in the Central Pit (C1) area mainly consists of argillite with high water pressure. For this reason, this research aims to investigate the behavior of groundwater and establish the rational dewatering program from the aquifer to reduce adverse groundwater pressure for the

safe excavation with minimum impact on the surrounding environment. The result from this research can be applied to secure the stability and reduce the environmental impact of deep excavation of coal mining. Due to the complex geological condition in Mae Moh, the model is created according to the simplified geological and hydrological setting proposed by previous researcher (Giao 1992; Honjo et al. 1992; Honjo et al. 1994; Pongpanlarp 2007).

1.3. Dissertation structures

The dissertation structure is summarized as shown in Figure1.6. Nakhon Ratchasima, Khon Kaen, Sakon Nakhon, and Udon Thani situated in northeastern Thailand and Mae Moh lignite mine located in Lampang province of Thailand are chosen as case studies. Very details information of this research is explained in each chapter.

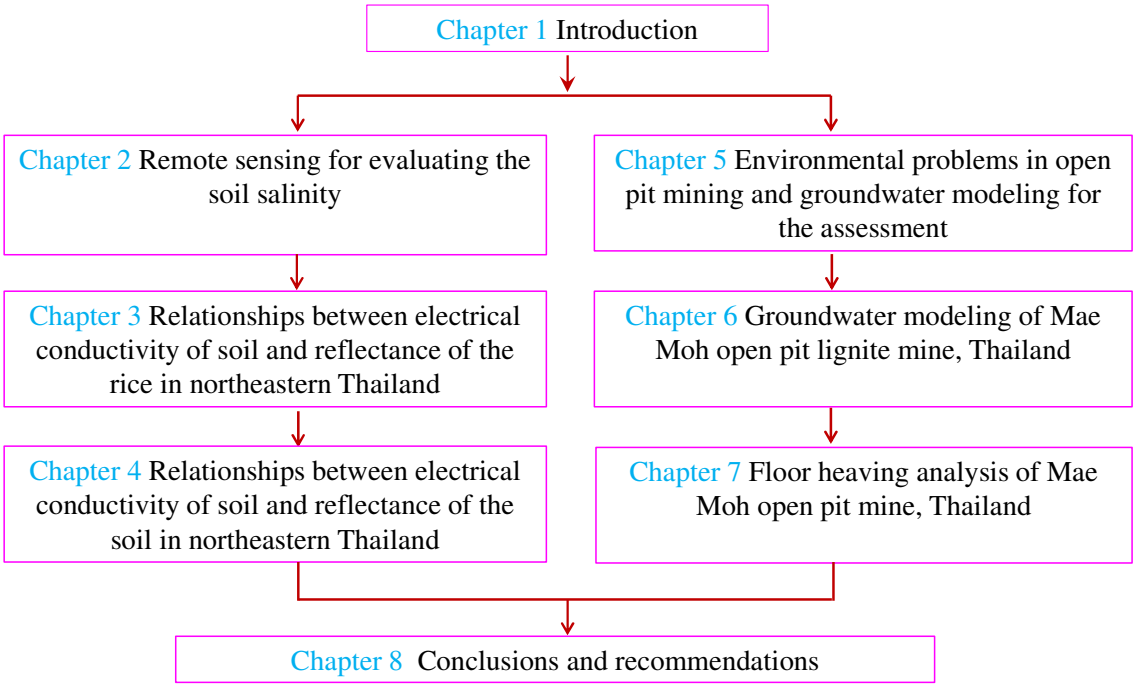

Figure1.6 Dissertation structures

This dissertation is organized into eight chapters as follows:

Chapter 1: Introduction

General background, problem statement, objectives, scope of this research and structure of the dissertation are emphasized. The general view of the environmental problem was highlighted. The common environmental problem of this study was included.

Chapter 2: Remote sensing for evaluating the soil salinity

The fundamental backgrounds of soil salinity and remote sensing for assessing the soil salinity were explained. In addition, the literature review of previous research related to soil salinity using remote sensing technique was also pointed out.

Chapter 3: Relationships between electrical conductivity of soil and reflectance of the rice in northeastern Thailand

A case study responding to the objectives of this study was presented. The site investigation is carried out to observe the encountered problem occurred. The chapter particularly presents the geological setting and source of soil salinity in northeastern Thailand. Field investigations of various paddy fields in northeastern Thailand were carried out in late November 2010 during the ripening season just before harvest in an attempt to realize the applications of the field hyperspectral technique for monitoring the spread of saline soils and estimation of the effects of soil salinity on rice plants. Jasmine rice and glutinous rice were two different rice species selected for this study. The statistical analysis revealed that the changes in soil EC were significantly sensitive to the ripening stages of both jasmine rice and glutinous rice planted at different levels of soil salinity. Among reflectance measurements, canopy reflectance was highly correlated with soil EC. The highest correlations are found in the near infrared (NIR) and shortwave infrared (SWIR). However, the estimated accuracies of relationship between soil EC and reflectance of glutinous rice were relatively lower than those of jasmine rice.

Chapter 4: Relationships between electrical conductivity of soil and reflectance of the soil in northeastern Thailand

The chapter presented the relationships between electrical conductivity of soil and reflectance of the soil in northeastern Thailand. First, the field measurements such as soil reflectance, the ions contents in the salt affect soil were explained. The relationship between electrical conductivity of the soil to the concentration of ions contents such as chlorides, calcium, magnesium, sulfates, and carbonates of sodium in the soil were also investigated. The good correlation of electrical conductivity of the soil to the ions was also confirmed. Therefore, the electrical conductivity could be selected as the salinity indicator. In addition, the relationships between soil EC and reflectance of soil have been determined by simple linear regression (SLR) analysis. Large distributions of low correlation, the magnitude values of the coefficient of determination (R^2) were less than 0.55, are dispensed over the entire region. Even though the weak correlation was found, this study could be used as the fundamental of the soil reflectance taken from the mixing soil sample on the surface and at 20 cm depth and soil salinity.

Chapter 5: Environmental problems in open pit mining and groundwater modeling for the assessment

This chapter explained the general background of groundwater modeling, groundwater problem in mining for assessment. The literature review such as groundwater flow equation, type of aquifers, influence of groundwater on stability, mode of floor heaving, floor heaving evaluation was also included. The previous research associated with groundwater modeling and stability study in the Mae Moh was also highlighted in this chapter.

Chapter 6: Groundwater modeling of Mae Moh open-pit lignite mine, Thailand

A case study of the environmental problem in the pit was explained. Mae Moh open pit mine was selected as the study area. Some general backgrounds such as geological setting, climate, and rainfall were highlighted. The process of groundwater modeling was pointed out such as a conceptual model, the model domain and grid design, material properties, model boundary condition, and initial head distributions. The calibration of steady state and transient state were also included in this chapter. The

calibration process was conducted to ensure that the groundwater modeling met the acceptable agreement between observation heads and computed head. The trial and error method was used by changing the input aquifer parameters within the acceptable range.

Chapter 7: Floor heaving analysis of Mae Moh open-pit lignite mine, Thailand

This chapter explains the case study of model prediction to establish the rational dewatering plan to reduce adverse groundwater pressure for the safe excavation with minimum pumping volumes in 2007 and 2015. First, the factor of safety was calculated according to the 40 years mining plan to define the critical area. Second, the water pressure control area was identified. Three wells were installed in the critical area to reduce the water pressure from the deep aquifer. Finally, the dewatering plan was conducted in the model prediction from 2007 to 2015.

Chapter 8: Conclusions and recommendations

The research results and recommendations for both soil salinity and groundwater modeling studies are summarized. The deficiency demands detailed investigations in the subsequent researches after this thesis were also reported.

CHAPTER 2 REMOTE SENSING FOR EVALUATING THE SOIL SALINITY

2.1. Introduction

Soil salinity is a global environmental problem and the most widespread land degradation problem that mostly take place in arid as well as semiarid regions (Epstein et al. 1980; Farifteh et al. 2006). The soil salinization is classified into primary (natural processes) and secondary (human activities) salinization (Metternicht and Zinck 2003). Traditionally, soil salinity can be analyzed and monitored by using ground-based methods. Soil samplings are collected in the target area and analyzed for EC at the field as well as in the laboratory. Normally, agriculture practice is associated with a large area. For this reason, the uses of field survey methods to detect and monitor soil salinity would be prohibitive in terms of labor and costs. Recently, the development method to map soil salinity with field measurement using remote sensing data and technology has been extensively applied in the last two decades (Hunt and Salisbury 1976; Mougenot et al. 1993; Ben-Dor 2002). The destructive methods used in plant analyzes are time-consuming and cannot sufficiently reflect spatial variability. Consequently, remote sensing can fulfill the demand for quick, accurate, and simple for plant analysis (Pasquini 2003).

This chapter presents a theoretical background of the standard methods that were used in the analysis and monitoring the spread of soil salinity. Firstly, the detailed cause of soil salinity is presented. Secondly, the reviewed in the previous study of remote sensing for evaluating the soil salinity is also explained.

2.2. Soil salinity

Soil salinity refers to the accumulation of salt in the soil especially on the surface or near-surface. Eight ions, cations of calcium (Ca^{2+}), magnesium (Mg^{2+}), sodium (Na^{+}) and potassium (K^{+}) and anions of alkalinity such as carbonate (CO_3^{2-}), bicarbonate (HCO_3^{-}), and carbonic acid (H_2CO_3); sulphate (SO_4^{2-}) and chloride (Cl^{-}), are the common elements associated with soluble salts (Tanji 2002). The accumulations of

these soluble salts in the soil profile negatively affect crop yields and reduce soil productivity. The characteristic of soil salinity is conventionally measured by the electric conductivity (EC) of soil with a unit of decisiemens per meter (dS/m), which is used to express the concentration of soluble salts (Goldshleger et al. 2013). The EC provides an indirect estimation of salt concentration in the soil. The soil is categorised as saline soil when it contains adequate soluble salt concentrations to give EC values, examined in a saturated extract (EC_e), higher than 4 dS/m as shown in Table 2.1 (Leone et al. 2007). The $EC_{1:5}$, 1:5 soil/water suspensions, is commonly used because it is rapid and easy to conduct. The $EC_{1:5}$ values can be converted to EC_e values according to the texture of the soil by the multiplier factors to an appropriate value of ECe.

Table 2.1 Interpretation of electrical conductivity from a saturated extract (EC_e) adopted from Richards (1954).

Soil Salinity Class	**EC_e (dS/m)**	**Effect on Crop Plants**
Non saline	0 - 2	Salinity effects negligible
Slightly saline	2-4	Yields of sensitive crops may be restricted
Moderately saline	4-8	Yields of many crops are restricted
Strongly saline	8-16	Only tolerant crops yield satisfactorily
Very strongly saline	> 16	Only a few very tolerant crops yield satisfactorily

Several types of salinization can be categorized as presented in Figure 2.1. Many factors can cause the salinization. The soil salinization is classified into primary and secondary salinization, which respectively affect 955 and 77 million hectares (Metternicht and Zinck 2003). In Southeast Asia, 5.8 million ha of land areas are harmed by soil salinity, one-quarter of which are located in Thailand, represented 2.7 percent of the country's land area (Shrestha 2006). Primary salinization result from natural weathering of parent material such as rock and minerals that influenced by factors associated with climatic, topography, hydrologic, and geologic and soil conditions. Secondary salinization develops from mobilization of the stored salt in the soil profile and/or groundwater dues to human activities and practices such as irrigation

practice, deforestation, and mining activities (Greiner 1997).

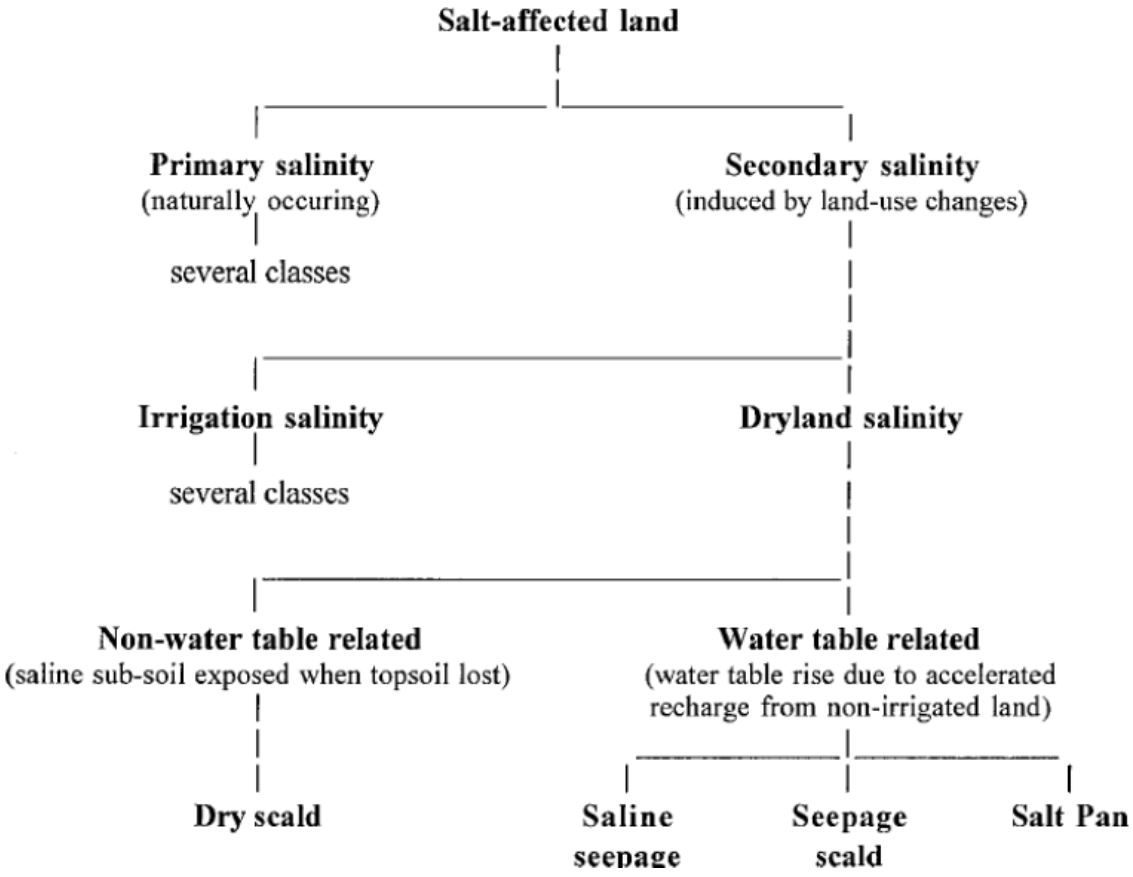

Figure 2.1 Categories of salt affected soil adopted from Greiner (1997)

2.2.1. Conversion of $EC_{1:5}$ to EC_e

In general, EC_e is used for interpretation of soil salinity in relation to plant growth. The EC_e is difficult to determine. For this reason, the rapid way of measurement EC is conducted according to the specific mixing ratio such as 1:1, 1:2 and 1:5. $EC_{1:5}$ is commonly used for the EC measurement (Hazelton and Murphy 2007).

Thus, the conversion of $EC_{1:5}$ to EC_e is imperative.

$$ECe\ (dS/m) = EC_{1:5}\ (dS/m) \times \text{multiplier factors} \quad (2.1)$$

The multiplier factor can be determined based on the texture of the soil as shown in Table 2.2. Nevertheless, $EC_{1:5}$ values are usually converted to EC_e using a multiplier

factors accordingly. Importantly, the results of $EC_{1:5}$ values should be attached with the result of soil texture.

Table 2.2 Multiplier factors for converting $EC_{1:5}$ (dS/m) to an approximate value of EC_e (dS/m) (Slavich and Petterson 1993)

Soil texture	Multiplier factor
Sand, loamy sand, clayey sand	23
Sandy loam, fine sandy loam, light sandy clay loam	14
Loam, fine sandy loam, silty loam, sandy clay loam	9.5
Clay loam, silty clay loam, fine sandy clay loam, sandy clay, silty clay, light clay	8.6
Light-medium clay	8.6
Medium clay	7.5
Heavy clay	5.8
Peat	4.9

Based on Shaw (1999), these multiplier factor are not always correct, but allowing to use for enabling an assessment of the soil salinity status. These relationships are principally according to chloride salts, so where large quantities of sulfate and carbonate salts are present, some error may occur using this conversion. The sparingly soluble salts such as gypsum and some carbonates and silicates may become more soluble with the greater dilution in a 1:5 soil/water extract.

2.2.2. Conversion of EC_e to Total dissolved solids (TDS)

The degree of salinity can also be measured by total dissolved solids (TDS) expressed as milligrams solute per liter (mg/L). The relationship between EC_e and TDS is expressed as (Hazelton and Murphy 2007):

$$TDS = k_e \times EC_e \quad (2.2)$$

where TDS is expressed in mg/L, EC_e is the electrical conductivity in dS/m at 25 °C, and k_e is the correlation factor which varies between 0.55 and 0.8 (Atekwana et al. 2004).

2.3. Impact of soil salinity on crops

The excessive salt concentrations in the soil have detrimentally influenced the soil's chemical and physical properties (Ramoliya et al. 2006) and have hastened land degradation phenomena that reduce crop yields together with agricultural productivity (Boyer 1982). The inordinate salt content in the soil lowers the potential osmotic of water and the ability of water to the plants (Katerji et al. 2009). Several factors such as soil, management, and climatic factors highly controlled soil salinity (Allbed et al. 2014). The stunted plants, leaf burn, and restricted root development are caused by the effects of salinity on crops growth and water stresses. When the salt concentration is too high, the soil salinity can lead total death of the plant. Accordingly, the soil salinity can also lead to the economic losses and food security problems.

2.4. Methods of the soil salinity detection

Since the soil salinity problem is dramatically increasing, the rapid monitoring of the spread of soil salinity and estimation of the effects of soil salinity is essential (Metternicht 2001). The studies of effectiveness and efficiency method and technique of the soil salinity detection have been undertaken by various researchers (Hunt and Salisbury 1976; Goetz and Herring 1989; Mougenot et al. 1993; Ben-Dor 2002; Dehni and Lounis 2012; Katawatin and Sukchan 2012)**.** The methods and technique have been applied to detect the soil salinity range from ground-based to remote sensing. For this reason, the use of the ground-based methods is somewhat less preferred as they are somehow expensive, time-consuming and laborious, and their application in large scale areas is impractical. Therefore, simple and reliable evaluation method of soil salinity is required which can be used for large. The later approach includes aerial, and satellite sensors associated with the conventional field measurements have been applied (Shrestha 2006).

According to Metternicht and Zinck (2003), the study of soil salinity problem using remote sensing data is complicated due to dynamic nature of the salinization process, and characteristics linked to spectral, spatial and temporal behavior of salts. The spectral confusion with other terrain surface features and interference by vegetation cover are

the main causes of the inadequate of remote sensing data. Because salinization typically occurs below the soil surface, remote sensing lacks the ability to look into the subsoil and might not able to detect salinization in the early stage. Additionally, remote sensing technique has limitations on classified the salt concentration in the soil in terms of severity levels, in particular, the accuracy indicating slightly and moderately affected soils. Nevertheless, the advantage of remote sensing technique is relatively cost-effective and efficient especially for mapping large-scale areas.

2.5. Remote sensing of salt affected soil

The development method to map soil salinity with field measurement using remote sensing data and technology has been extensively applied in the last two decades (Hunt and Salisbury 1976; Goetz and Herring 1989; Mougenot et al. 1993; Ben-Dor 2002; Dehni and Lounis 2012; Katawatin and Sukchan 2012). Remote sensing technique can be used to detect the presence of salts on the surface either directly on bare lands or indirectly through the vegetation, which is affected by salinity (Mougenot et al. 1993; Metternicht and Zinck 2003). Typically, the detecting and monitoring of salt-affected soils by remote sensing is conducted using aerial photographs, video images, infrared thermography, visible and infrared multispectral and microwave images (Metternicht and Zinck 2003; Abbas et al. 2013). Mainly, broadband sensors such as Systeme Pour l'Observation de la Terre (SPOT) High-Resolution Visible (HRV), Moderate-resolution Imaging Spectroradiometer (MODIS), and Landsat Thematic Mapper (TM) have been used for studying salt-affected soils.

2.6. Broadband remote sensing of soil salinity

Largely, broadband sensors have been applied to detect soil salinity and yielded satisfactory results (Csillag et al. 1993; Metternicht 2001; Metternicht 2003; Khan et al. 2005; Douaoui et al. 2006; Fernández-Buces et al. 2006; Yu et al. 2010). Jian-li et al. (2011) used a Landsat Enhanced Thematic Mapper Plus (ETM+) image to classify and extract of soil salinity from other cover and soil types using principal component analysis (PCA). The study revealed that the PC3 was the best band to identify areas of severely salinized soil while the blue spectral band from the enhanced thematic mapper

plus sensor (TM1) was the most appropriate to recognize salinized soil by identifying salt-tolerant vegetation. Bouaziz et al. (2011) reported moderate correlations between EC and spectral indices using a linear spectral unmixing (LSU) technique to improve the prediction of salt-affected soils using MODIS data. In addition, they established that the use of the LSU enhanced the correlations. Ding et al. (2011) classified land cover into different levels of soil salinity using the Landsat ETM+ image by means of PCA and decision tree approach. They obtained an accuracy of 95%. Melendez-Pastor (2010) used image-based spectra of saline and non-saline training areas, and the spectrum of the halite mineral as a surrogate to the spectra of saline soils to map saline soils using multispectral ASTER images by matched filtering and mixture tuned matched filtering techniques. They reported that the image-based approach was the most accurate approach for saline soil mapping and monitoring.

Although the success of multispectral sensors in mapping severely salt-affected soils, they have limitations in mapping slightly to moderately affected soils (Farifteh et al. 2006; Weng et al. 2010).This is attributed to their low spectral resolution and the use of traditional classification techniques (Dehaan and Taylor 2003; Tamás and Lénárt 2006). Additionally, it is not easy to map small areas including areas with a good cover of salt tolerant plants (Dutkiewicz et al. 2009).

2.7. Hyperspectral remote sensing of soil salinity

Hyperspectral remote sensing has the potential to overcome the spectral limitations of the broadband data as it provides near-laboratory quality spectra for each pixel. Each picture element contains a distinctive spectrum that can be used for the recognition of earth's surface materials. The spectrum allows the discrimination of slight differences between materials, permitting the investigation of phenomena that impressively extend the capability of traditional remote sensing (Chang et al. 2001; M. et al. 2003; JB 2007). This is possible because of the contiguous nature of the spectral profile of a hyperspectral signature. Currently, researchers have been investigating the value of hyperspectral remote sensing to enhance the detection of salt-affected soils using remote sensing (Ben-Dor and Banin 1994; Drake 1995; Ben-Dor 2002; Dehaan and Taylor 2003; Tamás and Lénárt 2006). It is anticipated that hyperspectral remote sensing will

yield more accurate detection of salinized soils. Encouraging findings on the value of hyperspectral remote sensing for studying salinized soils have been reported.

Additionally, hyperspectral remote sensing data can significantly provide an enrichment of spectral investigation abilities over conventional remote sensing data such as Systeme Pour l'Observation de la Terre (SPOT) High-Resolution Visible (HRV), Moderate-resolution Imaging Spectroradiometer (MODIS), and Landsat Thematic Mapper (TM) (Adam et al. 2010). Recent researches have shown that optimal information is presented in some specific narrowband (Thenkabail et al. 2004). Additionally, provided the significance of shortwave infrared (SWIR) bands in vegetation and agriculture researches, determining the optimal SWIR spectral bands is very important.

Farifteh et al. (2006) used PLSR and obtained prediction R^2 values between 0.78 and 0.98 using experimental soil sample data, which in each sample was treated with different salts (namely $MgSO_4$, KCl, NaCl, and $MgCl_2$). Weng et al. (2010) developed a univariate regression model to estimate soil salt content using a soil salinity index. The index was constructed from continuum-removed reflectance at 2052 and 2203 nm. Their model was applied to a Hyperion reflectance image and was successfully validated (R^2 = 0.63). Zhang et al., (2012) investigated the relationship between vegetation spectra and soil salinity. They derived vegetation indices from the recorded hyperspectral and then evaluated their predictive power for salinity. Subsequently, they employed a univariate linear correlogram as well as multivariate PLSR analysis to investigate the sensitive bands. They concluded that there is potential to monitor soil salinity with the hyperspectral of salt-sensitive and halophyte plants. Wang et al. (2012) developed an exponent reflectance model to estimate soil salt contents under various soil moisture conditions based on a control laboratory experiment on the two factors (soil salinity and soil moisture) to soil reflectance. They examined Na_2SO_4, NaCl, Na_2CO_3 with broad soil salinity (0% to 20%) and soil moisture (1.75% to 20%) (In weight base) levels for their effects on soil reflectance through a model based approach. They identified moisture resistant but salt sensitive bands of reflected spectra for the model before applying them to estimate soil salt content inversely. They found high R^2 of 0.87, 0.79,

and 0.66, and low means relative error of 16.42%, 21.17%, and 27.16% for NaCl, Na2SO4 and Na_2CO_3, respectively.

The use of hyperspectral remote sensing for studying soil salinity is not yet fully established. More investigations are still needed to uncover techniques to enhance the detection of salinized and/or salt-affected soils.

2.8. Spectroscopy of salt-affected soils

Using traditional wet chemistry techniques for soil salinity analysis may be restrictive due to high costs and labor when large amounts of samples have to be analyzed. It is accepted that near-infrared (NIR) spectroscopy and mid-infrared (MIR) spectroscopy are among less expensive and user-friendly techniques for quantitative soil analysis (Shepherd and Walsh 2002; Brown et al. 2006; Bellon-Maurel et al. 2010; Volkan Bilgili et al. 2010; Bellon-Maurel and McBratney 2011). It is perhaps the benefits regarding costs and less labor that makes the use of spectroscopic methods attractive, particularly because land that is under agriculture is massive these days. However, the soil sample preparation requirements for NIR and MIR spectroscopic analysis are not the same. MIR spectroscopy requires more sample preparation in order to optimize the light interaction while at the same time showing better specificity and reproducibility than NIR spectroscopy (Bellon-Maurel and McBratney 2011). On the other hand, NIR spectroscopy is reported to be easy to use and requires less sample preparation (Bellon-Maurel et al. 2010; Bellon-Maurel and McBratney 2011).

Viscarra Rossel et al. (2006) reviewed the literature comparing quantitative predictions of various soil attributes using a multivariate statistical technique and spectral response in the ultraviolet (UV), visible (VIS), NIR and mid MIR regions of the electromagnetic spectrum. They tabulated the soil attributes studied, spectral regions, spectral range, R^2, multivariate methods used, root mean squared error (RMSE) and the number of validation, and calibration samples used. Their work presents a comprehensive base of what can be achieved with respect to spectroscopy of soils.

2.9. Hyperspectral remote sensing of vegetation

The vegetation spectrum as shown in Figure 2.2 typically absorbs in the red and blue wavelengths, reflects in the green wavelength, strongly indicates in the near infrared (NIR) wavelength, and displays strong absorption features in wavelengths where atmospheric water is present. Different plant materials, moisture content, pigment, carbon content, nitrogen content, and other properties cause further variation across the spectrum. Measuring these variations and studying their relationship to one another can provide meaningful information about plant health, water content, environmental stress, and other essential characteristics. These relationships are often described as vegetation indices (VIs).

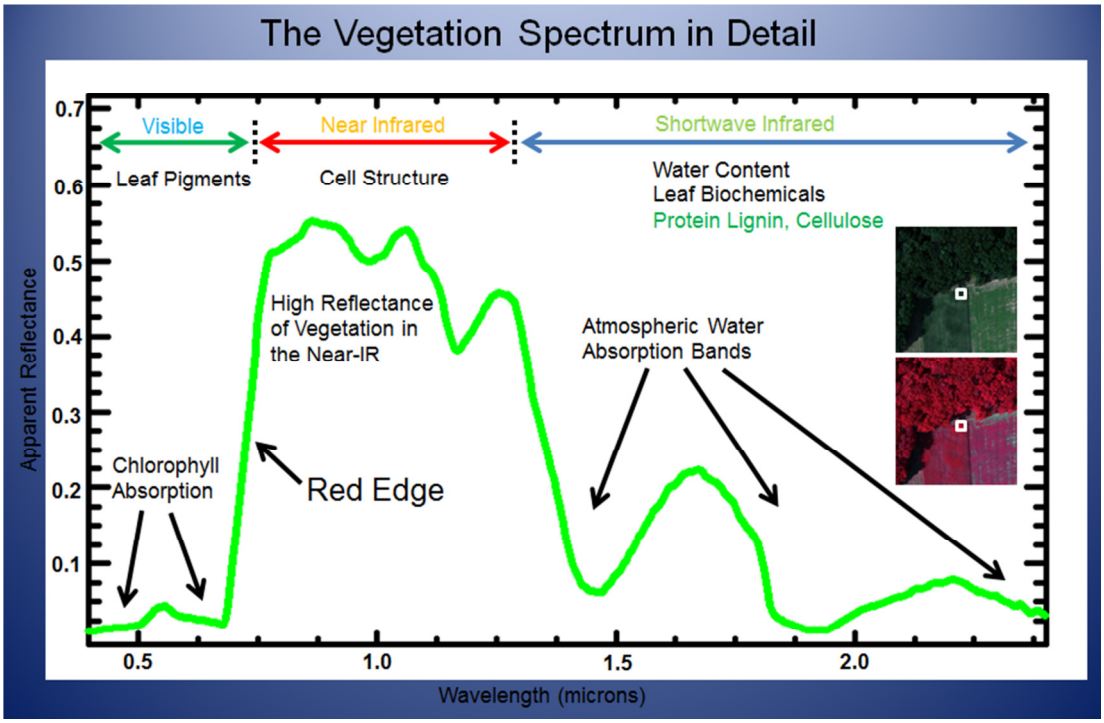

Figure 2.2 The detail of vegetation spectrum adopted from Elowitz (2015)

Among vegetation indices, the normalized difference vegetation index (NDVI) has been extensively used to analyzes multispectral information in crop plants owing to its simple form. The determination of NDVI can efficiently decrease the impacts of soil background and atmosphere noise (Yao et al. 2010). Development of plant features, such as biomass, water content, chlorophyll content, and leaf area index (LAI), affect

crop spectral reflectance from 350 to 2500 nm (Leone et al. 2007). Nevertheless, a new comprehensive analysis of rich hyperspectral data, normalized difference spectral indices (NDSI), needs to be undertaken to investigate new hyperspectral indices within the full spectrum of 350–2500 nm, which might produce accurate characteristic bands for estimating the biochemical elements in plants and other variables.

The optical spectrum is partitioned into four distinct wavelength ranges:

- Visible: 400nm to 700nm (the color Blue is approximately 475 nm, green is approximately 510nm and red is approximately 650nm)
- Near-infrared (NIR): 700nm to 1300nm
- Shortwave infrared 1 (SWIR-1): 1300nm to 1900nm
- Shortwave infrared 2 (SWIR-2): 1900nm to 2500nm

2.10. Regression analysis of soil salinity

Besides, assessing soil salinity spatial modeling, which is the utilization of numerical equations to simulate and predict real phenomena and processes, has followed several approaches. The approaches used range from artificial neural network (Farifteh et al. 2007; Akramkhanov and Vlek 2012), to classification and regression tree (Tóth et al. 2002; Taghizadeh-Mehrjardi et al. 2014), to fuzzy logic (Malins and Metternicht 2006), to generalized Bayesian analysis (Douaik et al. 2004), to geostatistics (e.g., Kriging, CoKriging and regression kriging) and statistical analysis (e.g., regression, ordinary least squares) . An overview of these techniques and how they provide optimal results under certain circumstances is given in the review papers of McBratney et al. (2003).

Regression analysis has become a general empirical method to link biophysical variables to remote sensing data in order to estimate continuous analyzes for these variables (Cohen et al. 2003). Regarding soil salinity, statistical analysis, particularly linear regression, has produced a fabulous potential among other techniques because of its speedy, practical, and cost-effective method (McBratney et al. 2003). Various statistical analyzes taken from remote sensing data have been improved and have become sensible predictors of soil salinity in past research (Tajgardan et al. 2010). A variety of statistical models based on remote sensing data has been developed and has

revealed reasonable predictors of soil salinity in the literature (Douaoui et al. 2006; Farifteh et al. 2006; Shrestha 2006; Farifteh et al. 2007; Tajgardan et al. 2010; Allbed et al. 2014).

2.11. Conclusions

The review of the literature presented in this chapter outlined the use of remote sensing, spectroscopy and terrain attributes for quantitative analysis of soil salinity, mapping, and modeling. There is consensus in the literature that traditional methods, for studying salt-affected soils, are not adequate due to the high costs and labor required. Cost effective and timely approaches are needed to enhance the quantitative analysis of soil salinity, mapping and modeling for improved monitoring. The literature revealed that the use of broadband sensors for studying salt-affected soils is not satisfactory due to limited spectral information. Hyperspectral remote sensing is promising to overcome the limitations of broadband sensors. The use of hyperspectral remote sensing for monitoring salt-affected soils still warrants more investigations.

CHAPTER 3 THE RELATIONSHIPS BETWEEN ELECTRICAL CONDUCTIVITY OF SOIL AND REFLECTANCE OF CANOPY, GRAIN, AND LEAF OF RICE IN NORTHEASTERN THAILAND

3.1. Introduction

Recently, soil quality for agricultural purposes has drawn much attention from many researchers, organizations, institutes, and local governments. Soil salinity refers to the accumulation of salt in the soil especially on the surface or near-surface; principally chlorides, calcium, magnesium, sulfates, and carbonates of sodium (Tanji 2002). Remote sensing technique can be used to detect the presence of salts on the surface either directly on bare lands or indirectly through the vegetation, which is affected by salinity (Metternicht and Zinck 2003). Several studies have suggested that abiotic and biotic environmental stress such as drought and salinity (Osborne et al. 2002), plant growth and physiology (Zhao et al. 2003), and the canopy characteristics of crops (Curran 1989) can be detected by crop spectral reflectance. Hence, the determination of soil EC from vegetation reflectance has significant potential implications for salinity stress detection and agricultural field management.

3.2. Geological setting and stratigraphic setting

Geologically, northeastern Thailand is composed of a combination of Precambrian massif and Mesozoic sedimentary rocks, which is called a Khorat plateau (Wongsomsak 1986). This plateau comprises of two large basins known as the Sakon Nakhon basin and the Khorat basin. According to Yumuang (1983), the Khorat plateau has been dated back to the Mesozoic Era. The older formations of this plateau are salt-free, and the youngest is rich in salt, a possibility source of salt presented on the surface, which is called "the Maha Sarakham Formation or Rock Salt Formation." The modified stratigraphic log of the Maha Sarakham Formation was investigated by Yumuang (1983) and Takaya et al. (1985). Yumuang (1983), as shown in Figure 3.1, classified the Maha Sarakham Formation into six members such as basal salt upper salt, upper clastic, lower clastic, middle salt, and middle clastic. On the other hand, Takaya et al.(1985) categorized it into upper clastic and rock salt. In addition, Takaya et al. (1985) classified

the upper part of Yumuang's upper clastic member as "Plio-Pleistocene Formation". This formation was not formerly recognized because it was confused with alluvium due to its elements are extremely less consolidated than that of the Maha Sarakham Formation.

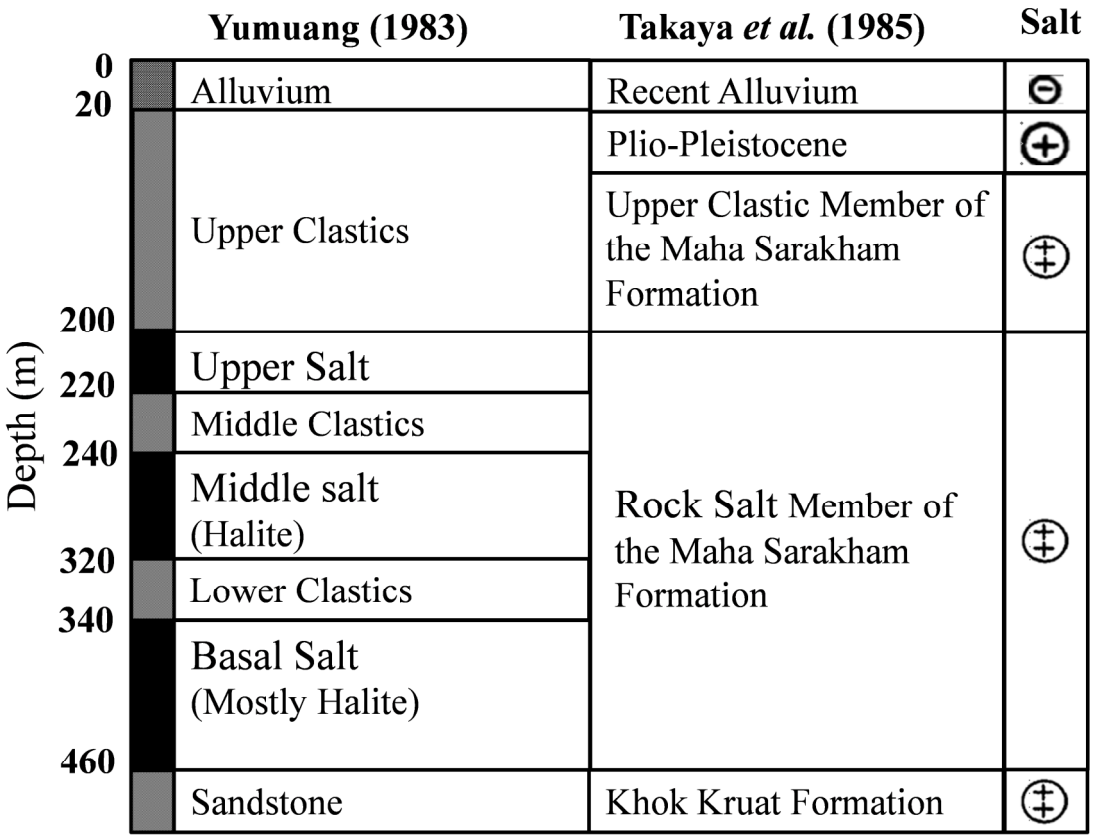

Figure 3.1 A Simplified Stratigraphic Column Shows Previous Subdivisions of the Maha Sarakham Formation modified after Takada et al.(1985).

The predominant compositions of the Maha Sarakham formation are claystone, shale, and inter-bedded with few layers of evaporate (gypsum, halite, anhydrite, sylvite, and carnallite) ranging in thickness from 10 to 170 m. The component of the Plio-Pleistocene Formation is fully clay with notable brownish yellow mottles, white to light matrix color, and frequently composing of large calcium carbonate nodules. Nakhon Ratchasima and Khon Kaen represent the affected areas in the Khorat basin while Sakon Nakhon and Udon Thani represent the affected areas in the Sakon Nakhon basin.

3.3. Source of soil salinity in northeastern Thailand

The primary source of soil salinity of the Khorat Plateau in northeastern Thailand is the geological formation, which includes salt rock as part of its composition. Based on the investigation of Wongsomsak (1986), there are three main sources of soil salinity in the Khorat Plateau, namely, the upper clastic member of the Maha Sarakham Formation, a rock salt member of the Maha Sarakham Formation, and the Plio-Pleistocene Formation. Geologically, the areas of soil salinity in the Khorat plateau are mainly categorized into three areas, namely, hill, basin, and the valley based on their topography and geology. The salt appeared in the hill area is intimately associated with the salt-bearing rock and the rock salt member of the Maha Sarakham Formation. Salt is visible either directly on the salt-bearing rocks or on foothills because of the seepage. The salt appeared in the basin area is similar to the salt presented in Thung Kula Ronghai, is found in the shallow layer of the Plio-Pleistocene Formation and the scattered, isolated hills toward the north. The salt appeared in the valley area is accelerated from brine.

The problem associated with soil salinity is caused by natural influences such as the variation in groundwater piezometric pressures and human activity in the salt mining industry. The mechanism of the salinity process in the Khorat Plateau is short-distance interflow of brine in the deep salt-source layers due to capillary force. In the case of heavy rains, salt is eroded and weathered from the salt source formations. The salt is transported into the groundwater by surface flow (Wongsomsak 1986). The salt is accumulated due to the water runoff, which leaches salts from upland. The saline groundwater reaches the surface through natural faults, or after being pumped out during salt mining activities. The salts begin to propagate upwards through the soil profile, with the help of bio-climactic influences, which increase the evapotranspiration rate until salt spots begin to appear on the soil surface (Imaizumi et al. 2002).

Numerical studies can explain the characteristics of salinity concentration carried out by Iizuka et al. (2007) and Iizuka et al. (2012). They found that the cycles of wet and dry on the ground caused by the seasons have a remarkable influence on the salinity content in the ground closer to the surface, leading to the accumulation of salt and

recrystallization on the ground surface because evaporations surpass precipitations through rainfall and salinity migration follows the direction of the pore water flow. This result implies that, once the salinity appears on the ground and recrystallizes, salinity pollution in the ground above the ground water level never returns to the original condition what it was before.

3.4. Field investigations and measurements

3.4.1. Site conditions

The northeastern Thailand has two main climatic seasons such as the dry season (November to April) and the rainy season (May to October). The dry season is generated from the dry winter monsoon from China, and the rainy season is influenced by the typhoons of South China and the maritime monsoon crossing over the Indian Ocean. The mean annual rainfall in the area is 650 mm, and average humidity is 72 percent. The maximum, minimum, and average temperatures of the area are 35.7, 22.8, and 29.2 °C, respectively. The topography is ranging with an elevation from 150 to 190 m above mean sea level. The study was conducted on typical paddy fields in northeastern Thailand during the ripening season just before harvest in late November 2010. The experimental sites were investigated from four representative provinces as presented in Figure 3.2 and summarized in Table 3.1–Table 3.3, namely, Nakhon Ratchasima, Khon Kaen Sakon Nakhon, and Udon Thani, after a series of past investigations (Pipatpongsa et al. 2007) based on the report of the salt damage area from the Land Development Department (Sukchan 2007).

Two different rice species were selected for this study. According to Pipatpongsa et al. (2011), jasmine rice (RD 15) is widely cultivated in the Khorat basin due to the appropriate climate condition, while glutinous rice (either RD 6 or RD 10) is mostly planted in the Sakon Nakhon basin due to the sufficient irrigation system. RD 15 (standard height 140–150 cm, harvested from the middle of November) has a jasmine fragrance and long shape mutated from the original variety of jasmine rice KDML105. Glutinous rice RD 6 (standard height 154–160 cm, harvested from late November) is also initially treated from KDML105. The hybrid sticky rice RD 10 bred from the rice RD1 can be grown during off-season with a shorter height of 115 cm.

Table 3.1 The summaries of experimental sites in Nakhon Ratchasima and Khon Kaen province.

Province	Measurement	Subject	Amount	Unit
Nakhon Ratchasima	Reflectance	Jasmine rice (grain & canopy)	24	quadrats
		Jasmine rice (leaf)	12	quadrats
		Soil (top)	13	sets
		Soil (20 cm depth)	13	sets
	EC field	Top soil	9	quadrats
	Sample (EC & pH lab)	Soil (top & 20 cm depth)	26	samples
	Plant conditions	Crop length	13	quadrats
		Panicle	13	quadrats
		LAI	13	quadrats
		Canopy openness	13	quadrats
Khon Kaen	Reflectance	Jasmine rice (grain & canopy)	16	quadrats
		Jasmine rice (leaf)	8	quadrats
		Soil (top)	12	sets
		Soil (20 cm depth)	8	sets
	EC field	Top soil	15	quadrats
	Sample (EC & pH lab)	Soil (top & 20 cm depth)	24	samples
	Plant conditions	Crop length	8	quadrats
		Panicle	8	quadrats
		LAI	8	quadrats
		Canopy openness	8	quadrats

Table 3.2 The summaries of data in Sakon Nakhon and Udon Thani province.

Province	Measurement	Subject	Amount	Unit
Sakon Nakhon	Reflectance	Glutinous rice (grain & canopy)	12	quadrats
		Glutinous rice (leaf)	6	quadrats
		Soil (top)	7	sets
		Soil (20 cm depth)	6	sets
	EC field	Top soil	7	quadrats
	Sample (EC & pH lab)	Soil (top & 20 cm depth)	14	samples
	Plant conditions	Crop length	6	quadrats
		Panicle	6	quadrats
		LAI	6	quadrats
		Canopy openness	6	quadrats
Udon Thani	Reflectance	Glutinous rice (grain & canopy)	28	quadrats
		Glutinous rice (leaf)	13	quadrats
		Soil (top)	14	sets
		Soil (20 cm depth)	14	sets
	EC field	Top soil	14	quadrats
	Sample (EC & pH lab)	Soil (top & 20 cm depth)	29	samples
	Plant conditions	Crop length	14	quadrats
		Panicle	14	quadrats
		LAI	14	quadrats
		Canopy openness	14	quadrats

Table 3.3 The summaries of experimental sites referred in this study.

Province	Measurement	Subject	Amount	Unit
Total	Reflectance	Jasmine rice	60	quadrats
		Glutinous rice	59	quadrats
		Soil (top & 20 cm depth)	87	sets
	EC field	Top soil	45	quadrats
	Sample (EC & pH lab)	Soil (top & 20 cm depth)	93	samples
	Plant conditions	Crop length	41	quadrats
		Panicle	41	quadrats
		LAI	41	quadrats
		Canopy openness	41	quadrats

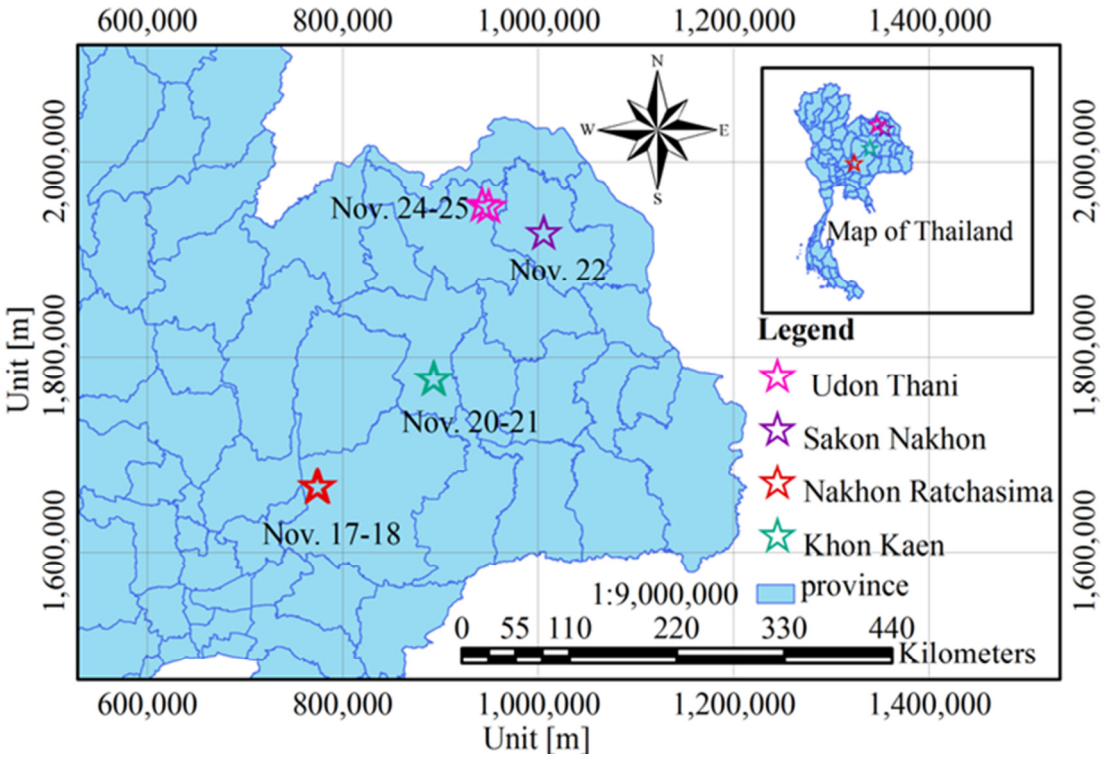

Figure 3.2 Map locating the investigated sites and soil sampling (Modified from Department of Mineral Resources, Kingdom of Thailand).

3.4.2. Hyperspectral reflectance measurements

The reflectance of canopy, grain, and leaf of rice were measured using a field-portable spectroradiometer ASD FieldSpec3 Pro and converted to spectral reflectance by ceramic pad. Quadrat (1 m × 1 m) was marked in each paddy as shown in Figure 3.3(a). The spectral reflectance measurement was conducted at nadir-looking. The reflectance measurement was investigated under clear sky conditions on cloudless or near cloudless days, approximately between 9:00 am and 16:00 pm (Thailand local time). The spectral reflectance range was over the continuous wavelength 350 to 2500 nm. Specifically, the field of view (FOV) of the spectral sensor was 25°. The spectral resolution is 3 nm and the sampling interval is 3 nm, and 10 nm was between 350 to 700 nm and 700 to 2100 nm, respectively. Thus, the measurements covered the ultraviolet, visible (VIS), near infrared (NIR), and shortwave infrared (SWIR) region of the spectra.

Figure 3.3 Reflectance measurement procedures: (a) quadrat 1 m × 1 m, (b) canopy reflectance, (c) grain reflectance, and (d) leaf reflectance

For each corner of the quadrat, including its middle, spectral reflectance was measured. The recorded spectrum file comprised continuous spectral reflectance at 1 nm steps over the band region ranging from 350 to 2500 nm because these data can contain optimal information in narrow wavelengths. The spectrometer was implemented with a 1.4 m optical fiber to enable the probe to go to the sample for easier measurements. The canopy reflectance was carried out over each quadrat, looking straight down from a height of 1 m with the angle of 25^{o} above the canopy using a ladder as presented in Figure 3.3(b). The grain and leaf reflectance were measured directly about 5 cm with the angle of 8^{o} above the fresh rice grain and leaf as shown in Figure 3.3(c) and Figure 3.3 (d), respectively.

3.4.3. Electrical conductivity measurements

At each site, soil core samples were taken from composite topsoil with sample layers of 5 cm and the subsurface layer at the depth of 20 cm as shown in Figure 3.4(a). The sampling sites were selected based on the desired variation using EC portable meter as illustrated in Figure 3.4(b). Each soil sample, as presented in Figure 3.4(c), was mixed, turning to one homogeneous sample of each location. The exact coordinates of each site were recorded using the Global Positioning System (GPS). After the measurement of spectral reflectance, soil samples from every corner and the middle of each quadrat were collected for field and laboratory experiments. Three different data sets of soil EC consisting of soil EC_{field}, soil $EC_{1:5}$ lab on the surface and soil $EC_{1:5}$ lab at 20 cm depth were collected in this study. The EC probe (ARP WD-3-WET-5E) was vertically inserted into the soil location and recorded by portable data logger (WDR-1). Volumetric water content (VWC), temperature (^{o}C), and soil EC were measured at the same time. Additionally, pH measurement was conducted by using PCSTestrth 35 of the soil solution as shown in Figure 3.4(d). Soil samples were sent to the domestic laboratory for physical and chemical analysis such as $pH_{1:1}$ and $EC_{1:5}$ of soil. Specifically, pH was determined potentiometrically in a 1:1 soil/distilled water suspension. $EC_{1:5}$ is the electrical conductivity of the solution determined in the laboratory conductometer by mixing one part of dry soil with five parts of distilled or deionised water by weight. After the sedimentation, the EC of the solution was tested (USSLS 1969).

Figure 3.4 Field investigations: (a) Soil sampling pit, (b) Electrical conductivity apparatus, (c) soil sampling, and (d) distilled water solution of soil

3.5. Changes in spectral reflectance

Taking variation of soil $EC_{1:5}$ lab on the surface as an example, Figure 3.5 exhibits the dynamic change patterns of the reflectance spectra obtained from the rice canopy, grain, and leaf reflectance under different levels of salinity in Khon Kaen province. The curves of canopy and leaf spectral reflectance of the rice were comparable to other reflectance of green plants. Different materials reflect and absorb at different wavelengths. Atmospheric absorption severely harmed the wavelength regions located in the range of 1350–1440, 1800–1960, and 2380–2500 nm during the field measurement process. Consequently, the spectral data in these wavelength regions were excluded from entire analyzes. In addition, the spectral data from 350 to 390 nm were also not included because of spectral inconsistencies. The remaining spectral data were in 390–1350, 1440–1800, and 1960–2380 nm and constituted a total of 1740 nm wavelengths of good noise-free spectral data that were available for analysis.

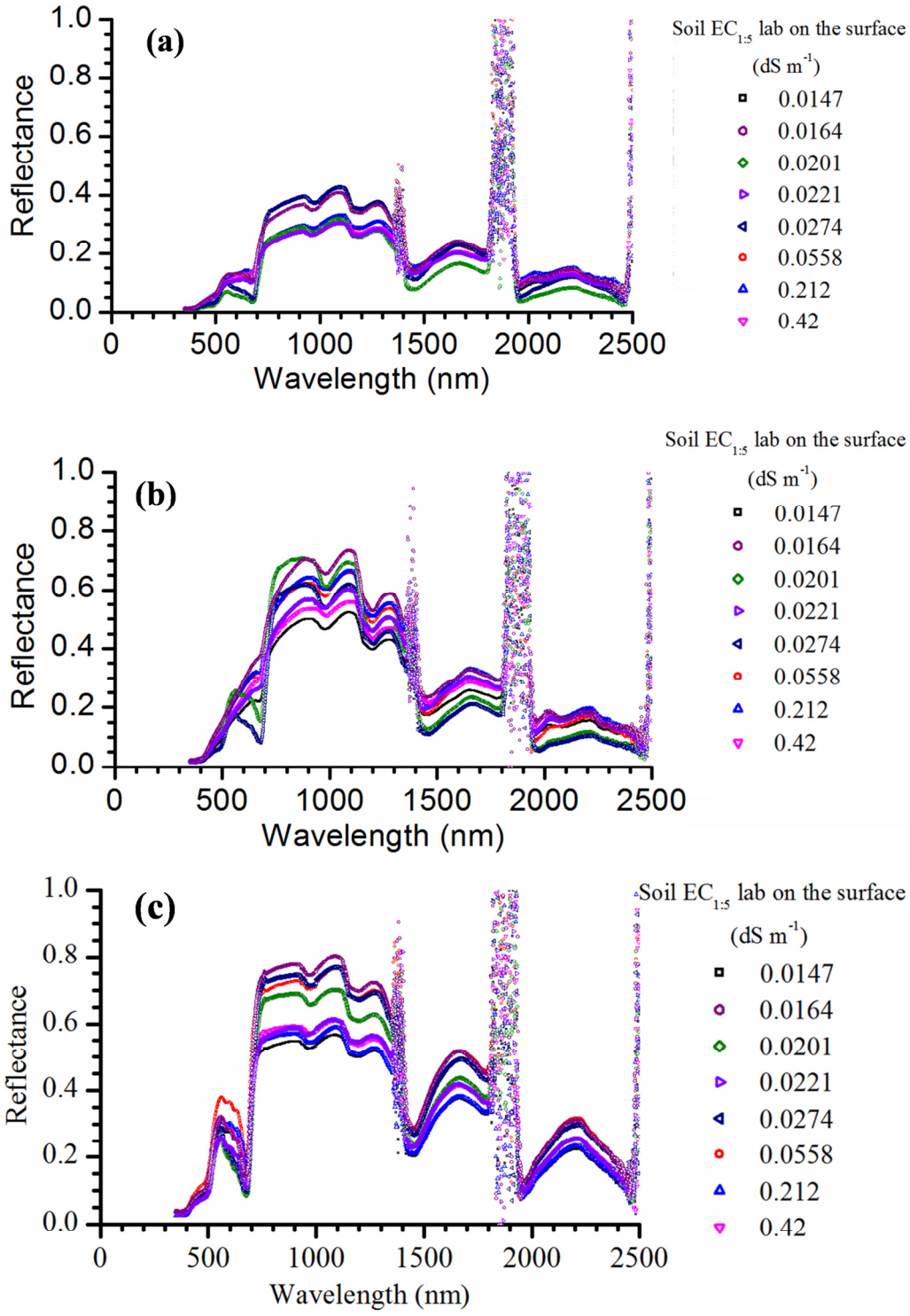

Figure 3.5 Changes in spectral reflectance with variation of soil $EC_{1:5}$ lab on the surface for samples taken from Khon Kaen province: (a) canopy reflectance, (b) grain reflectance, and (c) leaf reflectance.

Apparently, the variation of soil $EC_{1:5}$ lab on the surface is notably affected the characteristics of rice spectral reflectance in the numerous waveband regions. This indicated that these waveband regions were sensitive to the ripening stage of rice under the variation of soil $EC_{1:5}$ lab on the surface levels. The mean canopy reflectance as shown in Figure 3.5(a) was lower than that of grain as presented in Figure 3.5(b) and leaf reflectance as displayed in Figure 3.5(c), approximately 20%. The spectral reflectance was lower in the ultraviolet regions (350–400 nm) and the VIS regions (400–740 nm). On the other hand, it was higher in the NIR regions (740–1350 nm). Within the VIS regions, the maximum spectral reflectance was situated in the green region (490–570 nm) and the minimum spectral reflectance was located in the violet (400–425 nm) or red (640–740 nm) regions. In the blue regions (430–490 nm), the spectral is reflectance slightly increased and reached the maximum in the green regions (540–560 nm). The highest spectral reflectance was in the range between 1180–1190 nm and displayed a slight trough at the chlorophyll absorption regions (670 nm). Grain and leaf reflectance in the green wavelength were much higher than that of the canopy reflectance.

3.6. Data analysis

3.6.1. Determination of $NDSI_{i,j}$

The pre-process before determination of $NDSI_{i,j}$ is carried out by averaging the spectral data from every spectral reflectance measurement for each quadrat. $NDSIs_{i,j}$ is a method to extract the new spectral index from the full spectral band (Inoue et al. 2008), calculated by the formulation similar to NDVI. The NDSI expression for i and j bands is defined as:

$$\mathrm{NDSI}_{i,j} = \frac{(R_i - R_j)}{(R_i + R_j)} \tag{3.1}$$

Where R_i is the reflectance corresponding to the wavelength i and R_j is the reflectance corresponding to the wavelength j.

Mathematically, $NDSI_{i,j} = - NDSI_{j,i}$ and the value of $NDSI_{i,j}$ as shown in Equation (3.1)

ranges from -1 to 1. NDSI [i,j] was assigned as the spectral index, while soil EC was used as the salinity indicator, which varies with the location of the rice field. The hyperspectral data analysis was conducted using the VIS, NIR, and SWIR regions of the spectrum (350–2500 nm) subdivided into 1 nm bandwidths. Each of these was analyzed to seek a relationship between the measured data set of $NDSI_{i,j}$ and soil EC. The precise calculation of $NDSI_{i,j}$ was carried out for each integer i from 350 with j=i+3, i+4 until 2500. The resulting coefficients of determination (R^2) can help identify the best pair of wavelength (i,j) among the whole combinations of NDSIs. Then, inconsistent wavelengths that were affected by atmospheric disturbance from the field investigation were eliminated.

3.6.2. Statistical analysis

Simple linear regression analysis (SLR) was utilized to evaluate the correlation between soil salinity indicators, ripening stage of rice, and rice spectral variables. The R^2 indicates the strength of statistical analyzes between measured and predicted variable, and Root Mean Square Error (RMSE) symbolizes absolute values of estimation errors. In addition, the probability value (*p*-value) is used to determine the level of significance of SLR analysis. The *p*-value is calculated by using *F*-distribution according to the theory of one-way analysis of variance (ANOVA). The statistical analysis is significant if *p*-value < 0.05 and is highly significant if *p*-value < 0.001. The developed regression models were selected when the model met the requirement criteria, such as (i) high magnitude of R^2 values, (ii) low standard errors of the model prediction, and (iii) sufficiently significant *p*-value. The R^2 and RMSE are calculated using the following equations:

$$R^2 = \left(\frac{\sum_{i=1}^{n} (Y_i - \overline{Y})(X_i - \overline{X})}{\sqrt{\sum_{i=1}^{n} (Y_i - \overline{Y})^2 \times \sum_{i=1}^{n} (X_i - \overline{X})^2}} \right)^2 \quad (3.2)$$

$$\text{RMSE}=\sqrt{\frac{\sum_{i=1}^{n}(Y_i - X_i)^2}{n}} \tag{3.3}$$

Where Y_i and X_i are the predicted and observed values, respectively; $\overline{Y}$ and $\overline{X}$ represent the means of the predicted and observed values, respectively, and n is the number of samples.

All procedures of statistical analysis, 2-D contour mapping of R^2, and RMSE values respectively taken from Equations (3.2)–(3.3) were coded to MATLAB script with parallel processing features of Math Works version 2013b using 12 central processor units (CPUs) of TSUBAME 2.5, the supercomputer of Tokyo Institute of Technology. A total of 18 cases were performed for reflectance taken from the canopy, grain, and leaf of jasmine rice and glutinous rice with time used approximately about 108 hours.

3.7. Results

3.7.1. Electrical conductivity of the soil

The relevant statistical parameters for soil EC in the paddy field for jasmine rice and glutinous rice are summarized in Table 3.4 and, respectively. From field investigation, about 60% of the total samples were categorized as strongly saline soil. According to the manual of EC_{field} apparatus, the accuracy of this measurement ranges between 0–7 dS/m. For this reason, the value of soil EC, which was higher than the limitation, might be slightly biased. Because the targeted areas are located in salt-affected regions, soil samples are saline with the mean of soil EC_{field} of 6.07 dS/m for jasmine rice and 5.35 dS/m for glutinous rice. For soil $EC_{1:5}$ lab on the surface, the mean is 0.29 dS/m for jasmine rice and 0.21 dS/m for glutinous rice. For soil $EC_{1:5}$ lab at 20 cm depth, the mean is 0.16 dS/m for jasmine rice and 0.08 dS/m for glutinous rice. Note that the value of soil $EC_{1:5}$ lab is lower than that of soil EC_{field} because of the different method of measurement. In general, soil $EC_{1:5}$ lab at 20 cm depth is lower than soil $EC_{1:5}$ lab on the surface because of the naturally high concentration of salt accumulated on the surface. $EC_{1:5}$ lab for soils of both surface and at 20 cm depth was conducted in order to

raise the reliability of degree of salinity. It is noted that the values of $EC_{1:5}$ lab for soils taken from the surface is better correlated with soil EC_{field} than that taken at 20 cm depth as presented in Figure 3.6. For this reason, soil $EC_{1:5}$ lab on the surface is selected as the main salinity indicator referred in this study.

Table 3.4 Descriptive statistics of electrical conductivity (EC) of soil in the paddy fields for jasmine rice.

Description	Jasmine rice				
	Mean	Max	Min	SD	CV
	(dS/m)	(dS/m)	(dS/m)	(dS/m)	-
Soil EC_{field} (dS/m)	6.07	15.1	0.65	4.68	0.77
Soil $EC_{1:5}$ lab on the surface (dS m)	0.29	1.32	0.01	0.37	1.26
Soil $EC_{1:5}$ lab at 20 cm depth (dS m)	0.16	0.66	0.01	0.18	1.13

Table 3.5 Descriptive statistics of electrical conductivity (EC) of soil in the paddy fields for jasmine rice.

Description	Glutinous rice				
	Mean	Max	Min	SD	CV
	(dS/m)	(dS/m)	(dS/m)	(dS/m)	-
Soil EC_{field} (dS/m)	5.35	12.5	0	4.28	0.8
Soil $EC_{1:5}$ lab on the surface (dS/m)	0.21	1.01	0.01	0.25	1.2
Soil $EC_{1:5}$ lab at 20 cm depth (dS/m)	0.08	0.28	0.02	0.07	0.83

Notes: Max is maximum, Min is minimum, SD is a standard deviation, and CV is the coefficient of variation

The values of soil EC reported in this study do not indicate a representative degree of salinity of the entire province. The investigation team intentionally chose to visit the most severe lands reported for each province. Phang Khon district was chosen for Sakon Nakhon province. Kham Thale So district was selected for Nakhon Ratchasima province. Ban Phai district was chosen for Khon Kaen. Ban Dung district was chosen for Udon Thani province.

.

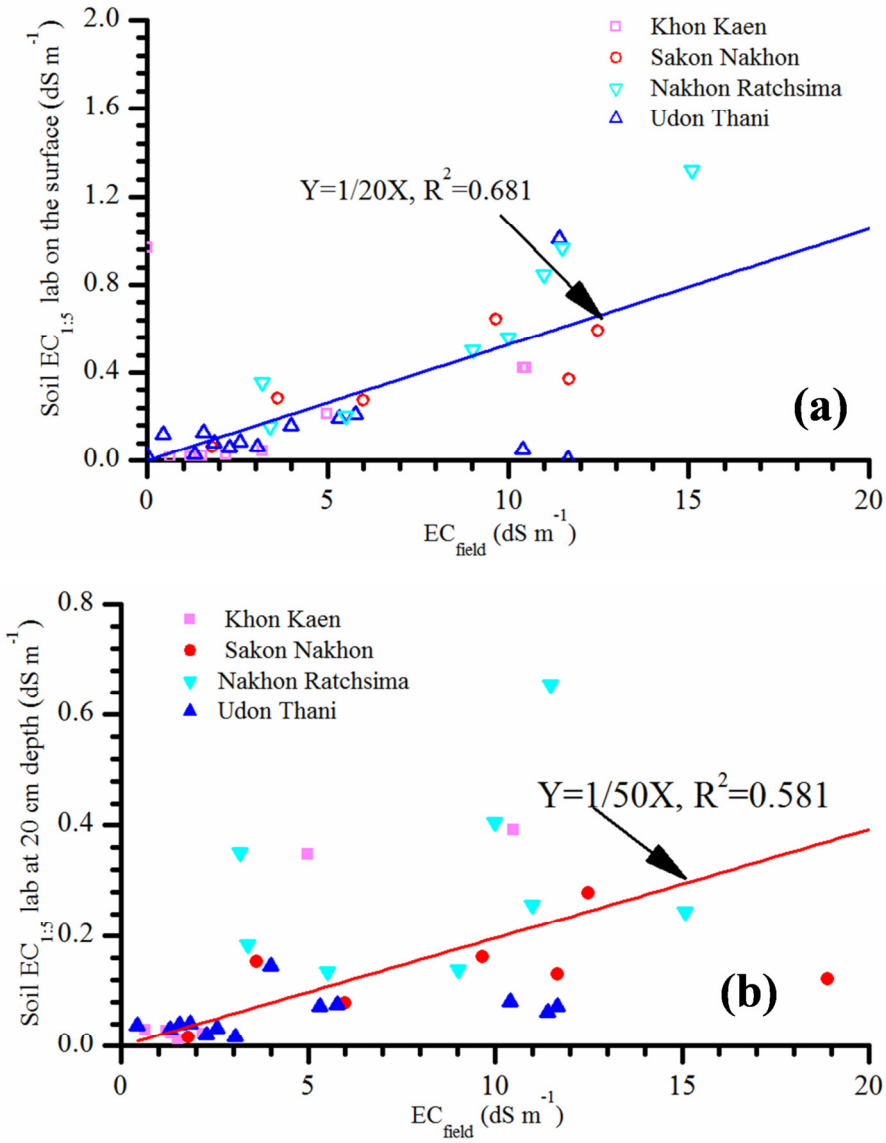

Figure 3.6 The correlation of soil $EC_{1:5}$ lab and EC_{field} used in the study: (a) on the surface and (b) at 20 cm depth.

3.7.2. Effect of soil salinity on the ripening stage of the rice

The studies of the effect of soil salinity (soil EC_{field} , soil $EC_{1:5}$ lab on the surface, and soil $EC_{1:5}$ lab at 20 cm depth) on the ripening stage of the jasmine rice and glutinous rice in northeastern Thailand were reported by Touch et al. (2013; Touch et al. 2013). This study highlighted several important parameters involved with soil salinities such as LAI, crop length, panicle length, soil EC, canopy openness, and soil pH.

Table 3.6 Relationships between crop length, panicle length, LAI, and canopy openness to soil $EC_{1:5}$ lab on the surface in the paddy fields.

Description				Soil $EC_{1:5}$ lab on the surface (dS/m)	
				Jasmine rice	Glutinous rice
Crop length	(cm)	Regression equation	-	y=-38.40x+137.330	y=-21.21x+136.590
		R^2	-	0.258	0.174
		p-value	-	0.0186	0.0668
		RMSE	(cm)	23.312	11.609
Panicle length	(cm)	Regression equation	-	y=-4.207x+24.002	y=-1.475x+24.730
		R^2	-	0.231	0.081
		p-value	-	0.0272	0.2247
		RMSE	(cm)	2.748	1.252
LAI	(-)	Regression equation	-	y=-2.147x+3.450	y=-0.489x+1.780
		R^2	-	0.550	0.048
		p-value	-	0.0001	0.3536
		RMSE	-	0.695	0.548
Canopy openness	(%)	Regression equation	-	y=31.171x+7.130	y=9.324x+28.290
		R^2	-	0.601	0.058
		p-value	-	3.690×10^{-5}	0.3042
		RMSE	%	9.577	9.918

Notes: For crop length: x=soil $EC_{1:5}$ lab on the surface/(dS/m), y=crop length/cm

For panicle: x=soil $EC_{1:5}$ lab on the surface/(dS/m), y=panicle length/cm

For LAI: x=soil $EC_{1:5}$ lab on the surface/(dS/m), y=LAI

For canopy openness: x=soil $EC_{1:5}$ lab on the surface/(dS/m), y=canopy openness/%

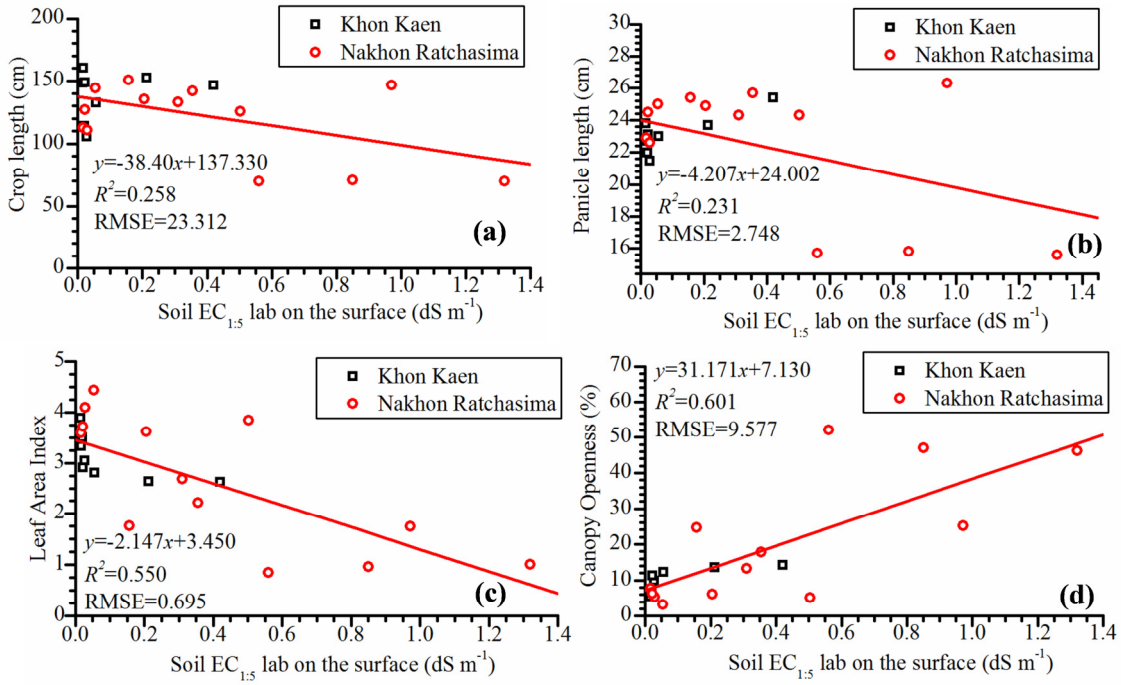

Figure 3.7 Changes in the ripening stage of rice with soil $EC_{1:5}$ lab on the surface for jasmine rice: (a) crop length, (b) panicle length, (c) leaf area index, and (d) canopy openness. Note that x is $EC_{1:5}$ lab on the surface measured in unit of dS/m, y is a quantity measured in unit as shown in each ordinate of figures and RMSE is root mean square error in unit of the ordinate.

Those parameters are the indicators to describe the density of vegetation as well as the influence of soil salinity to plant growth. The results indicated that the soil salinity was negatively effected to the ripening stage of the rice for both jasmine rice and glutinous rice. The overall growth performance of rice is reflected by plant height and leaf area. Salinity affects virtually all aspects of plant's physiology (Flowers et al. 2000). Rice is very sensitive to salinity during the reproductive stage. Table 3.6 summarises the statistical parameters from SLR analysis of crop length, panicle length, LAI, and canopy openness and soil $EC_{1:5}$ lab on the surface for jasmine rice and glutinous rice, such as regression equation, R^2, and p-value and RMSE.

Figure 3.7 exhibits the correlation between the ripening stages of rice to soil $EC_{1:5}$ lab on the surface for jasmine rice. The cropped length (p=0.0186) gradually decreases with

the increase of soil $EC_{1:5}$ lab on the surface as shown in Figure 3.7(a). Very few rice plants can be grown in high salinity with low productivity. The effect of the salinity on panicle length is linear and negative, approximately 20% decrease in unit increment of soil $EC_{1:5}$ lab on the surface, with R^2 equal to 0.231 as presented in Figure 3.7(b). The LAI decreases linearly with the increase of the salinity; the reduction being approximately 7% for an increase of soil $EC_{1:5}$ lab on the surface as demonstrated in Figure 3.7(c). Canopy openness is presented in Figure 3.7(d) with a positive linear line with the R^2 = 0.601 (p=3.690 $\times 10^{-5}$). This result reveals that the density of canopy is reduced under the variation of soil $EC_{1:5}$ lab on the surface from low to high value.

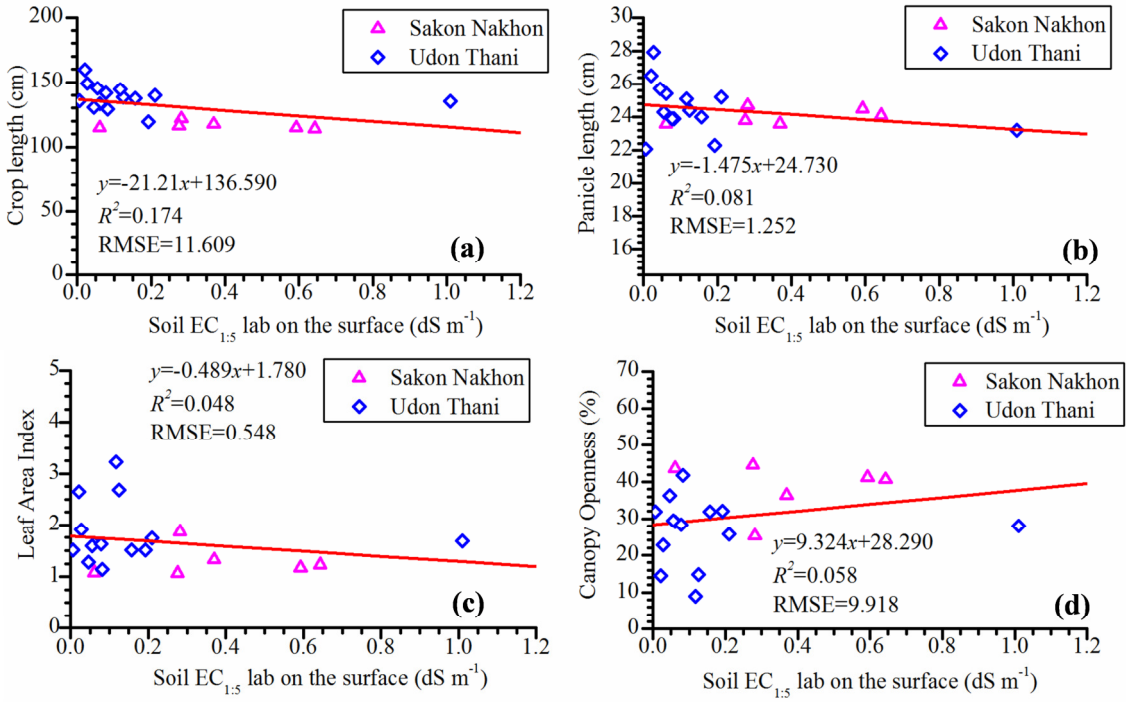

Figure 3.8 Changes in the ripening stage of rice with soil $EC_{1:5}$ lab on the surface for glutinous rice: (a) crop length, (b) panicle length, (c) leaf area index, and (d) canopy openness. Note that x is $EC_{1:5}$ lab on the surface measured in unit of dS/m, y is a quantity measured in unit as shown in each ordinate of figures and RMSE is root mean square error in unit of the ordinate

Similar behavior is found in glutinous rice, which is cultivated in Sakon Nakhon and Udon Thani provinces. Figure 3.8 illustrates the effect of salinity on the ripening stage of rice for glutinous rice under different levels of soil $EC_{1:5}$ lab on the surface. The

cropped length exhibits a dropping pattern with enhanced levels of the salinity ranging from 0 to 1.01 dS/m as displayed in Figure 3.8(a). Soil $EC_{1:5}$ lab on the surface is affected by total number of panicles length, LAI, and canopy openness is not significant ($p>0.1$) as displayed in Figure 3.8(b)– Figure 3.8(d), respectively. In conclusion, the ripening stage of glutinous rice is less sensitive to the salinity levels than those of jasmine rice. Typically, the glutinous rice needs more water to grow than jasmine rice. Hence, glutinous rice is suitable to cultivate in areas with good water management; for this reason, water provided by the irrigation system helps dilute the salt concentration out from the paddy field.

3.7.3. Canopy spectral reflectance

Preliminary analysis consisted of detailed plots of R^2, which were constructed in the form of 2-D contour maps at two separate wavelengths on *x* and *y* axes ranging from 350 to 2500 nm. A separate analysis was conducted for jasmine rice and glutinous rice. The "narrow peak" indicates wavelength regions of relatively high correlation while deep troughs indicate weak correlations.

With respect to spectral data of canopy, Figure 3.9(a) shows the contour map of R^2 between $NDSIs_{i,j}$ and soil $EC_{1:5}$ lab on the surface (upper triangle) and soil $EC_{1:5}$ lab at 20 cm depth (lower triangle) for jasmine rice. As a whole, the region consisting NDSI of 450–500, 600–700, 900–1050, 1600–2000, and 2100–2300 nm indicate high R^2 values (blackish). The same methodology was conducted with another set of spectral data for glutinous rice to seek the sensitive spectral band in relation to soil EC. Figure 3.9(b) exhibits the contour map of R^2 between NDSIs [i,j] for canopy reflectance and soil $EC_{1:5}$ lab on the surface (upper triangle) and soil $EC_{1:5}$ lab at 20 cm depth (lower triangle) for glutinous rice of two wavelengths on *x* and *y* axes ranging from 350 to 2500 nm. High correlation values are mostly greater than 0.55 on particular ranges of NDSI which are 700–1150, 1600–2000, and 2100–2250 nm for soil $EC_{1:5}$ lab on the surface and soil $EC_{1:5}$ lab at 20 cm depth.

3.7.4. Grain spectral reflectance

Using the same methodology for determining NDSIs [i,j], distribution maps of R^2

values for the correlation of $NDSI_{i,j}$ to soil EC based on grain reflectance were obtained. Figure 3.10(a) illustrates the contour maps of R^2 values between NDSI [i,j] and soil $EC_{1:5}$ lab on the surface (upper triangle), and soil $EC_{1:5}$ lab at 20 cm depth (lower triangle) for jasmine rice. The results show that the spectral bands with high values of R^2 were located in the VIS and SWIR regions. On the other hand, the predictive ability of individual spectral indices cannot be identified in the NIR range. The sensitive region combinations are found at wavelength around 1960–1990 nm and 2120–2030 nm for soil $EC_{1:5}$ lab on the surface. For soil $EC_{1:5}$ lab at 20 cm depth, the best combination is approximately in the band of 410–530 nm and 2170–2200 nm. Figure 3.10(b) displays the 2-D contour maps of R^2 between $NDSI_{i,j}$ and soil $EC_{1:5}$ lab on the surface (upper triangle), and soil $EC_{1:5}$ lab at 20 cm depth (lower triangle) for glutinous rice. Insignificant correlations between NDSI [i,j] and soil EC ($R^2 \leq 0.55$) were found. Large distributions of low correlation are dispensed almost over the entire region. Although the magnitude values of R^2 were less than 0.55, indicating a weak relationship, the potential spectral indices were selected for future study of the relationship between grain spectral reflectance of glutinous rice and soil EC.

3.7.5. Leaf spectral reflectance

The contour maps of R^2 values for the correlation of NDSIs [i,j] of leaf reflectance to soil EC in full range on *x* and *y* axes for jasmine rice and glutinous rice were qualified as shown in Figure 3.11(a) and Figure 3.11(b), respectively. Even though the R^2 values were less than 0.550, the potential $NDSI_{i,j}$ was chosen for further study of the relationship between leaf spectral reflectance of jasmine rice and soil EC. On the other hand, a number of better correlation band combinations of leaf spectral reflectance for glutinous rice were examined as displayed in Figure 7(*b*). The high value of R^2 was extracted at the wavelength approximately around 1040–1070 nm and 2280–2390 nm for $EC_{1:5}$ lab at 20 cm depth and $EC_{1:5}$ lab on the surface for glutinous rice, respectively.

3.7.6. Selected $NDSI_{i,j}$

$NDSI_{i,j}$ were selected according to the SLR analysis shown in Figure 3.9–Figure 3.11 as summarized in Table 3.7–Table 3.10. The selected $NDSI_{i,j}$ are based on specific spectral absorption band and statistical analyzes criteria such as high value of R^2, low RMSE,

and significant *p*-value. A factor that influences the spectral reflectance is located in some particular wavebands and absorbed different kind of plant features such as biophysical properties, biochemical properties, nutrient, and moistures. Also, the plant pigment is created by blue (430–490 nm), green (540–570 nm), and red (640–740 nm) wavebands. Moreover, water, carbon compounds (e.g. lignin and cellulose), and other biochemical properties (e.g. protein, nitrogen, starch, and sugars), located in NIR (740–1350 nm), and SWIR (1350–2500 nm), are also the factors influencing spectral variation of canopy, grain, and leaf of the rice. The detailed definitions and descriptions of these absorption bands were reported by Thenkabail et al. (2004). Specifically, the water absorption bands are situated around 970, 1450, and 1940 nm (Gao 1996). Based on the accuracy of field hyperspectral apparatus used in this study, the interval bandwidth of the selected $NDSI_{i,j}$ must not be less than 10 nm.

The selected $NDSI_{i,j}$ such as $NDSI_{485,498}$, $NDSI_{656,689}$, $NDSI_{651,690}$, and $NDSI_{417,520}$ are situated in a blue and the red waveband. These indices might have some important roles in the ecophysiological system that is directly or indirectly affects photosynthesis and chlorophyll content. In the case of canopy reflectance of jasmine rice, as shown in Table 3.7, the selected $NDSI_{656,689}$ shows a high correlation to soil $EC_{1:5}$ lab on the surface (R^2=0.602). Both R_{656} and R_{689} are located in the red spectrum absorption, which is sensitive to biomass specifically chlorophyll absorption (600–690 nm). In addition, the selected $NDSI_{i,j}$ such as $NDSI_{954,961}$, $NDSI_{1022,1033}$, $NDSI_{997,1136}$, $NDSI_{1039,1052}$, $NDSI_{713,1126}$, and $NDSI_{1045,1065}$ are located in NIR region which is related to water content. For example, $NDSI_{954,961}$, situated in the wavelength region of 900–970 nm, is considered as an indicator of plant water concentration (PWC) and successfully associated with leaf water content (Peñuelas et al. 1993; Peñuelas et al. 1997). This combination might have an effect on the canopy water content of jasmine rice. Besides the VIS and NIR regions, most of the wavelengths selected by the determination of $NDSIs_{i,j}$ were in the combination in SWIR region (see Table 3.7– Table 3.10, which is related to the plant moisture, plant biochemical, and carbon compounds.

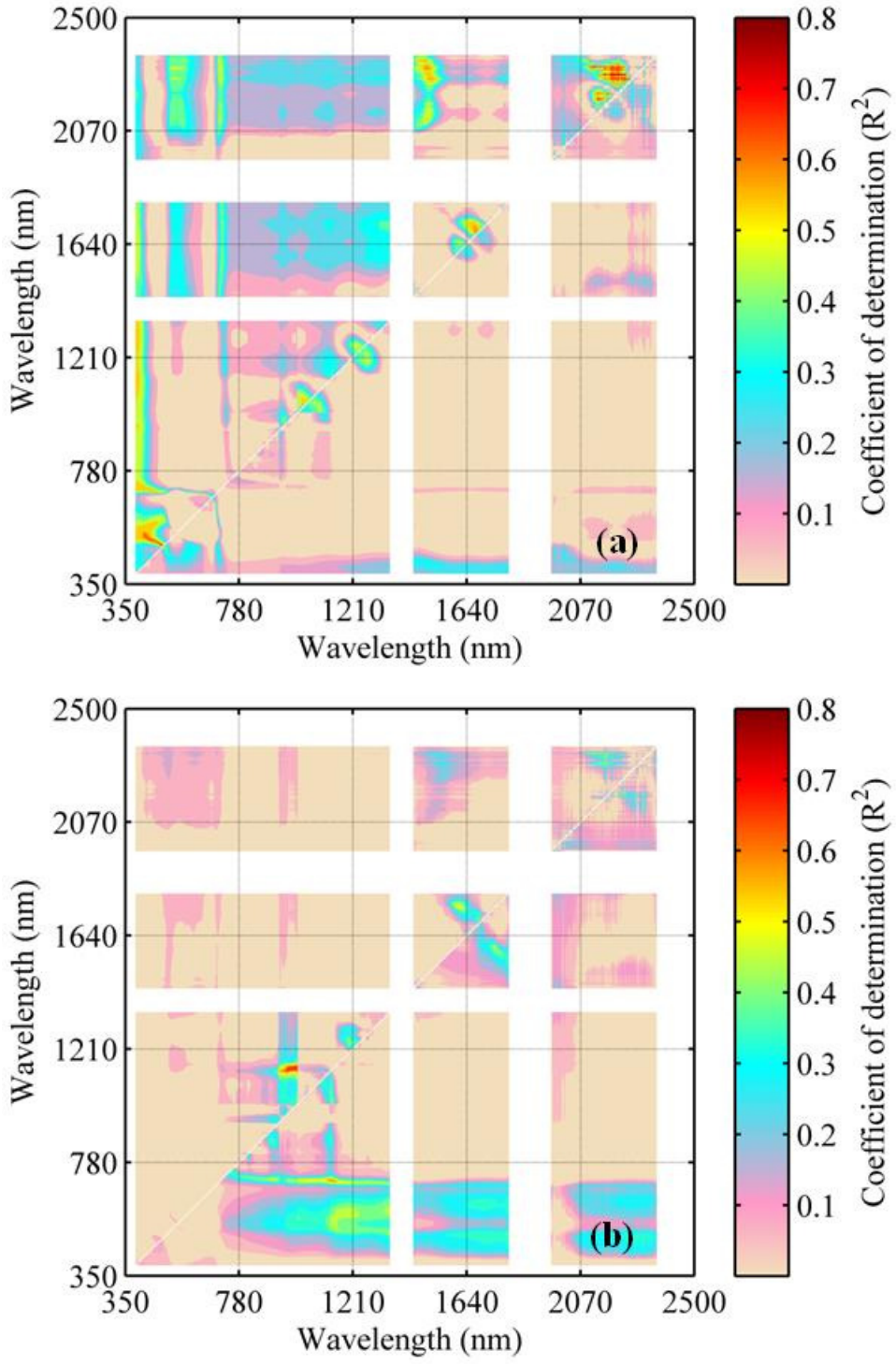

Figure 3.9 Contours of R^2 computed between $NDSIs_{i,j}$ of canopy reflectance and soil EC (upper triangle is of $EC_{1:5}$ lab on the surface and lower triangle is of $EC_{1:5}$ lab at 20 cm): (a) jasmine rice and (b) glutinous rice using the two separated wavelengths on x and y axes ranging from 350 to 2500 nm.

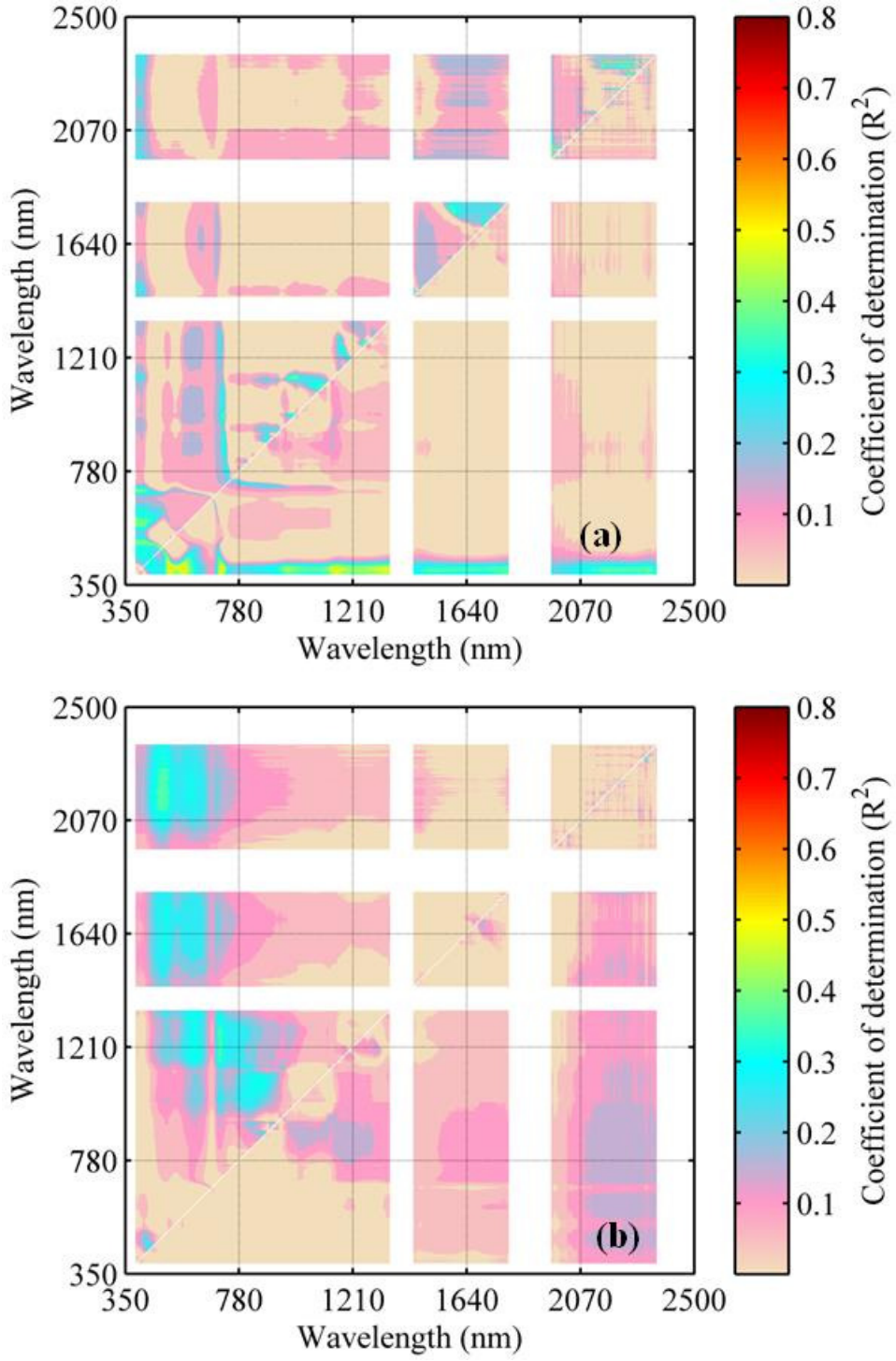

Figure 3.10 Contours of R^2 computed between $NDSIs_{i,j}$ of grain reflectance and soil EC (upper triangle is of $EC_{1:5}$ lab on the surface and lower triangle is of $EC_{1:5}$ lab at 20 cm): (a) jasmine rice and (b) glutinous rice using the two separated wavelengths on x and y axes ranging from 350 to 2500 nm.

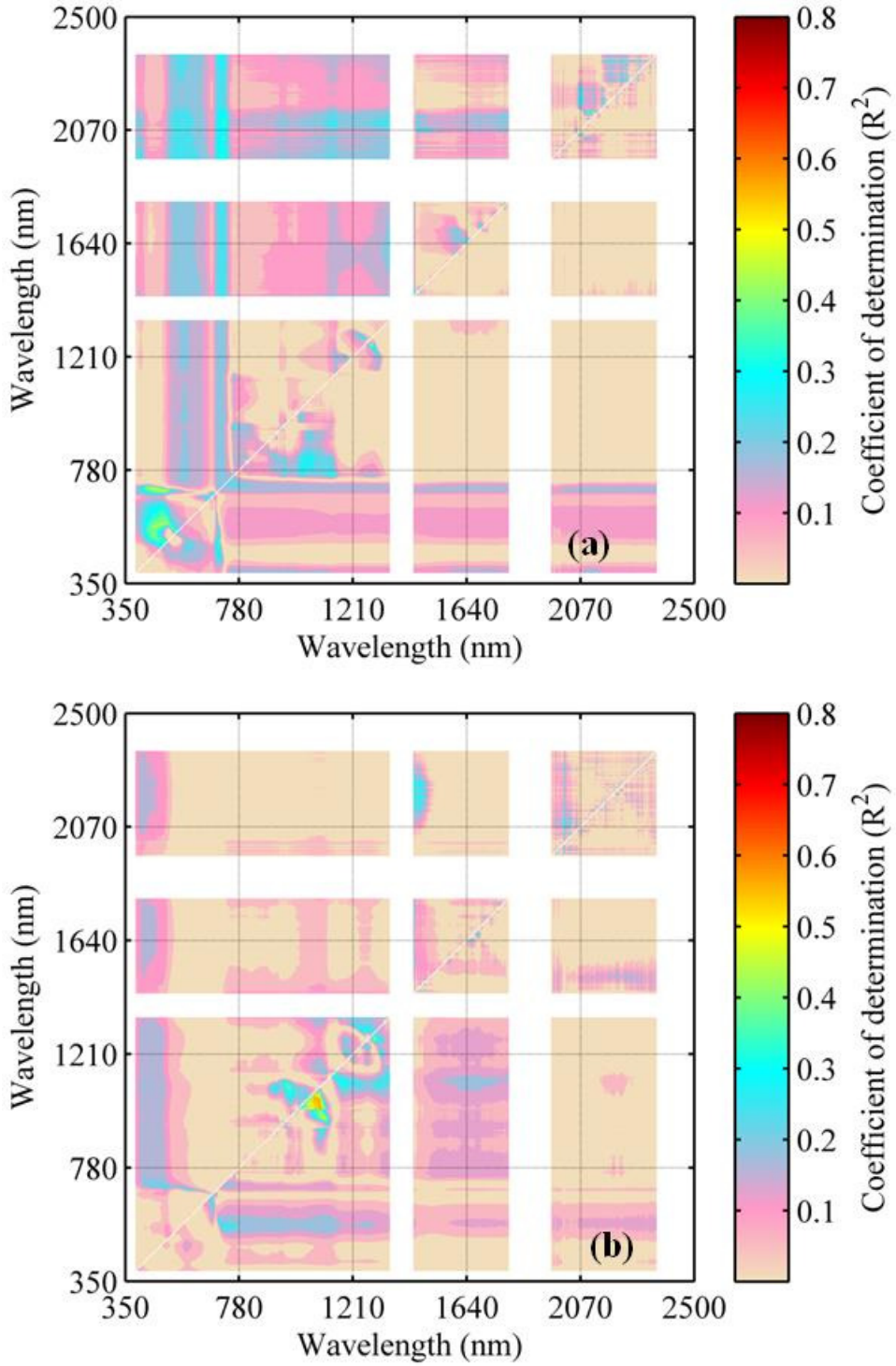

Figure 3.11 Contours of R^2 computed between $NDSIs_{i,j}$ of leaf reflectance and soil EC (upper triangle is of soil $EC_{1:5}$ lab on the surface and lower triangle is of soil $EC_{1:5}$ lab at 20 cm): (a) jasmine rice and (b) glutinous rice using the two separated wavelengths on x and y axes ranging from 350 to 2500 nm.

Table 3.7 Quantitative relationships of the soil $EC_{1:5}$ lab on the surface and soil EC_{field} to the selected spectral indices for jasmine rice.

Spectral indices	Soil $EC_{1:5}$ lab on the surface (dS/m) *				Soil EC_{field} (dS/m) **		
	Regression equation	R^2	RMSE	*p*-value	R^2	RMSE	*p*-value
Canopy reflectance measurements							
$NDSI_{485,498}$	y=0.025x-0.065	0.665	0.0068	1.153×10^{-5}	0.523	0.0081	2.300×10^{-4}
$NDSI_{656,689}$	y=0.021x-0.061	0.602	0.0065	5.818×10^{-5}	0.544	0.0071	1.690×10^{-4}
$NDSI_{954,961}$	y=-0.007x+0.002	0.521	0.0026	3.244×10^{-4}	0.599	0.0026	6.995×10^{-4}
$NDSI_{1022,1033}$	y=0.003x-0.009	0.649	0.0008	1.802×10^{-5}	0.660	0.0008	2.318×10^{-4}
$NDSI_{1675,1683}$	y=-0.002x+0.003	0.730	0.0005	1.580×10^{-6}	0.616	0.0006	5.271×10^{-4}
$NDSI_{2172,2211}$	y=0.012x-0.016	0.812	0.0022	5.806×10^{-8}	0.687	0.0030	1.336×10^{-4}
$NDSI_{2237,2283}$	y=-0.025x+0.080	0.836	0.0042	1.700×10^{-8}	0.702	0.0064	9.500×10^{-5}
Grain reflectance measurements							
$NDSI_{1969,1980}$	y=-0.025x-0.027	0.586	0.0081	8.00×10^{-8}	0.538	0.0093	1.850×10^{-3}
$NDSI_{2296,2328}$	y=0.026x+0.042	0.862	0.0041	3.484×10^{-9}	0.671	0.0070	1.900×10^{-4}
Leaf reflectance measurements							
$NDSI_{2319,2333}$	y=-0.008x+0.021	0.531	0.0030	2.700×10^{-3}	0.467	0.0038	4.940×10^{-3}

Notes: *p*-value is the probability value from F-distribution; RMSE is root mean square error; $NDSI_{i,j}$ is the normalized difference spectral index using the wavelengths i and j nm. The $NDSIs_{i,j}$ selected in this table were based on the contour map as shown in Figure 3.9–Figure 3.11.

* x = soil $EC_{1:5}$ lab on the surface / (dS/m); y = $NDSI_{i,j}$;** x =soil EC_{field} / (dS/m); y = $NDSI_{i,j}$

Table 3.8 Quantitative relationships of the soil $EC_{1:5}$ lab on the surface and soil EC_{field} to the selected spectral indices for glutinous rice.

Spectral indices	Soil $EC_{1:5}$ lab on the surface (dS/m) *				Soil EC_{field} (dS/m) **		
	Regression equation	R^2	RMSE	*p*-value	R^2	RMSE	*p*-value
Canopy reflectance measurements							
$NDSI_{997,1136}$	y=-0.042x-0.044	0.724	0.0068	1.940×10^{-6}	0.317	0.0107	9.720×10^{-3}
$NDSI_{1688,1698}$	y=-0.002x+0.005	0.661	0.0004	1.288×10^{-5}	0.182	0.0007	6.032×10^{-2}
$NDSI_{2161,2329}$	y=-0.021x+0.122	0.676	0.0038	8.575×10^{-6}	0.170	0.0024	3.720×10^{-4}
Grain reflectance measurements							
$NDSI_{2147,2175}$	y=-0.005x-0.023	0.395	0.0016	3.020×10^{-3}	0.057	0.0021	3.118×10^{-1}
Leaf reflectance measurements							
$NDSI_{2290,2370}$	y=0.024x+0.124	0.559	0.0058	2.320×10^{-4}	0.341	0.0071	8.510×10^{-3}

Notes: *p*-value is the probability value from F-distribution; RMSE is root mean square error; $NDSI_{i,j}$ is the normalized difference spectral index using the wavelengths i and j nm. The $NDSIs_{i,j}$ selected in this table were based on the contour map as shown in Figure 3.9–Figure 3.11.

* x = soil $EC_{1:5}$ lab on the surface / (dS/m); y = $NDSI_{i,j}$;** x =soil EC_{field} / (dS/m); y = $NDSI_{i,j}$

Table 3.9 Quantitative relationships of the soil $EC_{1:5}$ lab at 20 cm depth and soil EC_{field} to the selected spectral indices for jasmine rice.

Spectral indices	Soil $EC_{1:5}$ lab at 20 cm depth (dS/m)*				Soil EC_{field} (dS/m) **		
	Regression equation	R^2	RMSE	*p*-value	R^2	RMSE	*p*-value
Canopy reflectance measurements							
$NDSI_{651,690}$	y=0.045x-0.071	0.528	0.0080	2.83×10^{-4}	0.477	0.0092	4.33×10^{-3}
$NDSI_{1039,1052}$	y=0.005x-0.01	0.578	0.0009	9.88×10^{-5}	0.490	0.0010	3.65×10^{-3}
$NDSI_{2290,2312}$	y=-0.025x+0.038	0.673	0.0034	9.37×10^{-6}	0.457	0.0042	6.63×10^{-3}
Grain reflectance measurements							
$NDSI_{417,520}$	y=0.179x-0.645	0.551	0.0304	1.76×10^{-4}	0.211	0.0401	8.47×10^{-2}
$NDSI_{2180,2193}$	y=-0.017x-0.004	0.569	0.0028	1.21×10^{-4}	0.300	0.0040	3.49×10^{-2}
Leaf reflectance measurements							
$NDSI_{1256,1283}$	y=0.002x+0.0001	0.492	0.0004	5.60×10^{-4}	0.156	0.0006	1.44×10^{-1}

Notes: *p*-value is the probability value from F-distribution; RMSE is root mean square error; $NDSI_{i,j}$ is the normalized difference spectral index using the wavelengths i and j nm. The $NDSIs_{i,j}$ selected in this table were based on the contour map as shown in Figure 3.9–Figure 3.11.

* x = soil $EC_{1:5}$ lab at 20 cm depth / (dS/m); y = $NDSI_{i,j}$;** x =soil EC_{field} / (dS/m); y = $NDSI_{i,j}$

Table 3.10 Quantitative relationships of the soil $EC_{1:5}$ lab at 20 cm depth and soil EC_{field} to the selected spectral indices for glutinous rice.

Spectral indices	Soil $EC_{1:5}$ lab at 20 cm depth (dS/m)*				Soil EC_{field} (dS/m) **		
	Regression equation	R^2	RMSE	*p*-value	R^2	RMSE	*p*-value
Canopy reflectance measurements							
$NDSI_{713,1126}$	y=-0.296x-0.299	0.614	0.0159	4.32×10^{-5}	0.274	0.0218	1.78×10^{-2}
$NDSI_{2179,2233}$	y=-0.034x+0.003	0.599	0.0019	6.10×10^{-5}	0.195	0.0026	5.10×10^{-2}
Grain reflectance measurements							
$NDSI_{2321,2331}$	y=-0.080x+0.019	0.310	0.0081	1.07×10^{-2}	0.177	0.0088	6.44×10^{-2}
Leaf reflectance measurements							
$NDSI_{1045,1065}$	y=-0.011x-0.005	0.613	0.0006	7.34×10^{-5}	0.093	0.0009	2.03×10^{-1}

Notes: *p*-value is the probability value from F-distribution; RMSE is root mean square error; $NDSI_{i,j}$ is the normalized difference spectral index using the wavelengths i and j nm. The $NDSIs_{i,j}$ selected in this table were based on the contour map as shown in Figure 3.9–Figure 3.11.

* x = soil $EC_{1:5}$ lab at 20 cm depth / (dS/m); y = $NDSI_{i,j}$;** x =soil EC_{field} / (dS/m); y = $NDSI_{i,j}$

3.7.7. Validation of selected $NDSI_{i,j}$ with soil EC_{field}

To test the new selected spectral indices were reliable and applicable, the selected NDSI [i,j] was used to correlate with another independent data sets of soil EC (soil EC_{field}) measured from portable EC meter. Soil EC_{field} was taken from the same field investigation for selecting the paddy fields with the desired ranges of EC value as shown in Table 3.7– Table 3.10 for both jasmine rice and glutinous rice, respectively. Three statistical parameters were used for evaluation such as R^2, RMSE, and *p*-value. Only the selected $NDSI_{i,j}$ derived from the correlation between reflectance of canopy, grain, and leaf of rice with soil $EC_{1:5}$ lab on the surface is referred to because soil EC_{field} measured at the depth about 5 cm below the surface is better associated with soil $EC_{1:5}$ lab on the surface than soil $EC_{1:5}$ lab at 20 cm depth. Based on the preliminary analysis reported by Touch et al.(2013; 2013), soil $EC_{1:5}$ lab at 20 cm depth had shown a weak correlation with rice plants. Therefore, the validation of the spectral index taken from the selected $NDSI_{i,j}$ based on soil $EC_{1:5}$ lab at 20 cm depth is not persuasive (see Table 3.9 and Table 3.10).

Accordingly, Figure 3.12 and Figure 3.13 illustrate the most significant correlations between soil EC ($EC_{1:5}$ lab on the surface and soil EC_{field}) and the selected NDSI [i,j] of canopy reflectance of jasmine rice and glutinous rice, respectively. The similar tendency in negative correlations were found between $NDSI_{2237,2283}$ and soil EC for jasmine rice, as indicated in Figure 3.12(a) for $EC_{1:5}$ lab on the surface (R^2=0.836 and RMSE= 0.0042), Figure 3.12 (b) for soil EC_{field} (R^2 =0.702 and RMSE= 0.0064). There is also negative linear correlation of the scatter plot between soil EC and $NDSI_{997,1136}$ for glutinous rice as displayed in Figure 3.13. The best correlation with soil $EC_{1:5}$ lab on the surface (R^2 = 0.724 and RMSE= 0.0068) are presented in Figure 3.13(a). On the other hand, $NDSI_{997,1136}$ is poorly correlated with soil EC_{field} (R^2=0.317 and RMSE= 0.0107) as shown in Figure 3.13(b). This result indicates that the selected $NDSI_{997,1136}$ might, not a good spectral indicator used to estimate the amount of salt concentrated in the soil for field investigation.

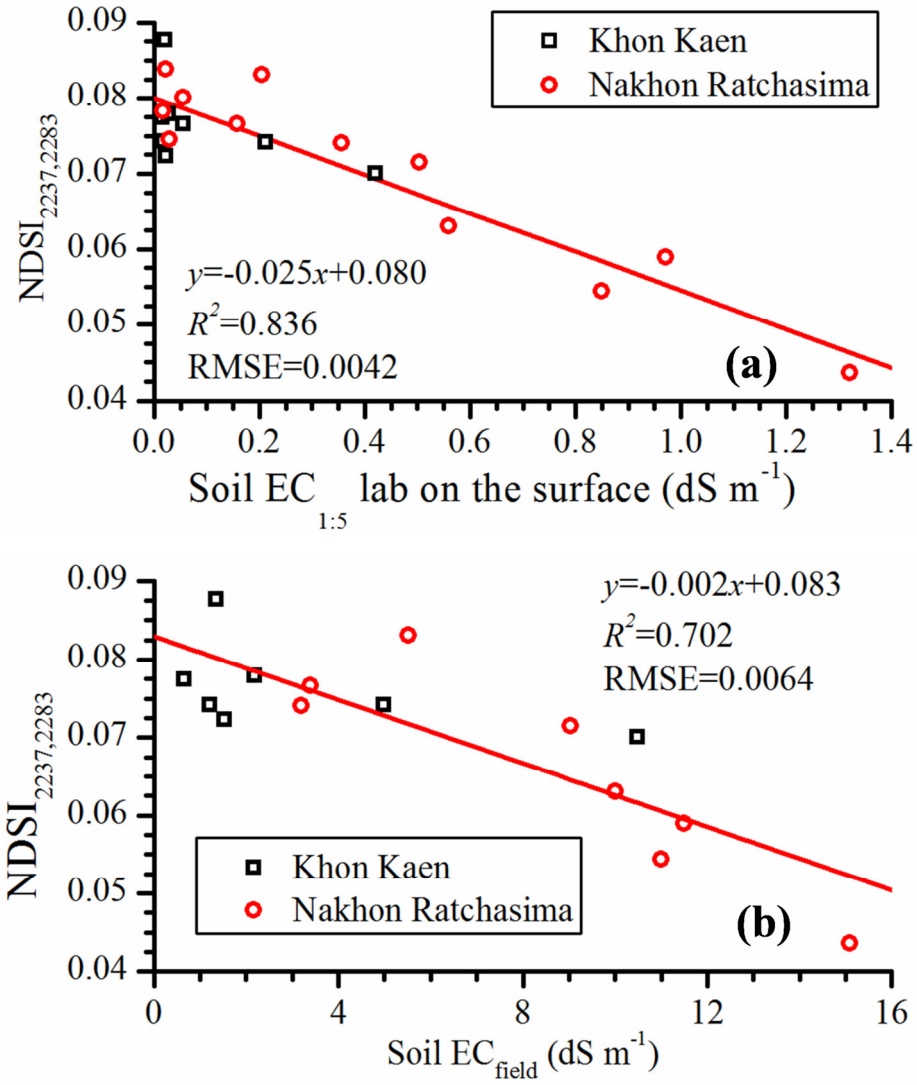

Figure 3.12 Relationships between soil EC and canopy spectral indices $NDSI_{2237, 2283}$ for jasmine rice: (a) soil $EC_{1:5}$ lab on the surface and (b) soil EC_{field}.

The best correlation between $NDSI_{i,j}$ and soil EC for grain reflectance of jasmine rice and glutinous rice are displayed in Figure 3.14 and Figure 3.15, respectively. For jasmine rice, the SLR analysis reveals the similar tendency in positive linear correlation for $NDSI_{2296,2328}$ between soil $EC_{1:5}$ lab on the surface (R^2= 0.862 and RMSE= 0.0041) and soil EC_{field} (R^2=0.671 and RMSE= 0.0070) as shown in Figure 3.14(a) and Figure 3.14(b), respectively. On the other hand, Figure 3.15 illustrates the similar tendency in negative linear relationship between soil EC and $NDSI_{2147,2175}$ obtained from the data set of glutinous rice. Figure 3.15(a) and Figure 3.15(b) exhibit the correlation between $NDSI_{2147, 2175}$ and soil $EC_{1:5}$ lab on the surface (R^2= 0.395 and RMSE= 0.0016) and soil

EC_{field} (R^2=0.057 and RMSE= 0.0021), respectively. Consequently, the chosen pairs of spectral wavelengths R_{2147} and R_{2175} for glutinous rice located in the SWIR regions might not be suitable spectral indices for soil EC determination of both fields and laboratory. The predictive spectral index could not be reasonably acceptable for grain spectral reflectance of glutinous rice. However, this selected NDSI [i,j] is tentative spectral index for further study.

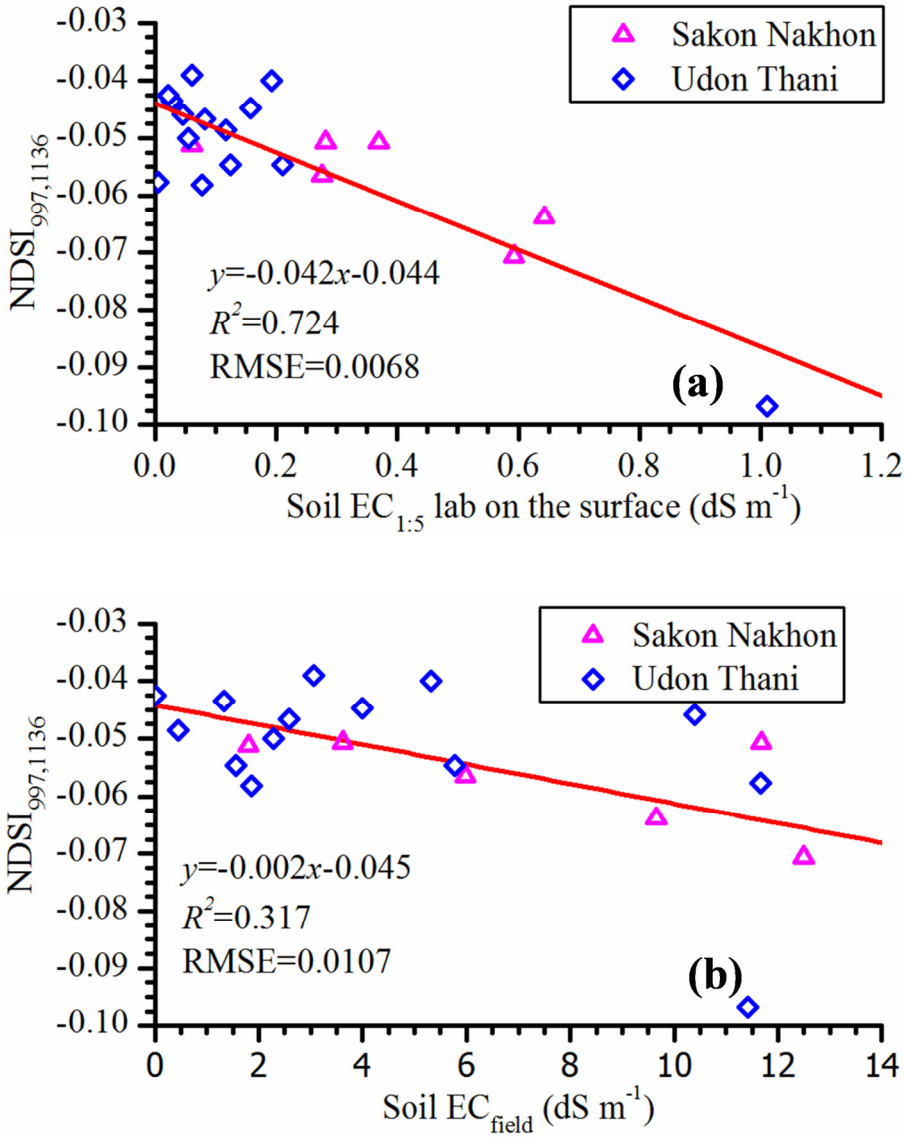

Figure 3.13 Relationships between soil EC and canopy spectral indices $NDSI_{997, 1136}$ for glutinous rice: (a) soil $EC_{1:5}$ lab on the surface and (b) soil EC_{field}.

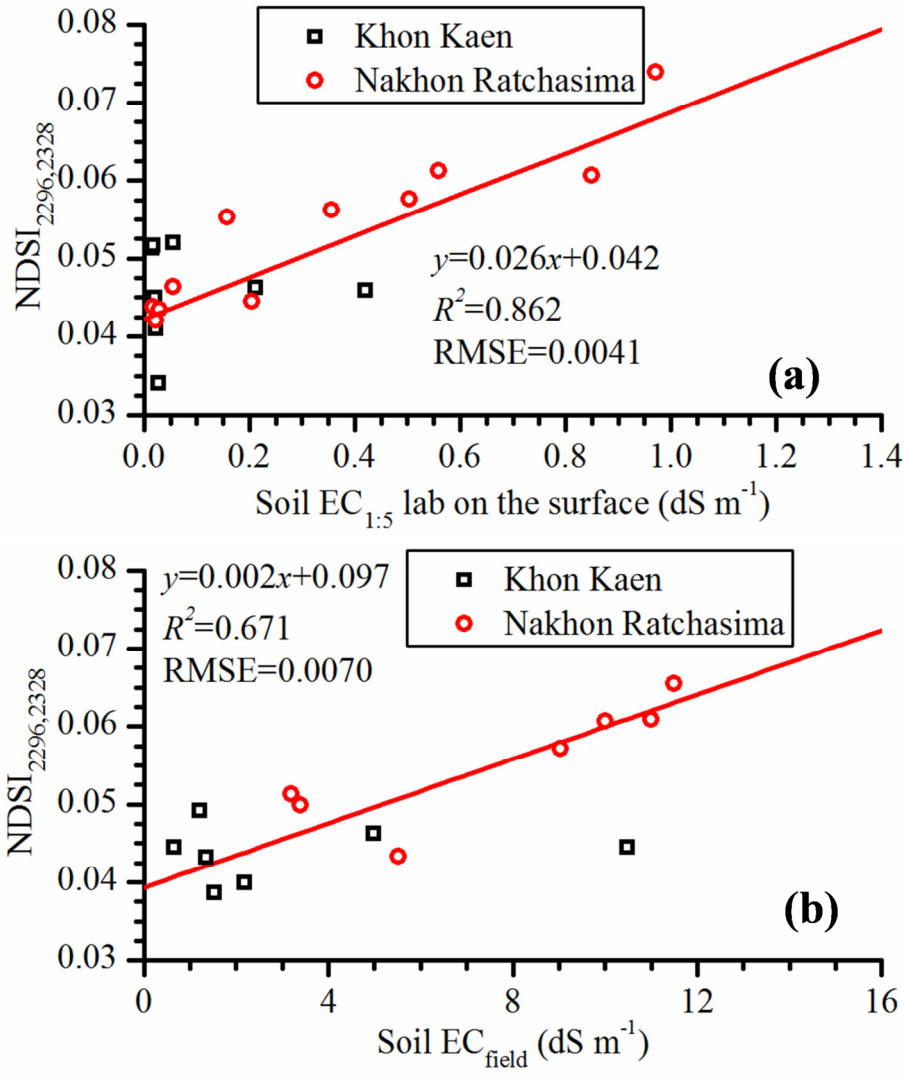

Figure 3.14 Relationships between soil EC and grain spectral indices $NDSI_{2296, 2328}$ for jasmine rice: (a) soil $EC_{1:5}$ lab on the surface and (b) soil EC_{field}.

In the same manner, Figure 3.16 and Figure 3.17 present the quantitative relationship between $NDSI_{i,j}$ taken from the leaf reflectance measurement and soil EC ($EC_{1:5}$ lab on the surface and soil EC_{field}) for both jasmine rice and glutinous rice, respectively. Figure 3.16(a) and Figure 3.16(b) illustrate the similar tendency in negative linear relationship of the selected $NDSI_{2319,2333}$ for jasmine rice with soil $EC_{1:5}$ lab on the surface (R^2=0.531 and RMSE=0.0030) and soil EC_{field} (R^2= 0.467 and RMSE=0.0038), respectively. Low magnitude value of R^2 ($R^2 \leq 0.550$) was found for this correlation; hence, $NDSI_{2319,2333}$ might not be a suitable spectral index to examine the degree of soil salinity for field and laboratory investigations. A bandwidth of wavelengths 2290 nm and 2370 nm give the

similar tendency in positive linear correlation with soil $EC_{1:5}$ lab on the surface (R^2=0.559 and RMSE=0.0058) and soil EC_{field} (R^2=0.341 and RMSE=0.0071) as shown in Figure 3.17(a) and Figure 3.17(b), respectively. Therefore, $NDSI_{2290,2370}$ might not be a good spectral index because this spectral index is poorly correlated with soil EC_{field} even though it has a good correlation with soil $EC_{1:5}$ lab on the surface (R^2 =0.559).

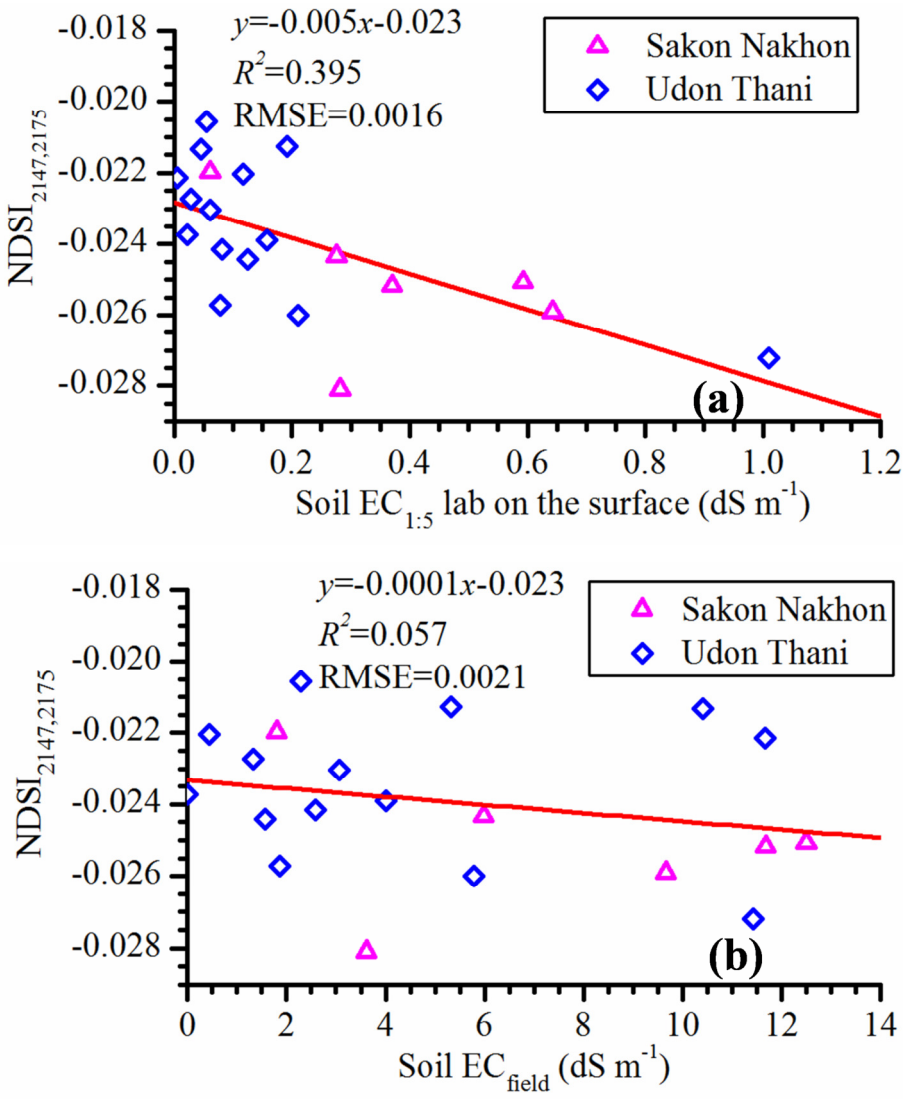

Figure 3.15 Relationships between soil EC and grain spectral indices $NDSI_{2147, 2175}$ for glutinous rice: (a) soil $EC_{1:5}$ lab on the surface and (b) soil EC_{field}.

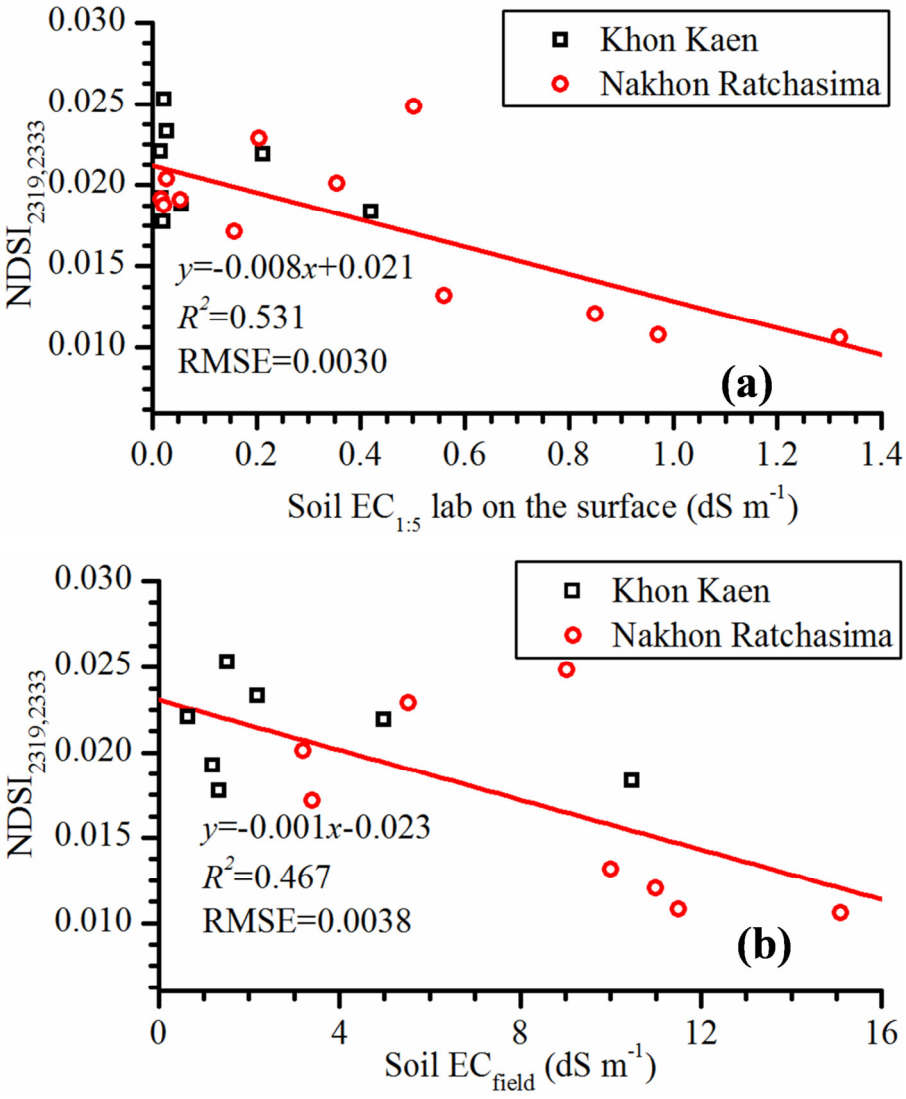

Figure 3.16 Relationships between soil EC and leaf spectral indices $NDSI_{2319,2333}$ for jasmine rice: (a) soil $EC_{1:5}$ lab on the surface and (b) soil EC_{field}.

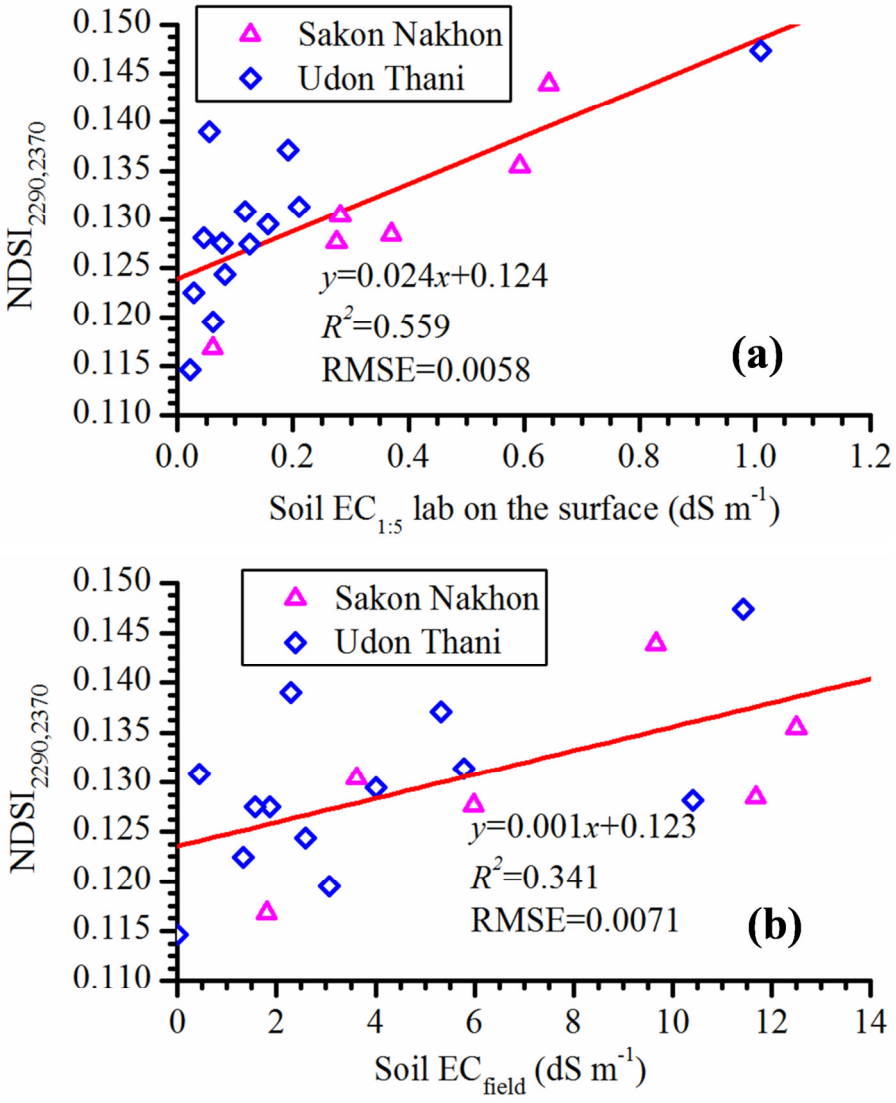

Figure 3.17 Relationships between soil EC and leaf spectral indices $NDSI_{2290, 2370}$ for glutinous rice: (a) soil $EC_{1:5}$ lab on the surface and (b) soil EC_{field}.

3.7.8. Comparison of the present spectral indices with conventional indices

The comprehensive studies were carried out to examine the relationships of soil $EC_{1:5}$ lab on the surface and soil $EC_{1:5}$ lab at 20 cm depth using the conventional spectral indices referred by previous researchers for canopy, grain, and leaf reflectance measurement, such as Photochemical Reflectance Index (PRI), Normalised Phaeophytinisation Index (NPQI), Normalised Difference Water Index (NDWI), Normalised Pigment Chlorophyll Index (NPCI), Normalised Difference Vegetation Index (NDVI), Water Index (WI), and Cellulose Absorption Index (CAI). Table 3.11

and Table 3.12 have adopted the previously reported spectral indices to evaluate the R^2 for correlating with the soil EC to both jasmine rice and glutinous rice conducted in this study, respectively. The results revealed that all conventional spectral indices were poorly correlated either with $EC_{1:5}$ lab on the surface or soil $EC_{1:5}$ lab at 20 cm depth for both jasmine and glutinous rice, because most conventional indices were examined using measurements from broadband. Nevertheless, most of those broadband limit the extensive exploitation of particular narrowband while hyperspectral measurements allow broader optimum selection of the most significant wavelengths.

3.8. Discussions

High level of soil salinity could harmfully impact the ripening stages of the jasmine rice and glutinous rice such as crop length, panicle length, canopy openness, and LAI. Even though the results from SLR analysis could not provide very high significant correlation for some rice parameters, the tendency of negative slope could be used to confirm the effect of soil salinity on the ripening stages of rice. So far, rare previous researches have explicitly examined the relationship between soil EC and reflectance of vegetation. However, the correlations between soil reflectance with soil EC have investigated by previous researchers such as Islam et al.(2003), Farifteh et al.(2007), and Mashimbye (2013). Leone et al. (2007) suggested that the VIS and NIR spectral regions are very important for analyzing plant spectral behaviors. Notably, most of the high correlations between $NDSI_{i,j}$ are found in NIR and SWIR region that are also convinced by Farifteh et al. (2007) and Mashimbye (2013). These previous studies help assure the selected spectral indices obtained in the present study, and are useful in exploring the relationship between soil EC and reflectance of canopy, grain, and leaf of rice under different salinity levels because the selected $NDSI_{i,j}$ are consistently located in the VIS, NIR, and SWIR.

Table 3.11 Relationships between soil EC to the conventional indices for jasmine rice.

Vegetation indices	Soil $EC_{1:5}$ lab on the surface (dS/m) (R^2)	Soil $EC_{1:5}$ lab at 20 cm depth (dS/m)
Canopy reflectance measurements		
PRI: $[R_{531}-R_{570}]/[R_{531}+R_{570}]$	0.002	0.004
NPQI: $[R_{415}-R_{435}]/[R_{415}+R_{435}]$	0.301	0.056
NDWI: $[R_{860}-R_{1240}]/[R_{860}+R_{1240}]$	0.113	0.016
NPCI: $[R_{680}-R_{430}]/(R_{680}+R_{430}]$	0.079	0.062
NDVI: $[R_{830}-R_{660}]/[R_{830}+R_{660}]$	0.004	0.000
NDVI: $[R_{800}-R_{670}]/[R_{800}+R_{670}]$	0.008	0.000
NDVI: $[R_{750}-R_{705}]/[R_{750}+R_{705}]$	0.019	0.047
NDVI: $[R_{900}-R_{680}]/[R_{900}+R_{680}]$	0.008	0.001
WI: $[R_{970}/R_{900}]$	0.149	0.007
CAI: $[0.5(R_{2000}+R_{2200})-R_{2100}]$	0.486	0.165
Grain reflectance measurements		
PRI: $[R_{531}-R_{570}]/[R_{531}+R_{570}]$	0.156	0.079
NPQI: $[R_{415}-R_{435}]/[R_{415}+R_{435}]$	0.290	0.323
NDWI: $[R_{860}-R_{1240}]/[R_{860}+R_{1240}]$	0.006	0.084
NPCI: $[R_{680}-R_{430}]/(R_{680}+R_{430}]$	0.196	0.128
NDVI: $[R_{830}-R_{660}]/[R_{830}+R_{660}]$	0.141	0.053
NDVI: $[R_{800}-R_{670}]/[R_{800}+R_{670}]$	0.138	0.049
NDVI: $[R_{750}-R_{705}]/[R_{750}+R_{705}]$	0.172	0.088
NDVI: $[R_{900}-R_{680}]/[R_{900}+R_{680}]$	0.144	0.052
WI: $[R_{970}/R_{900}]$	0.022	0.082
CAI: $[0.5(R_{2000}+R_{2200})-R_{2100}]$	0.092	0.017
Leaf reflectance measurements		
PRI: $[R_{531}-R_{570}]/[R_{531}+R_{570}]$	0.293	0.178
NPQI: $[R_{415}-R_{435}]/[R_{415}+R_{435}]$	0.030	0.037
NDWI: $[R_{860}-R_{1240}]/[R_{860}+R_{1240}]$	0.014	0.030
NPCI: $[R_{680}-R_{430}]/(R_{680}+R_{430}]$	0.133	0.107
NDVI: $[R_{830}-R_{660}]/[R_{830}+R_{660}]$	0.119	0.083
NDVI: $[R_{800}-R_{670}]/[R_{800}+R_{670}]$	0.084	0.071
NDVI: $[R_{750}-R_{705}]/[R_{750}+R_{705}]$	0.231	0.203
NDVI: $[R_{900}-R_{680}]/[R_{900}+R_{680}]$	0.074	0.069
WI: $[R_{970}/R_{900}]$	0.034	0.010
CAI: $[0.5(R_{2000}+R_{2200})-R_{2100}]$	0.482	0.095

Table 3.12 Relationships between soil EC to the conventional indices for glutinous rice.

Vegetation indices	Soil $EC_{1:5}$ lab on the surface (dS/m)	Soil $EC_{1:5}$ lab at 20 cm depth (dS/m)
	(R^2)	
Canopy reflectance measurements		
PRI: $[R_{531}-R_{570}]/[R_{531}+R_{570}]$	0.053	0.005
NPQI: $[R_{415}-R_{435}]/[R_{415}+R_{435}]$	0.001	0.087
NDWI: $[R_{860}-R_{1240}]/[R_{860}+R_{1240}]$	0.033	0.040
NPCI: $[R_{680}-R_{430}]/(R_{680}+R_{430}]$	0.008	0.045
NDVI: $[R_{830}-R_{660}]/[R_{830}+R_{660}]$	0.003	0.116
NDVI: $[R_{800}-R_{670}]/[R_{800}+R_{670}]$	0.002	0.091
NDVI: $[R_{750}-R_{705}]/[R_{750}+R_{705}]$	0.005	0.166
NDVI: $[R_{900}-R_{680}]/[R_{900}+R_{680}]$	0.003	0.124
WI: $[R_{970}/R_{900}]$	0.038	0.046
CAI: $[0.5(R_{2000}+R_{2200})-R_{2100}]$	0.138	0.188
Grain reflectance measurements		
PRI: $[R_{531}-R_{570}]/[R_{531}+R_{570}]$	0.002	0.053
NPQI: $[R_{415}-R_{435}]/[R_{415}+R_{435}]$	0.070	0.001
NDWI: $[R_{860}-R_{1240}]/[R_{860}+R_{1240}]$	0.209	0.158
NPCI: $[R_{680}-R_{430}]/(R_{680}+R_{430}]$	0.005	0.001
NDVI: $[R_{830}-R_{660}]/[R_{830}+R_{660}]$	0.051	0.002
NDVI: $[R_{800}-R_{670}]/[R_{800}+R_{670}]$	0.019	0.005
NDVI: $[R_{750}-R_{705}]/[R_{750}+R_{705}]$	0.066	0.002
NDVI: $[R_{900}-R_{680}]/[R_{900}+R_{680}]$	0.028	0.005
WI: $[R_{970}/R_{900}]$	0.148	0.173
CAI: $[0.5(R_{2000}+R_{2200})-R_{2100}]$	0.020	0.019
Leaf reflectance measurements		
PRI: $[R_{531}-R_{570}]/[R_{531}+R_{570}]$	0.007	0.107
NPQI: $[R_{415}-R_{435}]/[R_{415}+R_{435}]$	0.008	0.000
NDWI: $[R_{860}-R_{1240}]/[R_{860}+R_{1240}]$	0.025	0.058
NPCI: $[R_{680}-R_{430}]/(R_{680}+R_{430}]$	0.099	0.007
NDVI: $[R_{830}-R_{660}]/[R_{830}+R_{660}]$	0.022	0.061
NDVI: $[R_{800}-R_{670}]/[R_{800}+R_{670}]$	0.017	0.026
NDVI: $[R_{750}-R_{705}]/[R_{750}+R_{705}]$	0.013	0.179
NDVI: $[R_{900}-R_{680}]/[R_{900}+R_{680}]$	0.013	0.020
WI: $[R_{970}/R_{900}]$	0.083	0.091
CAI: $[0.5(R_{2000}+R_{2200})-R_{2100}]$	0.010	0.014

Notes: Photochemical Reflectance Index (PRI), Normalized Phaeophytinisation Index (NPQI), Normalized Difference Water Index (NDWI), Normalized Pigment Chlorophyll Index (NPCI), Normalized Difference Vegetation Index (NDVI), Water Index (WI), and Cellulose Absorption Index (CAI).

As the performance of the current apparatus is insufficiently progressed, some of the selected spectral indices located in cellulose absorption might not well represent the persuasive spectral bands. The analysis in this particular wavelength needs the very high accuracy of measurement with the order less than 0.1 nm (Nakaji 2009). In addition, previous studies have indicated that the relationship between plant isotopic compositions, in particular, cellulose and salinity, is complicated, and thus careful analysis is essential before making an interpretation. In addition, cellulose did not vary directly with salinity as observed with many plants (Ish-Shalom-Gordon et al. 1992; Ellsworth and Sternberg 2014).

3.9. Conclusions

The statistical analyzes revealed that the changes in electrical conductivity (EC) of soil were significantly sensitive to the ripening stages of jasmine rice and glutinous rice planted at different levels of soil salinity. Relationships between soil EC and reflectance of canopy, grain, and leaf of rice have been determined by simple linear regression (SLR) analysis. The highest correlations are found in the near infrared (NIR) and shortwave infrared (SWIR). The correlations between reflectance of canopy, grain, and leaf of rice and soil EC were found to be increased from the visible (VIS) through the shortwave infrared (SWIR) regions of the spectrum. Among reflectance measurements, canopy reflectance was highly correlated with soil EC.

The achieved result would be essential for air- or space-borne remote sensing applied to detect the saline soil in large areas of farmland. However, the estimated accuracies of relationship between soil EC and reflectance of glutinous rice were relatively lower than those of jasmine rice and may not be suitable for estimating soil EC in saline conditions. From SLR analysis, $NDSI_{i,j}$ using field hyperspectral technique gave coefficient of determinations (R^2) larger than conventional vegetation indices.

Reflectance of canopy, grain, and leaf of rice in northeastern Thailand during the ripening season just before harvest were examined in an attempt to realise the applications of the field hyperspectral technique for monitoring the spread of saline soils and estimation of the effects of soil salinity on rice plants. Nevertheless, from a remote sensing perspective, the relationships to spectral variables are not substantially strong; therefore, this deficiency demands detailed investigations in the subsequent researches after this early report.

CHAPTER 4 THE RELATIONSHIP BETWEEN ELECTRICAL CONDUCTIVITY OF SOIL AND REFLECTANCE OF THE SOIL IN NORTHEASTERN THAILAND

4.1. Introduction

Saline- or salt-affected soils are prevalent in both arid and semi-arid regions, with high levels of evapotranspiration and irrigated agriculture (Gleick 1993). Conventional methods of monitoring changes in soil salinity are based on field observation and laboratory analyzes of both crops and soils. This is mostly done by measuring the electrical conductivity (EC) of the soil solution as well as the exchangeable sodium percentage (ESP) and pH. However, these methods are time-consuming, expensive, and restricted to certain areas. Reflectance spectroscopy is one of the fastest-growing analytical technologies globally, with an overwhelming application in virtually all the fields of science. In general, all compounds exhibit absorption/emission spectra that can be analyzed both quantitatively and qualitatively. Specifically, visible–near infrared–shortwave infrared spectra (VIS–NIR–SWIR: 400–2500 nm) provide key aspects of both organic and inorganic matter that constitute invaluable diagnostic information for environmental scientists. In this research, soil reflectance is proposed to predict the electrical conductivity (EC) of the soil sample taken near the surface and at 20 cm depth.

This chapter aims to investigate the relationships between electrical conductivity of soil and reflectance of soil in northeastern Thailand. Besides the hyperspectral data taken from the rice, the experiment was also conducted for reflectance of soil. It is very important to understand the relationship between soil salinity and soil reflectance. In addition, some additional chemical component that used to determinate the salt content is also included in this chapter.

4.2. Materials and Methods

4.2.1. Sites and soil sampling

In Nakhon Ratchasima province (Kham Thale So district), as shown in Figure 4.1, bare

land and abandoned land caused by salt pan and drainage of salt can be seen in the heavily affected areas where only salt-tolerant plants (cactus, acacia, and palm) can live. In Khon Kaen province (Ban Phai district), as illustrated in Figure 4.2, despite of the low-yield rice field, farmers grow acacias or locust trees to help absorb salinity around paddy fields. Heavily damaged lands, where even grass is dying, are being improved by planting acacia (Australian species) with adequate irrigation system. In Sakon Nakhon province (Phang Khon district) presented in Figure 4.3, some abandoned lands are utilized by planting eucalyptus. The price of sticky rice, better than that of Jasmine rice, was unusual in the year 2010; for this reason, farmers still produced sticky rice in low yield paddy fields though rice continued dying during harvest period. In Udon Thani province (Ban Dung district), as demonstrated in Figure 4.4 where salt mine is still under operation during the dry season, villagers grow rice and operate salt pan nearby, separating both from buffer areas. Variations in the salinity found in rice fields near salt farms with an appearance of earthworm indicating enriched soil and yellow-eyed grass indicating salty soil in the paddy field. At each site, soil core samples were taken from composite topsoil with sample layers of 5 cm and the subsurface layer at the depth of 20 cm. The sampling sites were selected based on the desired variation using EC portable meter. Each soil sample was mixed, turning to one homogeneous sample of each location.

Figure 4.1 Affected rice field from drainage of salt pan at Nakhon Ratchasima province

Figure 4.2 Low yield rice field at Khon Kaen province with appearance of salt crust

Figure 4.3 Low yield paddy field during harvest period in Sakon Nakhon province

Figure 4.4 Variation of salinity found in rice fields near salt farm in Udon Thani province

4.2.2. Soil reflectance measurement

After conduct, the field hyperspectral measurements of rice, the spectral reflectance of soil was conducted. The sensor was point about 5 cm above the soil sample samples were taken from composite topsoil with sample layers of 5 cm and the subsurface layer at the depth of 20 cm as shown in Figure 4.5.

Figure 4.5 Field measurement: (a) soil reflectance measurement, and (b) calibration with ceramic pad.

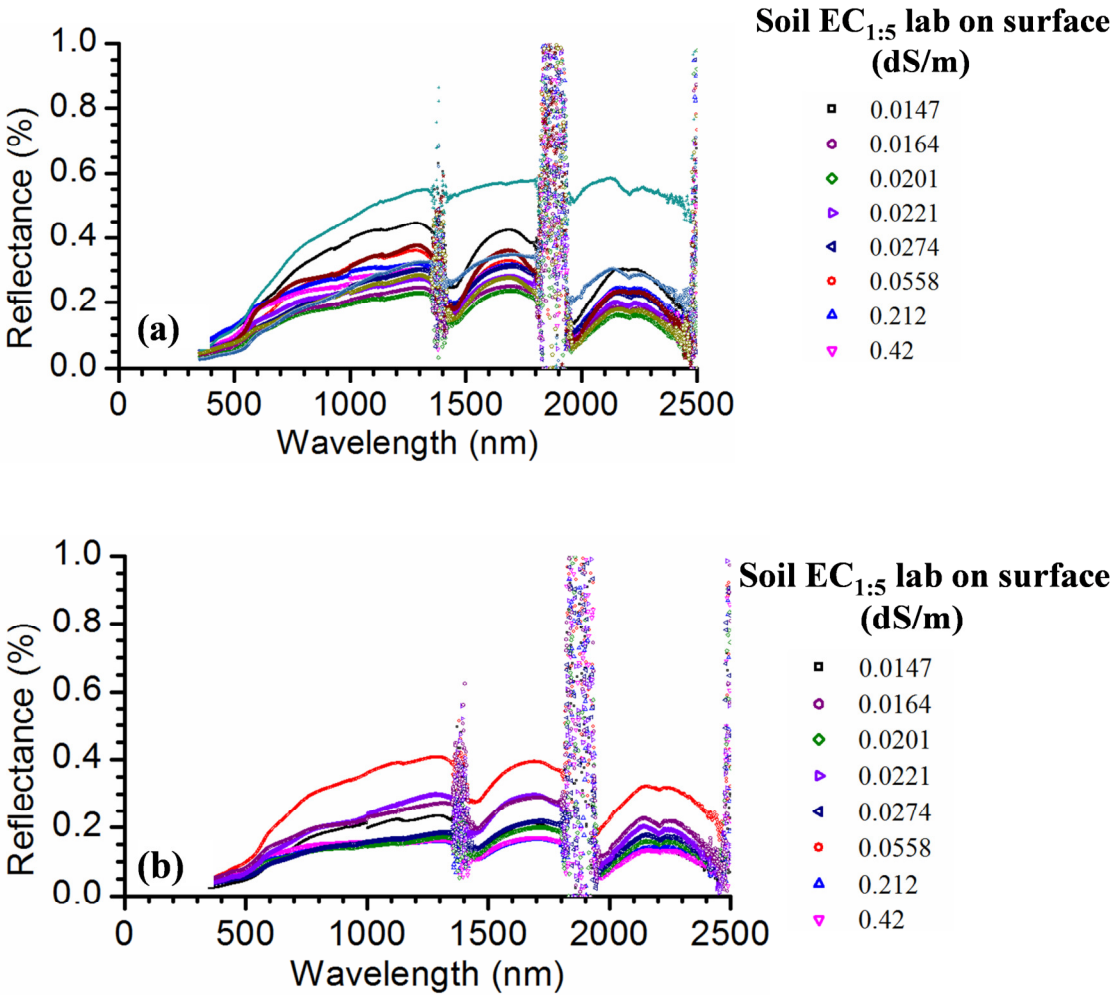

Figure 4.6 Changes in spectral reflectance with variation of $EC_{1:5}$ lab on the surface for samples taken from Khon Kaen province (a) soil reflectance on the surface, and (b) soil reflectance at 20 cm.

Taking variation of soil $EC_{1:5}$ lab on the surface as an example, the dynamic change patterns of the reflectance spectra obtained from the soil reflectance with sample layers of 5 cm and the subsurface layer at the depth of 20 cm under different levels of salinity in Khon Kaen province as shown in Figure 4.6(a) and Figure 4.6(b), respectively. The wavelength regions located in the range of 1350–1440, 1800–1960, and 2380–2500 nm severely harmed by the atmospheric absorption during the field measurement process. Therefore, these wavelength regions were excluded from entire analyzes. In addition, the spectral data from 350 to 390 nm were not included because of spectral inconsistencies.

4.2.3. Rice and LAI measurements

Rice plant studies were examined by gathering data such as crop length as presented in Figure 4.7(a), panicle length, LAI, canopy openness, and digital photos of plant condition of each quadrat. Rice plant location was selected randomly from each corner of the quadrat as well as its middle. The average values of crop length, panicle length, canopy openness, and LAI were used for data analyzes. These measurements were investigated to confirm the effect of salinity on the rice growth. Rice panicle length, defined as the length of the panicle neck to the apex (Huang et al. 2013), was measured at the maturity stage. The LAI was calculated as the summation of the areas of entire leaves divided by the ground area above which the leaves have been gathered (Yoshida 1981). The canopy openness defined as the relevant percentage of sky that is visible from a position beneath the canopy (Voss 1988), were calculated as a percent of open sky derived from diffuse non-interceptance (DIFN). LAI and canopy openness were determined in this study by using LAI-2000 plant canopy analyzer as shown in Figure 4.7 (b). The LAI is considered as an indicator of the density of plant canopies and is relatively easy to measure. The relevant statistical parameters for soil EC in the paddy field are summarized in

Table 4.1. The mean value of LAI is 2.82 for jasmine rice and 1.67 for glutinous rice.

Figure 4.7 Field investigation: (a) crop length measurement and (b) LAI measurement.

Table 4.1 Descriptive statistics of LAI in the paddy fields

Description	Jasmine rice					Glutinous rice				
	Mean	Max	Min	SD	CV	Mean	Max	Min	SD	CV
	-	-	-	-	-	-	-	-	-	-
LAI	2.82	4.43	0.85	1.06	0.38	1.67	3.23	1.07	0.58	0.34

Notes: Max: maximum; Min: minimum; SD: standard deviation; CV: coefficient of variation

4.3. Data analysis

4.3.1. Determination of $NDSI_{i,j}$

The pre-process before determination of $NDSI_{i,j}$ is carried out by averaging the spectral data from every spectral reflectance measurement for each quadrat. $NDSIs_{i,j}$ is a method to extract the new spectral index from the full spectral band (Inoue et al. 2008), calculated by the formulation similar to NDVI. The NDSI expression for i and j bands is defined as:

$$NDSI_{i,j} = \frac{(R_i - R_j)}{(R_i + R_j)} \tag{4.1}$$

Where R_i is the reflectance corresponding to the wavelength i and R_j is the reflectance corresponding to the wavelength j.

Mathematically, $NDSI_{i,j} = - NDSI_{j,i}$ and the value of $NDSI_{i,j}$ as shown in Equation (4.1) ranges from -1 to 1. NDSI [i,j] was assigned as the spectral index, while soil EC was used as the salinity indicator, which varies with the location of the rice field. The hyperspectral data analysis was conducted using the VIS, NIR, and SWIR regions of the spectrum (350–2500 nm) subdivided into 1 nm bandwidths. Each of these was analyzed to seek a relationship between the measured data set of $NDSI_{i,j}$ and soil EC. The precise calculation of $NDSI_{i,j}$ was carried out for each integer i from 350 with j=i+3, i+4 until 2500. The resulting coefficients of determination (R^2) can help identify the best pair of wavelength (i,j) among the whole combinations of NDSIs. Then, inconsistent

wavelengths that were affected by atmospheric disturbance from the field investigation were eliminated.

4.3.2. Salinity measurements

Soil salinity refers to the accumulation of salt in the soil especially on the surface or near-surface; principally chlorides (Cl^-), sodium (Na^+), calcium (Ca^{2+}), magnesium (Mg^{2+}), sulfate (SO_4^{2-}) , and carbonates of sodium (Na_2CO_3) (Tanji 2002). The excessive of these ions content in the soil can severely affect plant growth and land use, and increase soil erosion. For this reason, understanding the chemical component contained in the soil is very important. Figure 4.8 shows the process to ions concentration in soil. However, the main ions content that are used to determine the degree of salinity is chlorides (Cl^-) and sodium (Na^+).

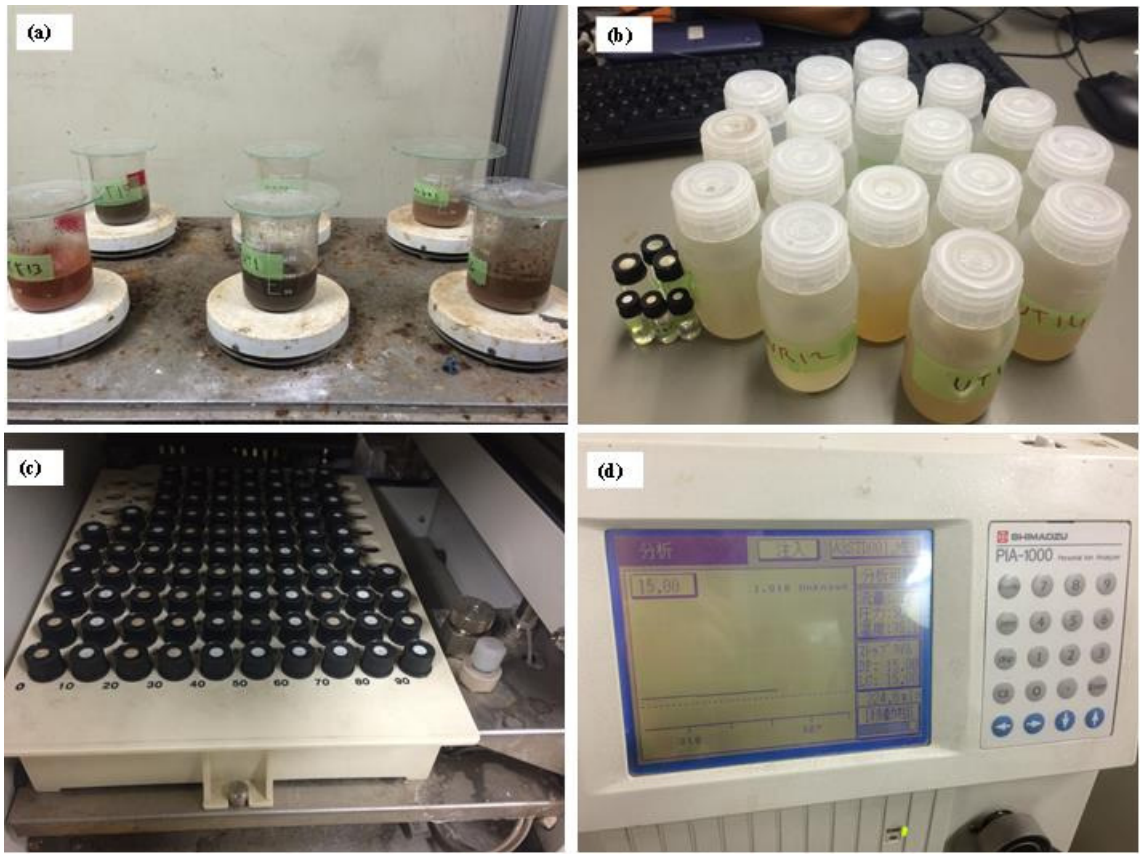

Figure 4.8 Ions measurement procedures: (a) soil sample, (b) soil/water solutions, (c) location of solution, and (d) ion apparatus.

First, soil samples were weighed about 20 g and mixed with distilled water about 100g. The solution was mixed using a magnetic stirrer F-616H for 24 hours. After stirring, the solution was extracted by filtering. Lastly, the ions content was tested using personal ion analyzer PIA-100. In addition, the same solutions that used for determination of the concentration of ions concentration were also used for determine the additional salinity parameters such as $EC_{1:5}$, TDS, pH, and salt by using multi-water checker (Model 7200, FUSO). The ions content, which is indicators of the presence of salinity in the soil, was selected as the soil properties to be investigated in relation to soil EC. The aims of this experiment confirm the relationship between the soil EC and detail component of the soil salinity.

4.4. Results

4.4.1. Relationship between electrical conductivity and soil salinity

For the purpose of the definition, saline soils have an electrical conductivity of saturation extracts of more than 4 dS/m at 25^{o}C. Soil salinity is measured as the salt concentration of the soil solution in terms of electric conductivity EC in dS/m. Sensitive plants are affected by half this salinity and highly tolerant ones at about twice this level (Richards 1954). Salinity or Total Dissolved Solids (TDS) is a measure of the total ionic concentration of dissolved minerals in water. TDS is composed of the following principal cations (or positively charged ions): Sodium (Na^{+}), Calcium (Ca^{2+}), Potassium (K^{+}), Magnesium (Mg^{+2}), and anions (or negatively charged ions): Chloride (Cl^{-}), Sulfate (SO_4^{2-}), Carbonate (CO_3^{2-}), Bicarbonate (HCO_3^{-}), and, to a lesser extent by Nitrate (NO_3^{-}), Boron (B^{3+}), Iron (Fe^{3+}), Manganese (Mn^{2+}) and Fluoride (F^{-}). TDS can be readily estimated in the field or laboratory by measuring the electrical conductivity (EC) of an aqueous solution. Figure 4.9 shows the correlation between Chloride, Sodium, and the concentration of salt, NaCl to the soil $EC_{1:5}$ lab. The high correlation was found. In addition, The correlation between TDS and $EC_{1:5}$ on the surface (Figure 4.10) have R^2 equal to 0.995. For this reason, the soil $EC_{1:5}$ can be selected as the salinity indicator.

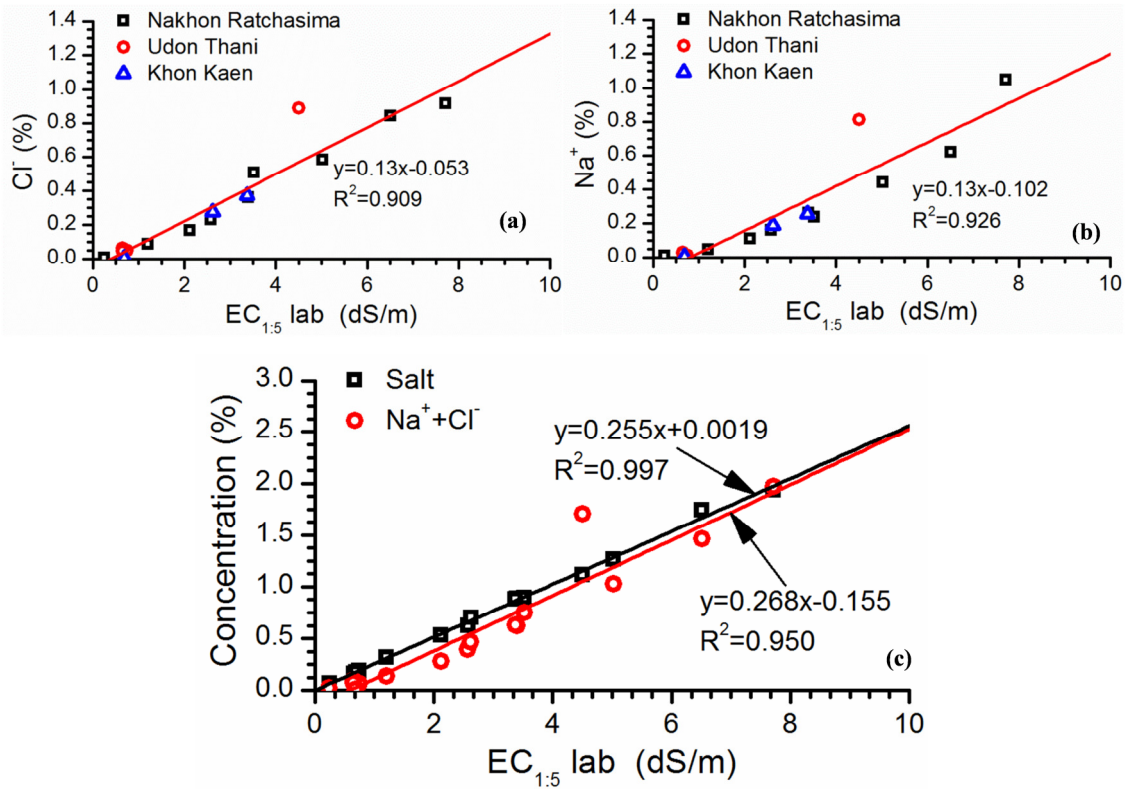

Figure 4.9 Changes of ion content in the with variation of $EC_{1:5}$ lab (a) Cl^-, (b) Na^+, and (c) concentration of salt and $Na^+ + Cl^-$.

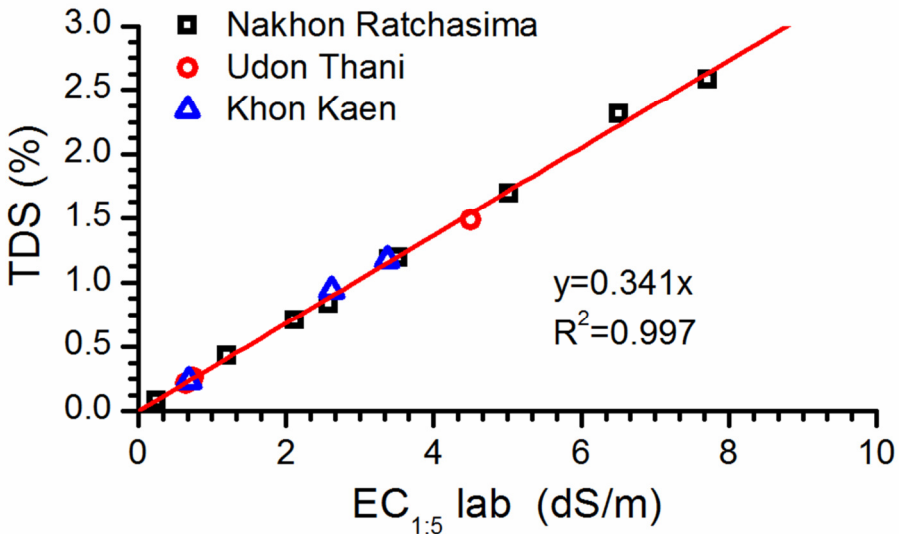

Figure 4.10 Changes of TDS with variation of $EC_{1:5}$ lab

4.4.2. Relationship of electrical conductivity and spectral reflectance index

Preliminary analysis consisted of detailed plots of R^2, which were constructed in the form of 2-D contour maps at two separate wavelengths on x and y axes ranging from

350 to 2500 nm. A separate analysis was conducted taken from composite topsoil with sample layers of 5 cm and the subsurface layer at the depth of 20 cm. The "narrow peak" indicates wavelength regions of relatively high correlation, while a deep trough indicates weak correlations. Figure 4.11 and Figure 4.12 illustrate the contour map of R^2 between NDSIs [i,j] and soil $EC_{1:5}$ lab on the surface (upper triangle) and soil $EC_{1:5}$ lab at 20 cm depth (lower triangle) for the topsoil sample layers of 5 cm and the subsurface layer at the depth of 20 cm, respectively. As a whole, large distributions of low correlation are dispensed over the entire region. Because each soil sample was mixed, turning to one homogeneous sample of each location, the detection of soil salinity was not recommended. Remote sensing technique can be used to detect the presence of salts on the surface either directly on bare lands or indirectly through the vegetation, which is affected by salinity (Metternicht and Zinck 2003). The soil samples that were used in this study were already mixed. For this reason, the estimated accuracies of relationship between soil EC and reflectance of soil taken from the mixed samples may not suitable for estimating soil EC in saline conditions.

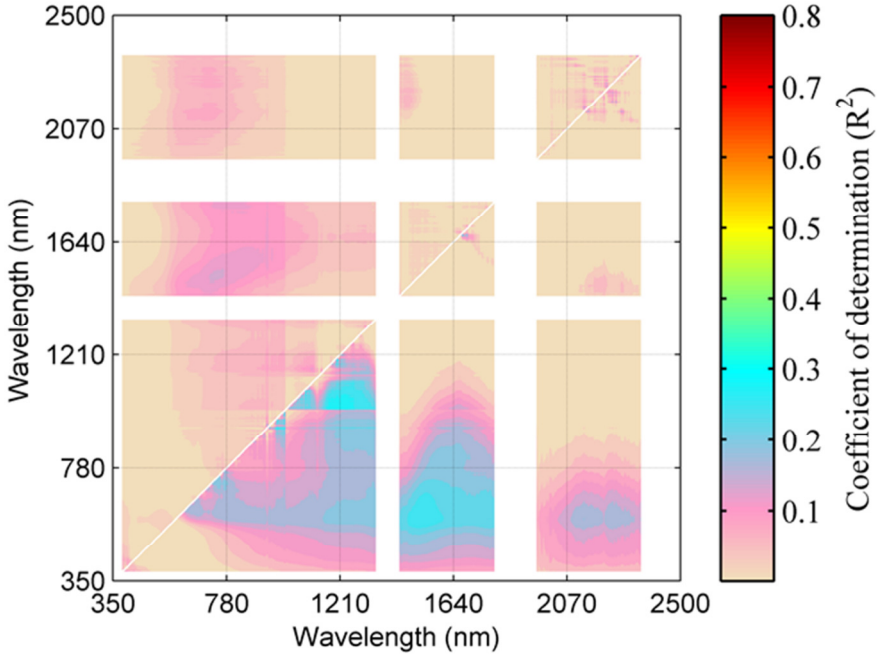

Figure 4.11 Contours of R^2 computed between NDSIs [i,j] of leaf reflectance and soil EC (upper triangle is of soil $EC_{1:5}$ lab on the surface and lower triangle is of soil $EC_{1:5}$ lab at 20 cm) for soil sample taken from the surface using the two separated wavelengths on x and y axes ranging from 350 to 2500 nm.

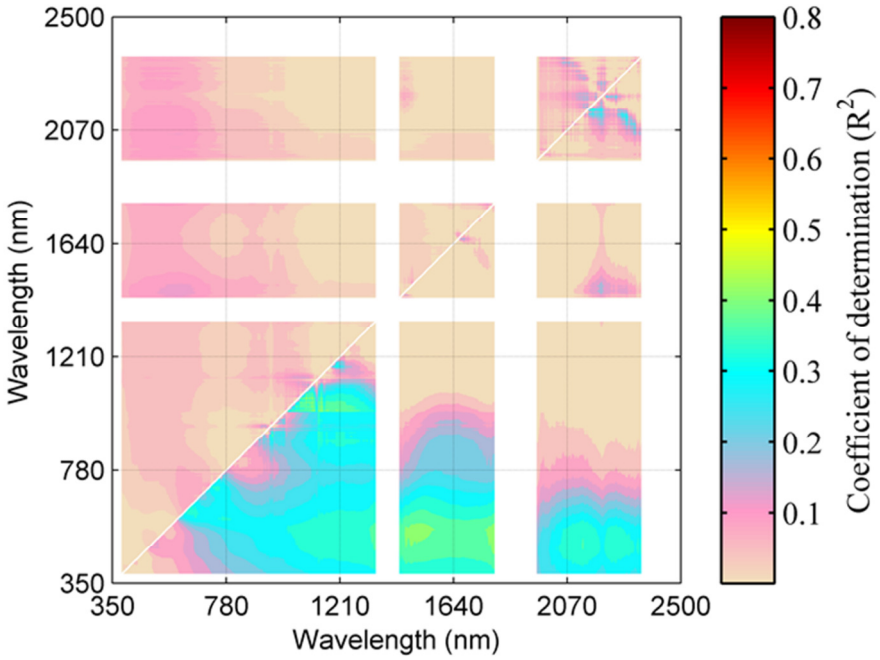

Figure 4.12 Contours of R^2 computed between NDSIs [i,j] of leaf reflectance and soil EC (upper triangle is of soil $EC_{1:5}$ lab on the surface and lower triangle is of soil $EC_{1:5}$ lab at 20 cm) for soil sample taken at 20 cm depth using the two separated wavelengths on x and y axes ranging from 350 to 2500 nm.

4.5. Conclusions

The relationship between electrical conductivity of the soil to the concentration of ions contents such as chlorides, calcium, magnesium, sulfates, and carbonates of sodium in the soil were also investigated. The good correlation of electrical conductivity of the soil to the ions was also confirmed. Therefore, the electrical conductivity could be selected as the salinity indicator. In addition, the relationships between soil EC and reflectance of soil have been determined by simple linear regression (SLR) analysis. Large distributions of low correlation, the magnitude values of the coefficient of determination (R^2) were less than 0.55, are dispensed over the entire region. Even though the weak correlation was found, this study could be used as the fundamental of the soil reflectance taken from the mixing soil sample on the surface and at 20 cm depth and soil salinity.

CHAPTER 5 ENVIRONMENTAL PROBLEMS IN OPEN PIT MINING AND GROUNDWATER MODELING FOR THE ASSESSMENT

5.1. Introduction

Open pit mine is an excavation or cut made at the surface of the ground for the purpose of extracting ore and that is open to the surface for the duration of the mine's life. To expose and mine the ore, it is necessary to excavate and relocate large quantities of waste rock. The main objective in any commercial mining operation is the exploitation of the mineral deposit at the lowest possible cost with a view of maximizing profits. The selection of physical design parameters and the scheduling of the ore and waste extraction program are complex engineering decisions of enormous economic significance. The planning of an open pit mine is, for this reason, an exercise in economics, constrained by certain geologic and mining engineering aspects (Fourie and Hohm 1992). Groundwater is becoming more important and reliable source of water supply in these days since the surface water has been polluted and insufficient to supply to the aggregate demand of industries, factories, agricultures, and urban consumption. Groundwater is a momentous operating factor in many open pit mines. Its influence is predominantly important to the stability because groundwater pressure adversely affect the shear strength of a rock mass and overburden. The design of soil and rock slopes, for this reason always includes a study of the influence of groundwater. An evaluation program will include field measurements, and interpretation, an analysis of how groundwater affects stability and an evaluation of drainage layouts to control its effects on stability.

This chapter presents the environmental problem in open pit mining and groundwater modeling for the assessment. The literature studies related to groundwater modeling, flow equation, finite element modeling, and floor heaving analysis are included in this chapter. In addition, the previous study of groundwater and stability analysis in Mae Moh open pit mining is also highlight in this chapter.

5.2. Groundwater

Groundwater can be defined as the water in the saturation zone of the earth. The hydrologic cycle of the earth consist of many processes interacting all three phases of water (Figure 5.1).Groundwater is one part of this complex hydrologic cycle. The saturated formations below the ground surface serve as a medium for transmission of groundwater and also as a reservoir for the storage of groundwater. The occurrence and movement of groundwater are related to the physical forces acting in the subsurface and the geological environments in which they occur. Gravity, pressure from the atmosphere and overlying water, and molecular attraction between solids and water are the External forces that are acting on water in the subsurface. In response to the difference in fluid pressure and elevation, groundwater move through the interconnected voids, within the saturated zone of the earth. The driving force of this phenomenon is measured in terms of potentiometric head (or hydraulic head).

(4.2)

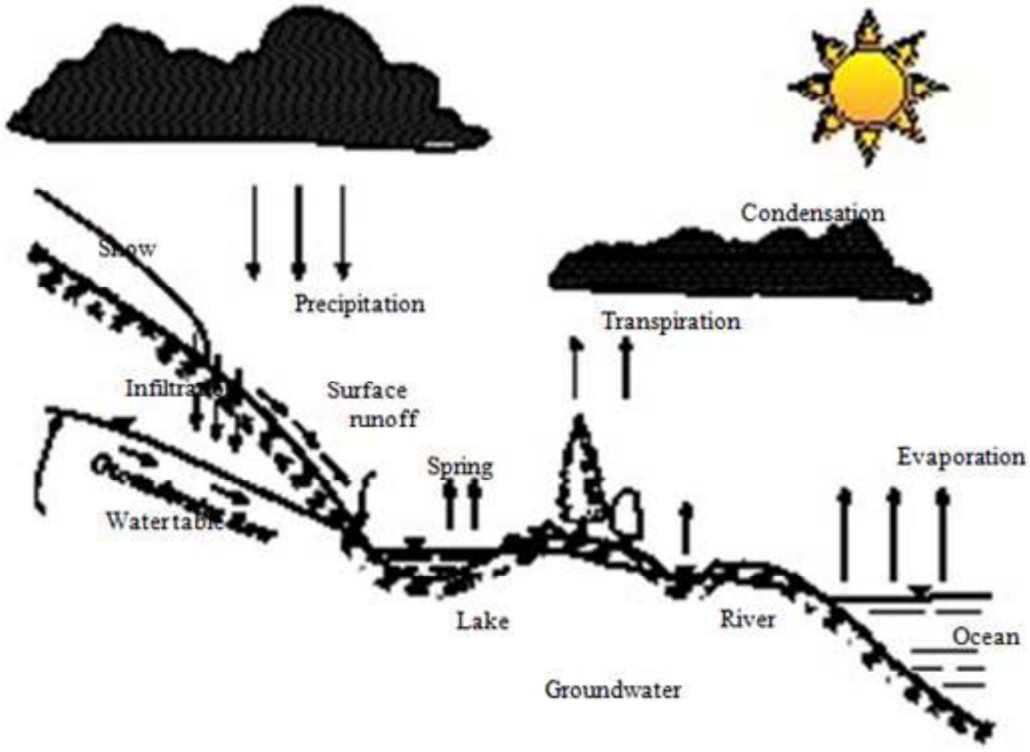

Figure 5.1 Hydrological cycle

$$h = z + \frac{p}{\rho g} + \frac{v^2}{2g} \quad (Bernoulli's\ equation) \tag{5.1}$$

Where,

h = hydraulic head [L]

z = elevation above datum [L]

p = fluid pressure with constant density D [L]

g = acceleration due to gravity [LT^{-2}]

v = fluid velocity [LT^{-1}]

Pressure head (h_p) is defined as:

$$h_p = \frac{p}{\rho g} \tag{5.2}$$

Water is held in tension in the unsaturated zone, and hence pressure head is less than atmospheric pressure ($h_p < 0$). In the saturated zone, pressure head is greater than atmospheric pressure ($h_p > 0$). The velocity component of hydraulic head is neglected because groundwater velocity is usually very low. For this reason, hydraulic head can be expressed as:

$$h = z + h_p \tag{5.3}$$

5.2.1. Water table and potentiometric surface

The height of water rise in a well is the summation of elevation head and pressure head (Figure 5.2). The pressure head is equal to the height of the water column above the point which may concern within the well. The water table is defined as the surface of a groundwater body at which the pressure is atmospheric, and is measured by the level at which water stands in wells that penetrate the water body just far enough to hold standing water. The potentiometric surface approximates the level to which water will rise in a tightly cased well that can be screened at the water table or greater depth. In wells that penetrate to greater depths within the aquifer, the potentiometric surface may be above or below the water table depending on whether an upward or downward component of flow exists. The potentiometric surface can vary with the depth of a well. In confined aquifers, the potentiometric surface will rise above the aquifer surface. The

water table is the potentiometric surface for an unconfined aquifer where the head varies appreciably with depth in an aquifer; a potentiometric surface is meaningful only if it describes the static head along a particularly specified stratum in that aquifer. The concept of the potentiometric surface is only rigorously valid for defining horizontal flow directions from horizontal aquifers.

5.2.2. Aquifer formations

In general, an aquifer is a geologic unit that contains enough accessible water. Depending on the geological aspects, Aquifers can be classified into four basic formation types in which they occur, namely: unconfined, confined, semi-confined, and perched (Figure 5.3). Unconfined aquifers sometime called phreatic or water table aquifers because their upper boundary lies in the water table. The level of this boundary fluctuates with the effects of recharge and discharge Unconfined aquifers are generally close to the land surface, with continuous layers of materials of high intrinsic permeability extending from the land surface to the base of the aquifer.

- Confined, or artesian, aquifers are created when groundwater is trapped between two layers of low permeability known as aquitards. In a confined aquifer, the groundwater is under pressure and the water level in a well rises above the upper boundary of the aquifer. Flowing artesian conditions exist when the water level in a well rises above land surface. Recharge to confined aquifers is predominantly from areas where the confining bed is breached, either by erosional unconformity, fracturing or depositional absence.

- Semi-confined, or leaky, aquifers occur when water-bearing strata are confined, either above or below, by a semi-permeable layer. When water is pumped from a leaky aquifer, water moves both horizontally within the aquifer and vertically through the semi-permeable layer.

- A perched aquifer is a special type of the unconfined aquifer where a groundwater body is separated from the water table by a layer of unsaturated material. A perched aquifer occurs when an impermeable formation intercepts water moving down through

the unsaturated zone. Clay lenses in sedimentary deposits often have shallow perched water bodies overlying them. Wells tapping perched aquifers yield temporary or small quantities of water.

5.2.3. Fundamental of Flow in Aquifers

Hydraulic head; drawdown; porosity; discharge; velocity and ground water velocity; hydraulic conductivity, permeability, and transmissivity; and capillarity and capillary fringe are the key hydraulic and hydrogeological quantities to characterize aquifers. These quantities are used for almost every aquifer problem. In the following sections, based on (Batu, 2006), definitions, as well as some key aspects of these quantities, are presented.

5.2.3.1.Darcy's Law

Soil and rocks are classified with respect ground water flow on the basis of their permeability. Permeability or hydraulic conductivity is the rate at which water will flow through a material under a given pressure differential. For homogeneous material, it is express via Darcy's law (Figure 5.4).

$$Q = -kA\frac{dh}{dl} \tag{5.4}$$

Where,

Q = flow rate [L^3T^{-1}]

k = coefficient of permeability [LT^{-1}]

A = cross section area through which flow takes place [L^2]

$\frac{dh}{dl}$ = hydraulic gradient

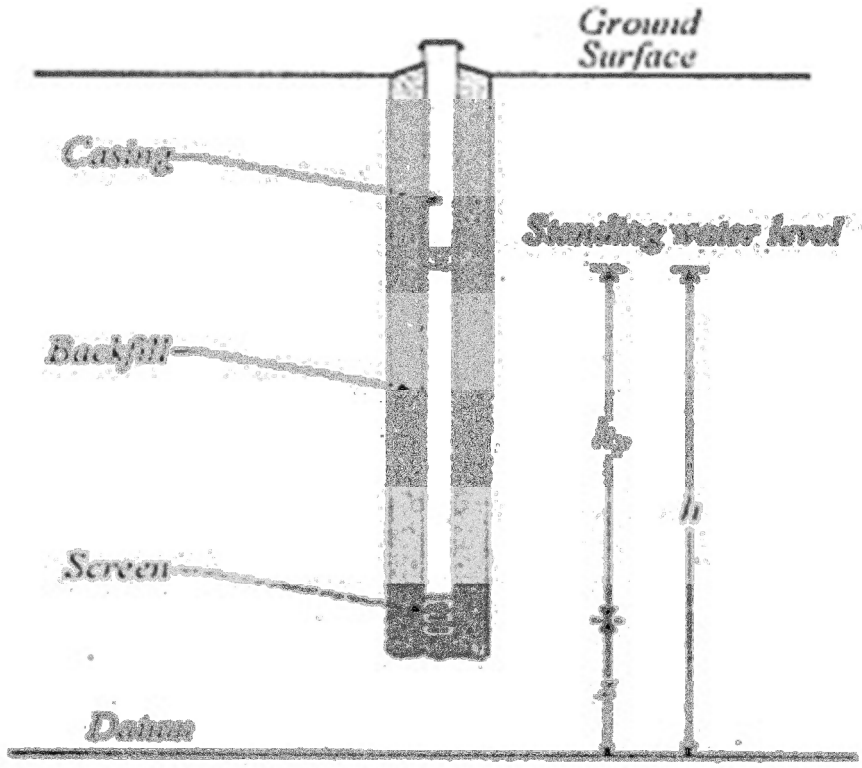

Figure 5.2 Relationship between hydraulic head, pressure head, and elevation head within a well

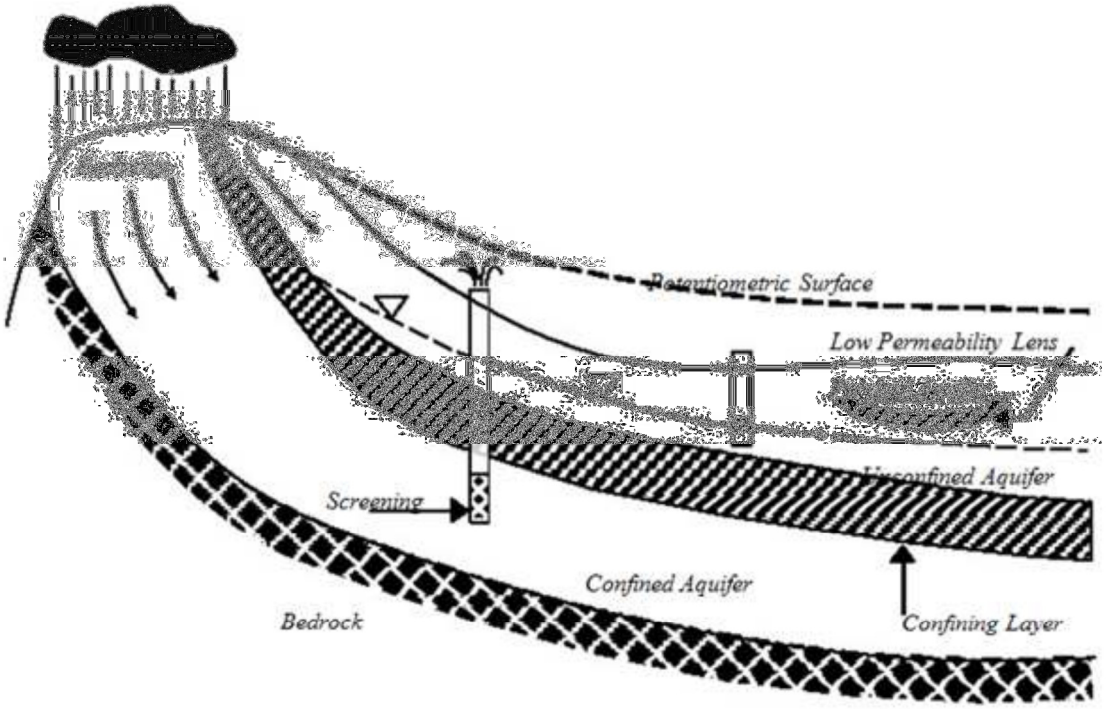

Figure 5.3 Aquifer formations

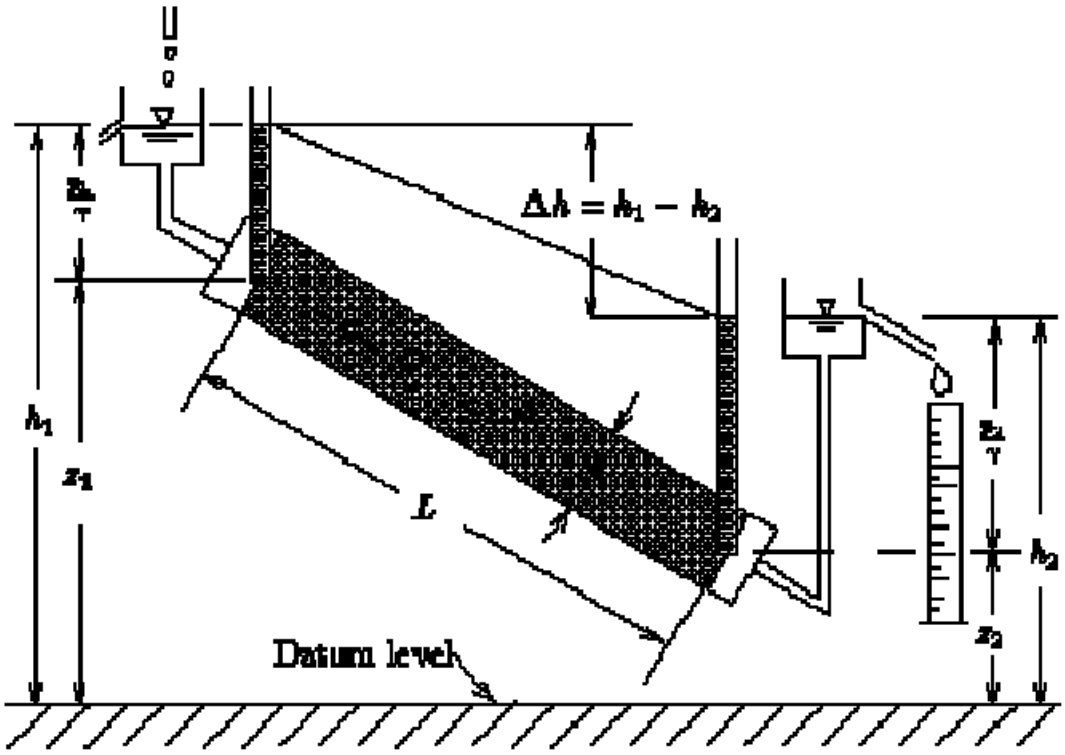

Figure 5.4 Simplified permeability test

5.2.3.2. Hydraulic Head and Drawdown

Hydraulic Head

Hydraulic head, which is also called as head or piezometric head, is defined as the fluid pressure of water formation produced by the height above a given point.

Drawdown

Under extraction or injection conditions from a well, the position of the initial hydraulic head at a point in an aquifer changes, and the vertical distance between the initial hydraulic head at a point in the lower position of hydraulic head at the same point is called drawdown.

5.2.3.3. Porosity and Specific yield

Porosity is defined as the ratio of void space to the total volume of media. Primary porosity in the material is due to the properties of the soil or rock matrix while secondary porosity is developed in the material after its emplacement through such processes as solution and fracturing. Figure 2.6 shows different types of pore spaces in

sediments and rocks.

$$n = \frac{V_v}{V_t} \tag{5.5}$$

Where,

V_v = volume of void space [L^3]

V_t = total volume (volume of solids plus volume of voids) [L^3]

The effective porosity is the porosity available for fluid flow. The effective porosity of a unit of media is equal to the ratio of the volume of interconnected pores that are large enough to contain water molecules to the total volume of the rock or soil. Specific yield (Sy) is the ratio of the water that will drain from a saturated rock owing to the force of gravity to the total volume of the media. Specific retention (Sr) is defined as the ratio of the volume of water that a unit of media can retain against the attraction of gravity to the total volume of the media. The porosity of a rock is equal to the sum of the specific yield and specific retention of the media. For most practical applications in sands and gravels, the value of effective porosity can be considered equivalent to specific yield.

5.2.3.4. General three-dimension Equation

Based on Waterloo Hydrogeologic Inc (1999), the three-dimensional movement of groundwater of constant density through porous earth material may be described by the partial differential equation:

$$\frac{\partial}{\partial_x}(K_{xx}\frac{\partial_h}{\partial_x}) + \frac{\partial}{\partial_y}(K_{yy}\frac{\partial_h}{\partial_y}) + \frac{\partial}{\partial_z}(K_{zz}\frac{\partial_h}{\partial_z}) = S_s\frac{\partial_h}{\partial_t} - W \tag{5.6}$$

Where

k_{xx} , k_{yy} , k_{zz} : Values of hydraulic conductivity along the x, y, and z coordinate axis, which area assumed to be parallel to the major axes of hydraulic conductivity (Ll^{-1})

h : Potentiometric head (L))

W : A volumetric flux per unit volume and represents sources and/or sinks

of water (T^{-1})

S_S : The specific storage of porous material (L^{-1}); and t is time (t)

In general, SS, k_{xx} , k_{yy} , and k_{zz} may be function of space (SS = $S_S(x,y,z)$, K_{xx} = $k_{xx}(x,y,z)$, etc.) and W may be a function of space and time (W = W(x,y,z,t); equation (5.6) described groundwater flow under non-equilibrium conditions in a heterogenous and anisotopic medium, provided the principal axes of hydraulic conductivity area aligned with the coordinate direction.

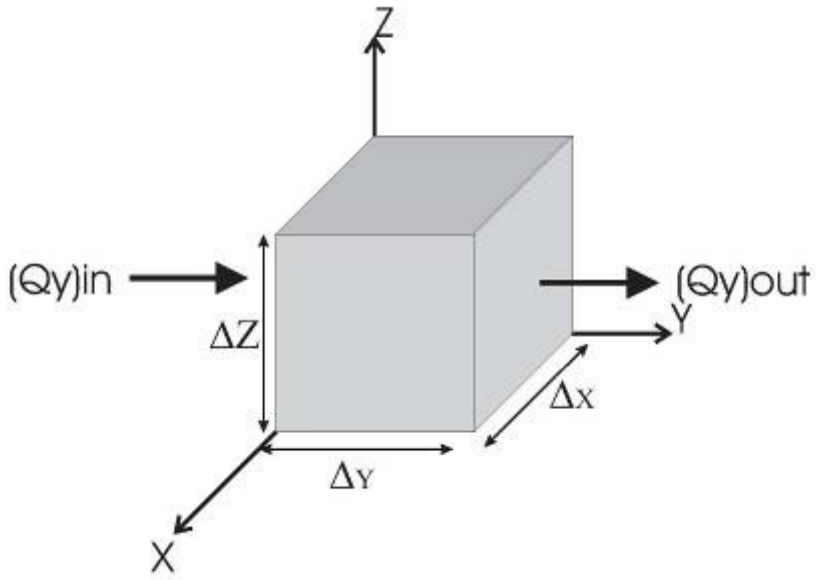

Figure 5.5 Representation Elementary Volume (REV)

5.2.3.5. Transmissivity (T) and storage coefficient (S)

The concept of transmissivity and storage coefficient were developed primarily for the analysis of good hydraulics in confined aquifer (Freeze and Cherry 1979) The transmissivity related to the hydraulic conductivity and saturated thickness.

$$T = K \times b \qquad (5.7)$$

Where

K = hydraulic conductivity [LT-1]

b = saturated thickness of the aquifer [L]

It is defined as the rate at which water of prevailing kinematic viscosity is transmitted through a vertical strip of the aquifer of unit width an extending through the full saturated thickness, b, under a unit hydraulic gradient.

The storage coefficient also known as the coefficients of storage is defined as the volume of water that an aquifer releases from or takes into storage per unit surface area of aquifer per unit change in the component of the head normal to the surface.(Fig. 2.8)

For a confined aquifer,

$$S = b \times S_S \tag{5.8}$$

Where

b = thickness of the aquifer [L]

S_S =specific storage (1/L)

Specific storage is the amount of water per unit volume of a saturated formation that is stored or expelled from storage owing to compression and expansion of the mineral skeleton and the pore water per unit change in hydraulic head. The specific storage (1/L) is given by:

$$S_S = \rho_w g(\alpha + n\beta) \tag{5.9}$$

Where

ρ_w = density of water [$ML^{-3}T^{-2}$]

g = acceleration of gravity [LT^{-2}]

α= compressibility of the aquifer skeleton [$1/(ML^{-1}T^{-2}$]

n = porosity

β= compressibility of water [$1/(ML^{-1}T^{-2}$]

5.2.3.6.Hydraulic Conductivity and Permeability

Hydraulic Conductivity (k)

The definition of hydraulic conductivity is derived from Darcy's Law:

$$k = \frac{q}{i} = -\frac{Q}{A(\frac{dh}{ds})} \tag{5.10}$$

It is apparent from this equation that k has dimensions of "length/time" (L/T) or velocity. This coefficient is called hydraulic conductivity or saturated hydraulic conductivity and is the function of properties of both the porous medium and the fluid flowing through it.

Permeability

The term coefficient of permeability is used instead of hydraulic conductivity, especially in the geotechnical engineering literature. This is inappropriate because k not only depends on the permeability of the porous medium but also on the properties of the fluid flowing through the porous medium. The properties that affect the flow are dynamic viscosity $\mu\mu$ and $\gamma\gamma$. The dynamic viscosity $\mu\mu$ of the fluid is a measure of the resistive force within the pores of the porous medium, and the specific weight $\gamma\gamma$ may be considered as the driving force exerted by the gravity.

5.3. Groundwater modeling

Groundwater system is very complicated in nature due to the inconsistency of physical and hydrogeological conditions and the heterogeneity of the aquifers systems. To deepen and ease the understanding of the subsurface configuration, and to characterize the hydrogeological units under investigation with limited data, it is required to make assumption and simplification of certain field parameters. In this sense, groundwater modeling is generated, with the integration of the thorough understanding of hydrogeological condition and natural condition with the available data, to deal with any groundwater-related problems. In other words, groundwater modeling is a special tool capable of representing the real condition of the aquifer system, and widely used to simulate the groundwater flow system as well as to evaluate and forecast the effect of hydrological changes in aquifer.

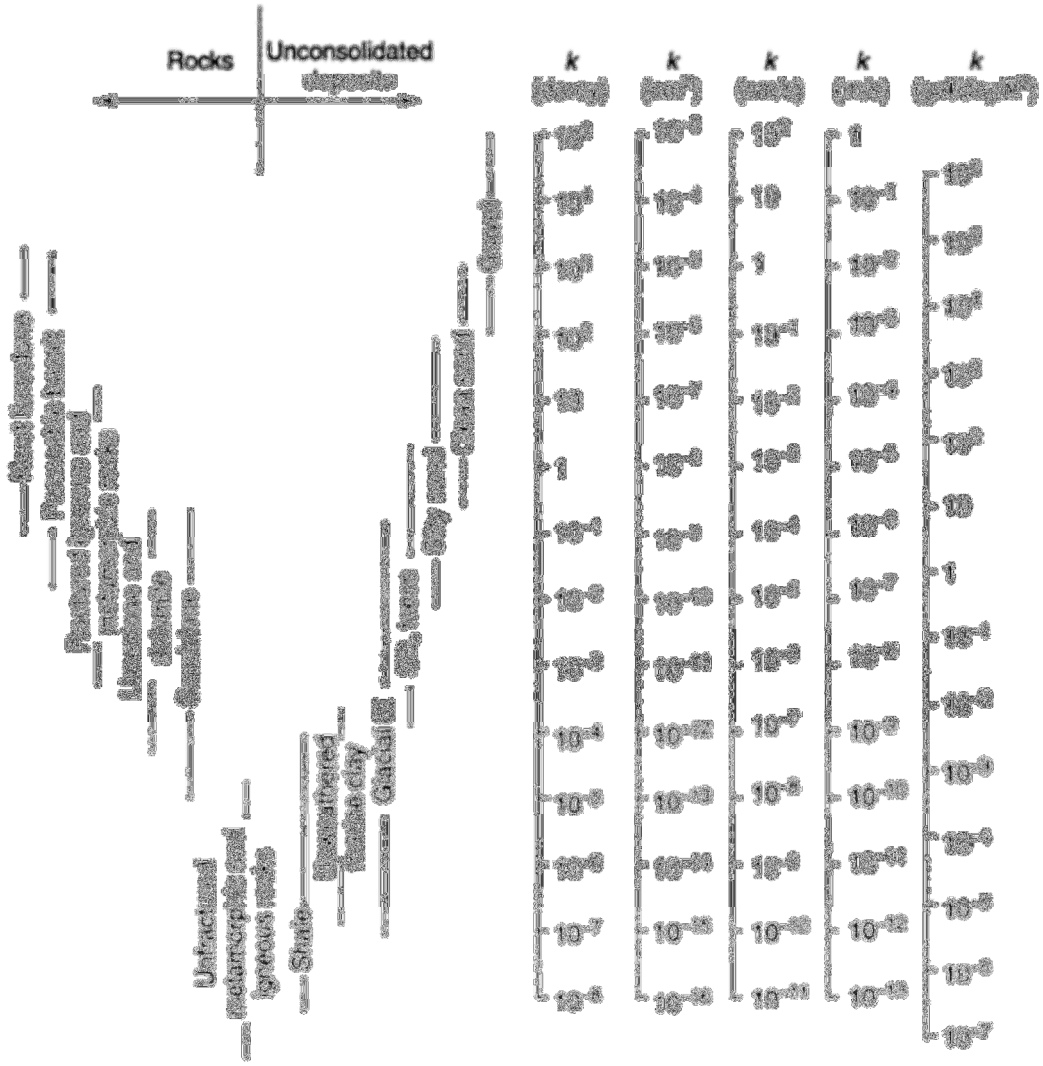

Figure 5.6 Hydraulic conductivity and permeability rang of values in a different unit

5.3.1. Type of groundwater modeling

Until this present day, numerous types of groundwater modeling have been developed to resolve a particular groundwater problem within the limited availability of data and the objectives of modeling. Generally, there are three main types of models including (1) physical scale models- scaling down the duplicate of real system; (2) analog models using other type of model with similar characteristics that could represent groundwater behaviors such as electrical model; and (3) mathematical models which rely on the basic mathematical equation of the groundwater flow. According to Spitz & Moreno (1996), the most common groundwater models that have been used to simulate groundwater

flow and transport include analytical models, porous media models, viscous fluid models or Hele- Shaw models, membrane models, electrical analog models, empirical models, mass balance models, and numerical model. All of these groundwater models are very restricted in their scope of application, except the numerical model that can deal with a complex problem of groundwater.

5.3.2. Numerical Modeling

Numerical modeling, a set of numerical methods to work out the complexity of the mathematical equation of the groundwater behaviors in the hydrogeological units, is a very new approach for the simulation of complex groundwater flow and transport. By mean of computer program in which the program codes have already been written with little or no restriction on boundary types, initial conditions and characteristics of investigated solute in the aquifer system, it is no longer a very difficult task to figure out the groundwater flow system and mass transport behaviors. The outstanding point of numerical modeling is its ability to bind together data and physical principles into a coherent and useful picture of a site (Spitz & Moreno, 1996). For these undisputable reasons, numerical modeling becomes the most commonly used form of groundwater modeling analysis and outclasses other types of models.

5.3.3. Steps in Designing Numerical Models

There are many ways to solve the partial differential equations in numerical groundwater and solute transport modeling. Though the method uses may vary according to the site-specific problem, it still exists commonly fundamental phases in numerical model design (Spitz & Moreno, 1996). It includes the following components:

- Compiling and interpreting field data. It is required to gather all the available field data and interpret it in order to get a better understanding of the natural system, to specify the main groundwater problem, to ease the selection of the program code together with required input data used in the modeling process. After the compilation and interpretation of the field data, it is possible to develop a site-specific groundwater problem with a readily decided code. The accuracy of the model result does primarily depend on the validity of the model physics and the quality of the input from field data.

- Understanding the natural system. The understanding of the natural system is crucial to ascertain the accurate modeling. The distribution of geological and hydrogeological parameters and boundary conditions must be clearly identified so that it is possible to analyze the complexity of the groundwater problem and to set the simplified configurations. It is appreciable in any cases to develop a model of investigated groundwater problem with as little effort as possible which best represents the real system. Overall, the natural system must be well understood so as to design the best-fitted model in view of needs, cost, and the availability of the data, and to develop and calibrate the model.

- Conceptualizing the natural system. After gaining the understanding of the natural system, it needs to transfer the real world condition to the conceptually equivalent model system that can be utilized to solve the groundwater problem.

At this stage, it is recommended not only to simplify the flow, but also to reduce the transport process to a few transport mechanisms considered dominant. The more the conceptual model approaches the reality, the better the result will be. The errors in the conceptual model can only be corrected during or after the model calibration by changing assumptions of certain field parameters.

- Selecting numerical model. As there is no existing model that is applicable to all types of flow and solute transport modeling, by this stage the model user must be aware of the type of computer code which can be used for the calculation of particular groundwater problem.

- Calibrating and validating the model. Since the assumptions and simplifications of the natural system are made due to the inadequacy or unavailability of field data, the model calibration are used to alter the input data within observed ranges until the simulated and the observed value are fitted together within a chosen tolerance.

In calibration phase, the model user must be able to judge if the calibrated data represent

the natural system because a good fit to historical data based on unrealistic input data is not only wrong but also misleading. Model validation, on the other hand, is needed to ensure that the model is reliable in making prediction.

A practical testing of model validation is to make a comparison of the model with a dataset not used in model calibration. If the calibrated groundwater model does not reproduce accurate results in model validation, model data are recalibrated using both datasets. The more convincing the model calibration, the more useful will be the model validation. The calibration and validation will fail or yield inadequate results if significant features of the natural system are excluded from the model.

- Applying the model. Numerical modeling demonstrates its dominance over other types of the groundwater models, for it is possible to assess the alternative scenarios for a chosen area efficiently. However, it still exits limits of model applications such as the uncertainty of the far future prediction of the groundwater behaviors.

- Presenting the results. It is required that the model output be informatively and comprehensively presented along with some illustrations; especially, it must be legible to the non-model users.

5.3.4. Data Requirement for Numerical Modeling

Since the accuracy of the model result depends on the validity and the availability of data, the main step of groundwater modeling is to collect all the existing important input data such as surface and subsurface geology, hydrogeology (water table, precipitation, pumping wells and so on), aquifer properties and water quality. According to Boonstra & de Ridder (1981) and Spitz & Moreno (1996), there are two main categories of data which are required to develop numerical groundwater flow and solute transport modeling. It encompasses data that characterize the physical framework of the groundwater basin, as well as the hydrogeological stress. Table 2.1 summarizes the required input data for numerical groundwater and transport modeling.

5.4. Boundary Condition

5.4.1. Flow boundaries

To obtain the solution of differential flow equation and the contaminant transport to a given problem, it is necessary to define additional information about the physical state of the process that does not appear in the equation because the governing equation alone is not sufficient to describe a specific physical system. In general, that additional information is derived from the detailed investigation of the study area by finding the relevant initial and boundary conditions.

Boundary conditions specify the derivative value of the dependent variable along the boundaries being modeled while initial conditions are simply the values of the dependent variable specified everywhere on the boundary of study area. In term of the groundwater model, boundaries of the model determine the locations and quantities of simulated flow in and out of the model (Huyen, 2007). The criteria for selecting boundary conditions are primarily based on the topography, hydrology, and geology. Hydrogeological boundaries conditions of the groundwater modeling are mathematically classified into three types including (1) boundary of prescribed pressure or hydraulic head, (2) boundary of prescribed flux of groundwater, and (3) semi-permeable or head-dependent flux boundary.

- Prescribed hydraulic head boundaries as shown in Figure 5.7. This first kind boundary is mathematically termed as Dirichlet's boundary condition. Prescribed head boundaries can be found in surface water bodies such as rivers, lakes, canals, sea coast, impoundments, and drain that freely interact with the aquifer. It is assumed that the elevation of surface water is equal to the elevation of the water table. The measured groundwater heads are also considered as the prescribed head boundaries (unnatural boundaries) as long as these boundaries stay unaffected by stress within and outside of the model domain during the simulation. It is recommended to use the measured heads as prescribed head boundaries when the investigated aquifer is to such a wide extent that the natural prescribed head boundaries are too remote for modeling for the reasons that they facilitate the convergence of the numerical solution of flow. In the modeling of

steady-state groundwater flow, based on Spitz & Moreno (1996), the potentiometric surface must be assigned at least one point in the model area; otherwise, an infinite number of head distributions will be found which all differ from each other at each point in the solution domain by a constant value. The specified head boundary expressed by numerical equation is:

$$H(x, y, z) = H_o \tag{5.11}$$

Where H(x,y,z) = head at a point with coordinates (x,y,z),

H_0 = specified head value.

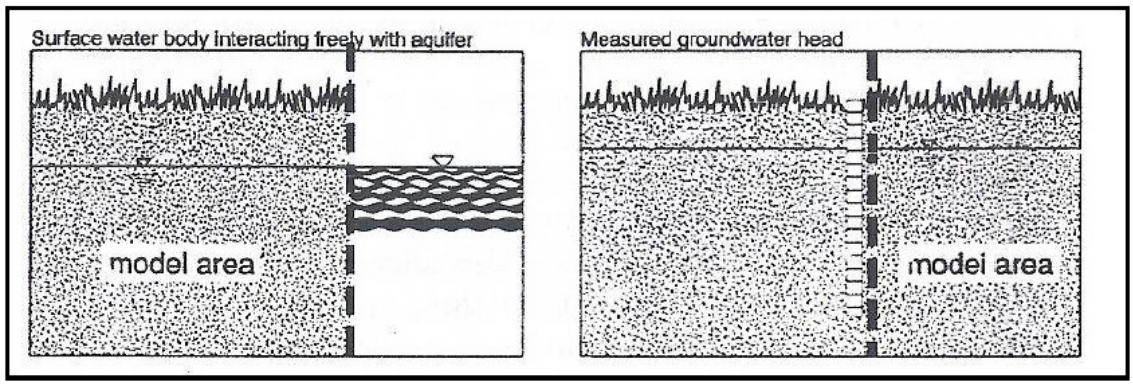

Figure 5.7 First kind of boundary condition (Spitz & Moreno, 1996)

- Prescribed flux boundaries. This second kind boundary condition, also named as Neumann's condition or recharge boundaries, is a boundary through which certain volume of groundwater enters the aquifer from adjacent strata whose hydraulic head is unknown. This type of boundary is used to describe fluxes to surface water bodies, spring flow, and seepage to and from the bedrock underlying the system. No flux boundary is a special type of prescribed flux boundary which is also referred to as a zero flux, impermeable, reflective or barrier boundary. In the analysis of the model result, no-flux boundaries are identical to streamlines. As suggested by Boonstra & de Ridder (1981), when modeling groundwater basin, it is very important to let the external boundaries of the model coincide with prescribed heads and/or no-flux boundary. Bedient et al., (1999) defines mathematical expression of prescribed flux as followings:

$$q_x = \frac{\partial H}{\partial x} = constant \tag{5.12}$$

- Semi-permeable flux boundaries. This third kind boundary condition is referred to as mixed, Cauchy's Fourier's condition or head-dependent boundary. This condition relates boundary heads to boundary flows (Adnan, 2008). It is used to represent leakage or exchange between the stream and adjacent aquifer in which leakage may change over time as the head in aquifer change though the head in the stream may remain fixed. The exchange of water between aquifer and stream depends on the head differences between surface water and groundwater. Such flow conditions can occur if the river bed acts as a semi-permeable membrane between the river and aquifer. The semi-permeable boundary can be expressed mathematically in the form of:

$$\frac{\partial H}{\partial x} + aH = C \tag{5.13}$$

Where *a*, C is constants

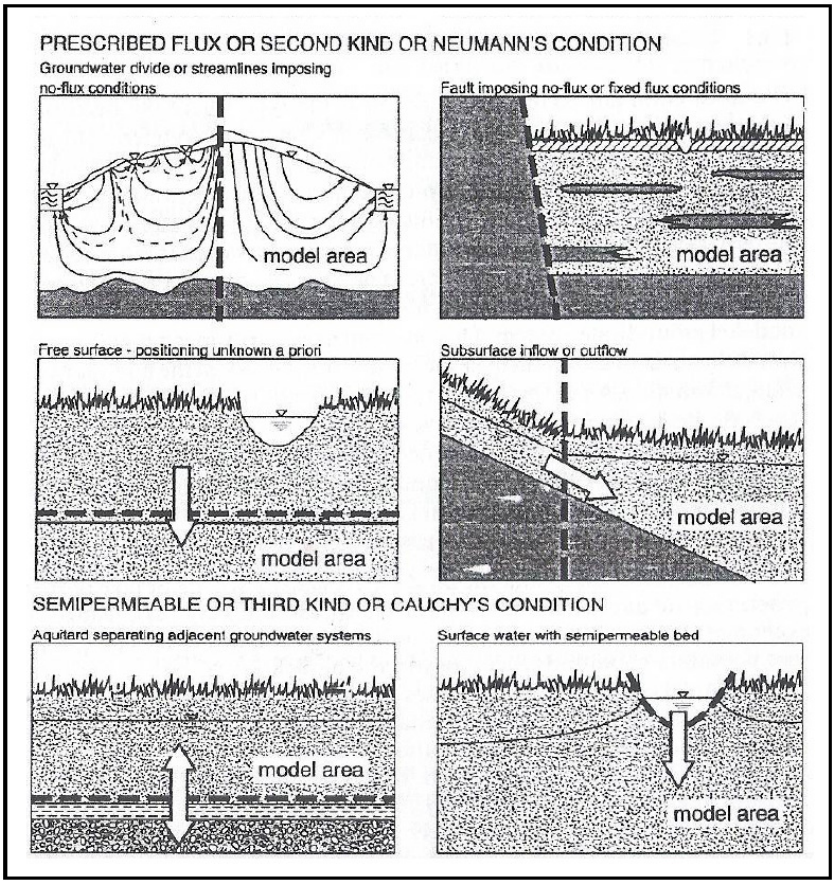

Figure 5.8 Second and third kind of boundary condition (Spitz & Moreno, 1996)

Table 5.1Typical model input data (Spitz & Moreno, 1996)

Physical Framework	
Aquifer type	Topography
	Geology
	Stratigraphy
	Aquifer geometry (Base, thickness, lateral extent)
	Lithological variation within the aquifers
Aquifer characteristics	Hydraulic conductivity/ permeability
	Heterogeneity/homogeneity, Anisotropy/isotropy
	Porosity
	Conductivity/ Pore pressure relationship
	Saturation/ Pore pressure relationship
	Specific yield
	Specific storage
	Dispersity (for transport modeling)
	Soil bulk density (for transport modeling)
Aquifer boundaries	Location
	Prescribed head
	Prescribed flux
	Semipermeable boundary (Leakage factor, head in the adjacent system)

Hydrological Boundary Conditions Initial Water Levels/Gradients	
Internal Inflow/Outflow	Recharge/discharge (Area, rate, duration)
	Extraction or injection wells (Location, rate, duration)
	Exchange with surface water (Surface water elevation, base of surface water, leakage factor)
Groundwater Quality Boundary Conditions	
Land use	Industries, agricultures
Aquifer environment	Groundwater chemistry
	Background values of solutes/contaminants
	pH
Source	Location
	Area
	Source concentration
	Volume
	Duration
Contaminant	Solubility
	Density
	Viscosity
	Henry's law constant
	Octanol-water partition coefficient
	Diffusion coefficient
	Adsorption
	Decay rate
	Biodegradability

5.4.2. Effect of deep excavation to the groundwater pressure

Groundwater flows through the earth material from the areas of greater hydraulic head to areas of lower hydraulic heads. The rate of groundwater movement depends upon the slope of the hydraulic head (hydraulic gradient), and aquifer and fluid properties. In rock masses, groundwater flow is often controlled by the secondary permeability (permeability of the structure-fold, fault, discontinuities, etc.), instead of the primary permeability (i.e., that of intact material) as in the case of soil. It is known that only relatively few cracks of remarkably small aperture are needed to increase the effective permeability of a rock mass by several order of magnitude (Morgenstern 1971).

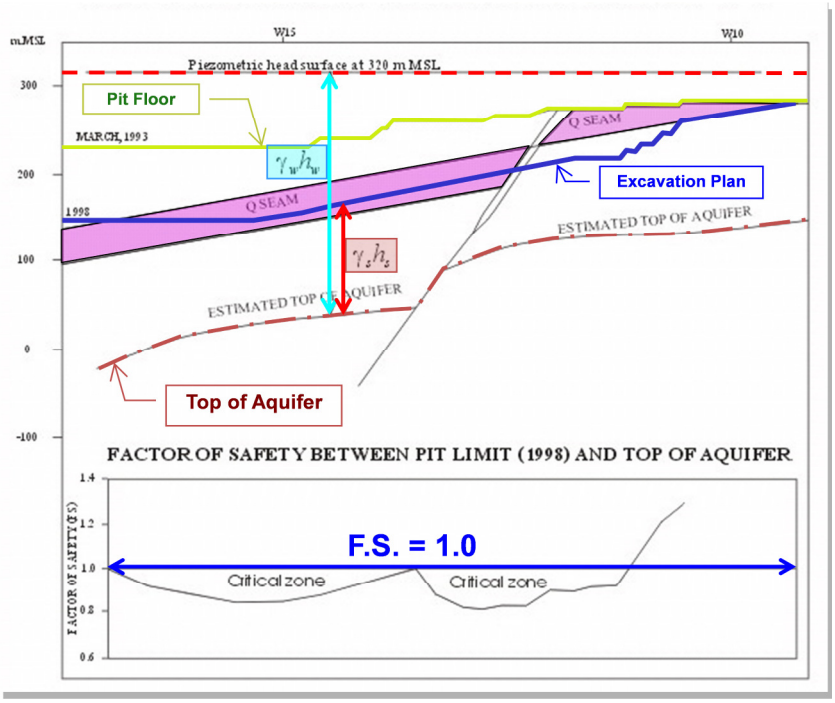

Figure 5.9 Effect of groundwater pressure on mining

The stability of the slope depends on the value of its resisting force and driving force that act on the slope. If the resisting force is greater than the driving force, then the slope is in a stable condition.

The factor of safety is calculated as shown below.

$$Factor\ of\ Safety = \frac{Resisting\ force}{Driving\ force} \tag{5.14}$$

5.5. Conclusions

The general background of groundwater modeling, groundwater problem in mining for assessment was explained. The literature review such as groundwater flow equation, type of aquifers, influence of groundwater on stability, mode of floor heaving, floor heaving evaluation was also included. The previous research associated with groundwater modeling and stability study in the Mae Moh was also highlighted in this chapter.

CHAPTER 6 GROUNDWATER MODELING OF MAE MOH OPEN PIT LIGNITE MINE, THAILAND

6.1. Introduction

The groundwater problem at Mae Moh mine has drawn attention as the mining excavation goes deeper, thus resulting in a detailed investigation of hydrogeological condition. One of the problems facing the mining is floor heave influenced by groundwater. The control of groundwater pressure in deep-seated aquifers with high elevation becomes important in the mining. In addition, the underground water at Mae Moh mine is naturally contaminated with arsenic. For this reason, the developments of 3D groundwater model of deep pit mine using Modflow simulation and the studies of underground water treatment are needed for the future planning. The predictive simulations were carried out for eight years (2007 to 2015). Because stability of the Mae Moh mine shows how can be closely linked to the water environment, this research aims to report the field visits to the water related facilities of the mine, which were conducted during 2010-2013.

The Mae Moh mine as shown in Figure 6.1, one of the largest open-pit mines in the region where deposits cover an area of more than 38 km^2, has been planned and operated by the Electricity Generating Authority of Thailand (EGAT) since 1955. Mae Moh mine supplies up to 50,000 tons of lignite to daily feed the power plants located in the mining area. The current deepest level of the pit is about 300 meters in the northeast mine area while the final depth will be 490 meters at the end of production. Due to an enormous volume of overburden excavation of about 60-80 million cubic meters per year, many engineering problems caused by the deep open-cut have been reported and handled (Pipatpongsa et al. 2009; Pipatpongsa et al. 2010; Doncommul et al. 2011).

6.2. Geology of Mae Moh basin

Typical profile of geology and hydrogeology of the Mae Moh coal is shown in Figure 6.2 and summarized in Table 6.1. Mae Moh mine is situated in the Mae Moh tertiary

basin, which has more than 1,000 m of maximum thickness. The original ground surface of the Mae Moh Basin was flat to gently rolling, consisting of easily eroded Tertiary rocks and the overlying younger sediments. The natural landforms within the basin have largely been changed by the mining activities (open pit lignite mine and heaped dumps), the infrastructure construction activities (housing resettlement areas, power plant construction), and the dam construction for water supply and storage associated with the power plants.

Figure 6.1 Map of Thailand where studied area is situated in the northern part (Source: Google map)

Table 6.1 Characteristics of hydrologic stratigraphy of the Mae Moh basin [8].

Layers	Characteristics
Quaternary deposit	This unsaturated layer of 20 m is mostly deposited in the Mae Moh basin with the water table nearly parallel to its topography. Alluvium sand and gravel partly appear.
Huai Luang formation	This semi-consolidated red-brown clay with thickness of 170 m is considered as aquitard despite the existence of minor local aquifer zone due to sand.
Na Khaem formation	This saturated layer with a thickness of about 5-300 m is considered as local minor aquifer. Some faults/joints passing the Na Khaem formation to basement formation might cause floor heave and stress release due to high underground water pressure.
Huai King formation	This semi-confining layer above the basement formation is considered as a major aquifer with thickness of about 40-230 m. The water head in the sand layer is 20 m above the ground level; therefore, dewatering is required.
Basement formation	This major aquifer has thickness of about 10-1,000 m. Limestone layer is an important aquifer.

According to the recent studies on sedimentary rocks (Silaratana et al. 2004; Songtham et al. 2005; Songtham et al. 2005; Ratanasthien et al. 2008), five main geological formations, namely, Quaternary, Huai Luang, Na Khaem, Huai King, and basement, are found in the Mae Moh basin as summarized in Table 3. Huai Luang formation is the youngest tertiary formation with thickness varying from 5 to 350 meters. It consists of red to brownish-red semi-consolidated and unconsolidated claystone, siltstone, and sandstone. Na Khaem formation is the most significant lignite-bearing formation with thickness of 250-400 meters. Five lignite seams (J, K, Q, R, and S) are also found in this formation. It is composed of lignite seams and gray to greenish-gray claystone and mudstone. The Huai King formation is a fluvial sequence consisting of semi-consolidated fine to coarse sandstone, claystone, mudstone, and conglomerate with

green, yellow, blue, and purple color with thickness varying from 15 to 150 meters. This geological formation occurs within both the Western and Eastern sub-basins, being widespread to the south, and extends beneath the basaltic lavas of the southern Mae Moh Basin (Dames and Moore 1995).

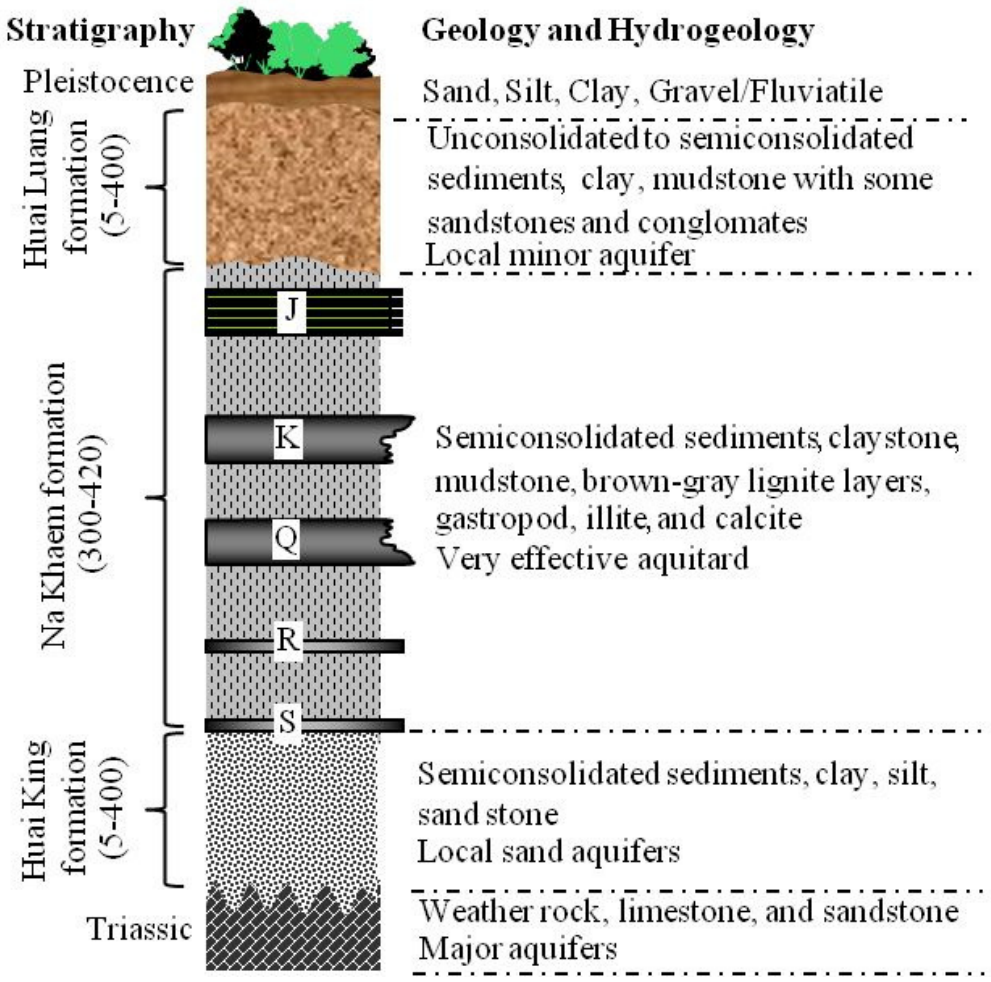

Figure 6.2 Typical profile of geology and hydrogeology of the Mae Moh coal mine (Courtesy of Electricity Generating Authority of Thailand).

6.3. Rainfall and Groundwater

6.3.1. Rainfall

There are five gauging stations installed at different locations to gather the amount of precipitation in Mae Moh mine as presented in Figure 6.3. The precipitation data at the gauging station were used to examine the hydrological condition of the open pit area.

The rain gauge, which is also known as precipitation gauge or pluviometer, can measure the amount of rainfall, and these data were transmitted to the base station through the radio telemetry system. The ID of the gauging stations shown in Figure 2 is the overview of the gauging station around study area. This representative data are calculated from the average of five gauging stations named RUM#6, RUM#3, RUM#5, RUM#7, and RUM#2. Histograms of annual rainfall data recorded from 2005 until 2012 in Mae Moh Mine are presented in Figure 6.4. The maximum amount of rain precipitated in the late rainy season of September and the minimum in the early year of February. Records of the 8-year period point out that the Mae Moh basin received the majority surface runoff with the highest rainfall of 2,155 mm in 2011, and the lowest rainfall was 825 mm in 2012. The average annual rainfall was about 1,316 mm.

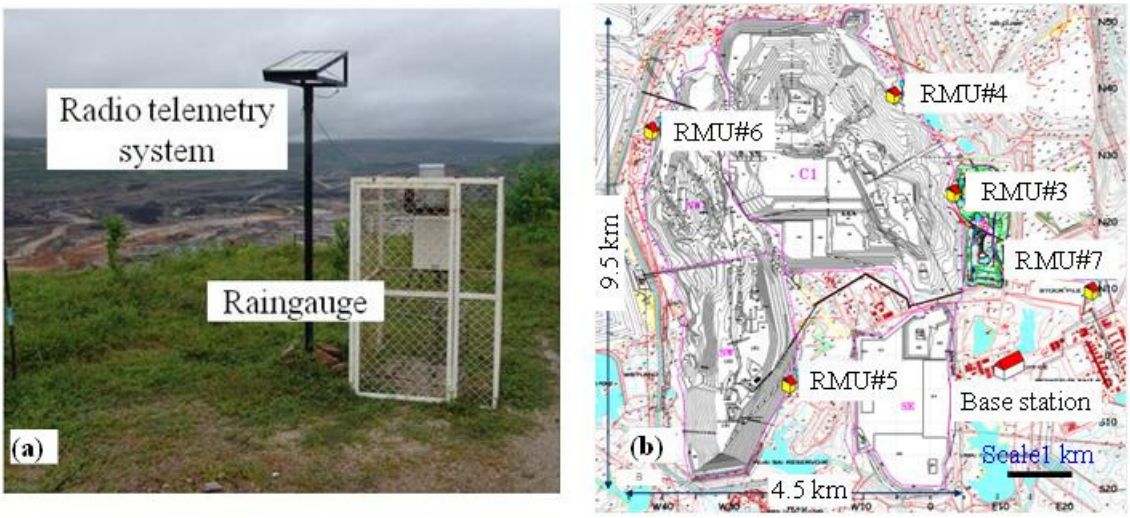

Figure 6.3 Rain gauge and radio telemetry system to receive precipitation.

6.3.2. Observation wells

Groundwater is one of the most critical factors in slope stability problem. This groundwater primarily originates from rainfalls. Some water infiltrates into the ground and percolates downwards to the phreatic zone while some flows over the surface as surface runoff. Some amount of groundwater in the saturated zone might move toward the pond. Figure 6.5 illustrates the observation wells installed at different locations in Mae Moh coal lignite mine. Numerous borehole logs associated with the groundwater drilling investigations have been recorded over Mae Moh lignite mine and in the open

pit area. The hydraulic parameter testing methods used for this study are pumping test, air lifting test, falling head test, and flow recession test. The field monitoring program for groundwater bores started from the first completed groundwater bore in the Mae Moh basin. This program continued through the drilling and testing program and is still continuing. It consists of a regular monitoring routine such as groundwater level measurements, discharge rate measurements for artesian bores, groundwater sampling, and groundwater temperature.

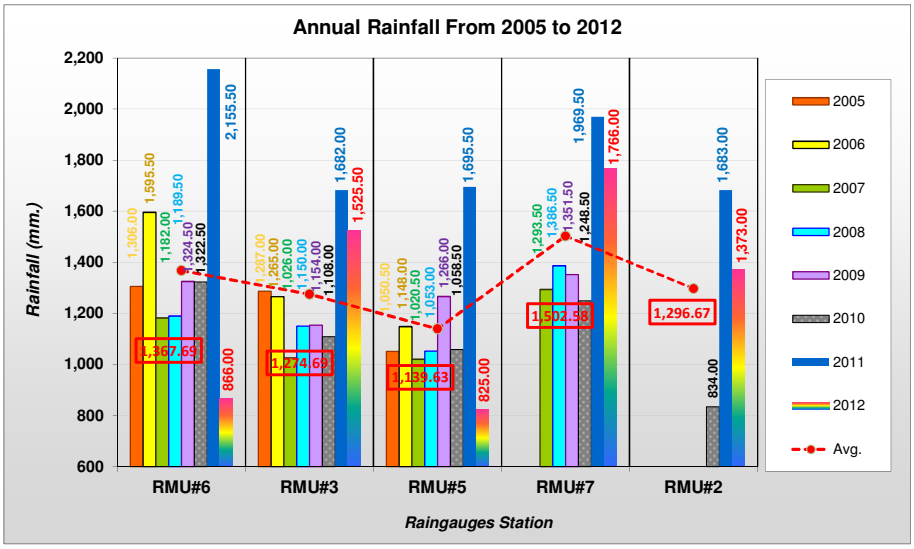

Figure 6.4 Average of annual rainfall data (Courtesy of EGAT)

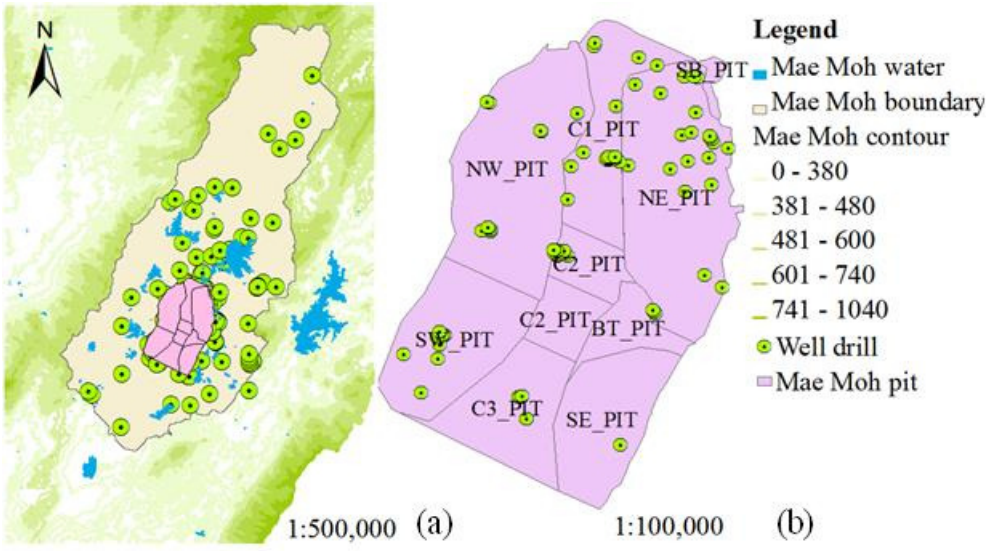

Figure 6.5 Observation wells (a) outside open pit area (b) inside open pit area (Reproduced from EGAT)

6.3.3. Groundwater

The underground water influences the magnitude and extent of strata depressurization, which have a potential impact on the Mae Moh area. Figure 7 shows a pumping well with a pipe feeding underground water to the collecting sump (20,000 m^3) as shown in Figure 8 before pumping to the holding pond (lined by plastic-sheet) of the water treatment plant. According to Pongpanlarp (2007) [8], the hydrologic stratigraphy from top to bottom of the Mae Moh basin is summarized in Table 3.

The groundwater problem at Mae Moh mine has drawn attention as the mining excavation goes deeper, thus resulting in a detailed investigation of hydrogeological condition. The Huai Luang formation contains sands that are minor local aquifer zones. The clays swell when wetting and can cause severe drilling problems in the upper portion of drill holes. The Na Khaem formation is the main confining layer for the underlying Huai King and basement formations and is thought to form an effective low-permeability confining aquitard. The Huai King formation was considered to be a major aquifer at the base of the Tertiary succession. The basement rock layer below the Huai King formation is complex, thus making it difficult to differentiate the formation. The detailed structure of the basement formations has not been not well understood. The rocks are extensively folded and faulted, and there are not enough data to fully define the structure and detailed lithology under the central basin area. Aquifers are only present in the basement formations because of secondary structures, fault after Triassic formation and cavity in limestone formation (Evans and Jitapunluk 1989). The Basement formation was group of Triassic rock compose of Tr1 - Tr5. The main aquifer was limestone layer (Tr4) in karst topography and argillite and sandstone layers (Tr3) in which the water seeps in the fractures and weather zone.

6.4. Groundwater flow modeling for center pit (C1)

6.4.1. Conceptual model

This research essentially concentrates on the modeling of groundwater pressure effect against floor heaving in the center pit (C1) as shown in Figure 6.6. The input data from the groundwater model were required to be reviewed and identified from the site investigating. Based on 40-year old power plan of Mae Moh mine, the critical area in

the year 2007 was situated in N30-N50, W35-W0 in mine grid. For this reason, the modeling was focus on this critical area. The conceptual model was designed as a fundamental graphical illustration of multiple layers of the natural aquifer system within the model boundary. The components of the conceptual model involved with the determination of model boundary and properties of the aquifer system. The conceptual model is considered as the overall purpose of the groundwater modeling. A 3D geological stratigraphy of the groundwater model is presented in Figure 6.7. In order to simplify the model, quaternary, Huai Luang, and Na Kham formation were grouped as one layer and followed by the Huai King Formation. The basement was divided into three layers. The model comprises of three aquifers and one aquitard as illustrated in Table 6.2. Because the material and hydraulic properties of Quaternary, Huai Luang, and Na Kham are quite similar; therefore these formations were grouped together for the sake of simplification of groundwater modeling.

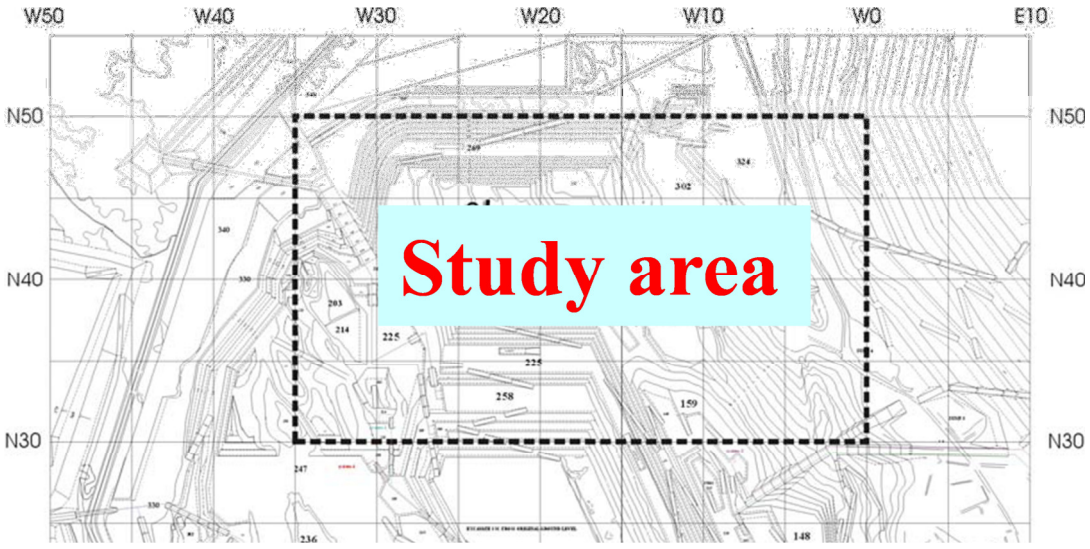

Figure 6.6 Location of Center pit (C1)

6.4.2. Model domain and grid design

The groundwater modeling of the C1 pit was established using the Modflow package (GMS 9.1, Aquaveo). The model boundary was defined as 3.5 km × 2 km, which were split into 9 material types and grid cell of 100 rows, 190 columns, and 15 layers. The model configuration was formed based on the conceptual model, which was principally reviewed from the past investigations (Dames and Moore 1995; Pongpanlarp 2007).

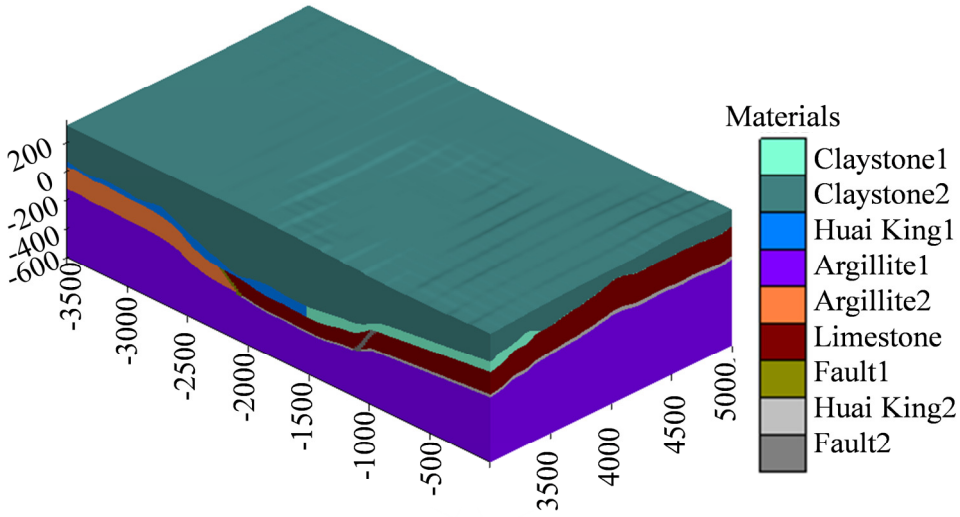

Figure 6.7 3D geological stratigraphy of the groundwater model.

Table 6.2 Geological units in conceptual groundwater model.

Formation		**Hydrostratigraphy**
Quaternary Huai Luang Na Kham	UB Claystone	Aquitard
Huai King	Semi-consolidated	Aquifer
Basement	Limestone	Aquifer
	Sandstone Argillite	Aquifer

6.4.3. Material properties

Many field investigations especially pumping tests were conducted in Mae Moh mine by EGAT. For this reason, the initial hydraulic properties of groundwater modeling were based on their results of field investigations. These parameters were modified accordingly within an acceptable range for model calibrations. In order to define the hydraulic properties of the Huai King and basement formation, numerous field tests were investigated during Phase 2 groundwater studies program of Mae Moh mine. An additional underground field investigation was also conducted from 1994 to 1996. The

hydraulic conductivity and specific storage values after the model calibration were assigned as shown in Table 6.3. The hydraulic conductivity and the storage properties were adjusted during the steady state calibration and transient state calibration. The parameters adjusted for all nodes. First, the aquifer properties were correlated with the standard aquifer properties of each rock according to Freeze and Cherry (Freeze and Cherry 1979) and adjusted with the result of aquifer properties from the monitor wells. The computed potentiometric heads were compared with the observed heads in order to get acceptable results. The variation of aquifer parameters during model calibration was adopted in the range of standard values from Freeze and Cherry (Freeze and Cherry 1979). The final values were in the acceptable range.

6.4.4. Boundary condition

The general head boundary (GHB) is head-dependent recharge or discharge across an aquifer boundary. Proper boundary conditions were defined for mathematical computation according to the potentiometric head distribution along the boundary of the model. The general head values of the hydrographs from observation borehole logs along the model domain boundary were selected for GHB. Specifically, the GHB conditions were defined only to the Huai King Formation, basement formation and free flow in the pumping well PA12B (Figure 6.8). The increase in heads is not due to increasing recharge rates from the regional recharge zones during the observation period. There is no significant influence of regional groundwater on the head of the study area because the model was focused on the basement formation underneath a very thick layer of the claystone that consider as aquitard zone. The hydrology of the model (study) area is not related to the regional flow patterns because below the basement formation is bedrock with consider as aquitard. There is no flow due to recharge, but there is a flow due to discharge caused by wells.

Table 6.3 Modeled hydraulic parameters (after calibration).

Description	k_h	k_v	k_h/k_v	S_s	S_y	Porosity
	m/s	m/s	-	1/m	-	-
Claystone1	1.00×10^{-07}	1.00×10^{-08}	10	0.0093	0.001	0.1
Claystone2	1.00×10^{-07}	1.00×10^{-08}	10	2.4×10^{-05}	0.01	0.1
Huai King1	1.16×10^{-06}	1.16×10^{-07}	10	2.4×10^{-05}	0.01	0.1
Argillite1	5.78×10^{-06}	5.78×10^{-07}	10	5.30×10^{-08}	0.001	0.1
Argillite2	1.57×10^{-06}	1.57×10^{-07}	10	7.00×10^{-06}	0.001	0.1
Limestone	5.787×10^{-05}	5.79×10^{-06}	10	5.60×10^{-07}	0.001	0.1
Fault1	1.00×10^{-09}	1.00×10^{-10}	10	0.0001	0.001	0.1
Huai King2	1.70×10^{-08}	1.70×10^{-09}	10	0.0001	0.02	0.1
Fault2	1.00×10^{-04}	1.00×10^{-04}	1	0.0001	0.02	0.1

Notes: k_h is horizontal hydraulic conductivity, k_v is vertical hydraulic conductivity, S_s is specific storage, and S_y is a specific yield.

6.4.5. Initial head

The starting piezometric heads of all layers were specified as +300 meters above mean sea level. The values of starting head were assigned according to the starting head from the past research in 1994 as illustrated in Figure 6.9 (Dames and Moore 1998). This procedure is conducted by steady state calibration simulation. The computed results of piezometric heads from steady state calibration were applied as starting piezometric heads for the transient calibration for both modeled calibration and prediction. Figure 6.9 shows that groundwater from the northeast and western sides of the model area seem to be recharging the mine site. These groundwater zones with high potentiometric surfaces provide the upward movement underneath the mine pit.

6.4.6. Model simulation

Model simulation was operated using the Modflow package in order to examine the groundwater flow behavior of the layer comprised of limestone in the basement formation in the C1 pit. The simulations divided into two steps such as calibration and prediction. Specifically, steady state and transient simulation were adopted for

groundwater modeling based on the available input data from the conceptual model.

6.4.7. Observation well of the groundwater model

Observation wells were used for calibrating the model both steady state and transient conditions. This calibration was carried out by using the potentiometric head distribution of 12 observation wells within the model domain as illustrated in Figure 6.8 and Table 6.4. The average value of potentiometric heads from the observation wells was utilized for the steady state calibration. On the other hand, the transient calibration was operated by using the variations of potentiometric heads over time. The role of theses observation wells was to match the observed head and the computed head around the model boundary. Deep observation wells have been established since 1989 in the critical areas of the floor heaving effect to draw down high water pressure of local sand aquifers and major aquifer zones in limestone. The observation wells outside the mine area are referred to indicate the regional flow.

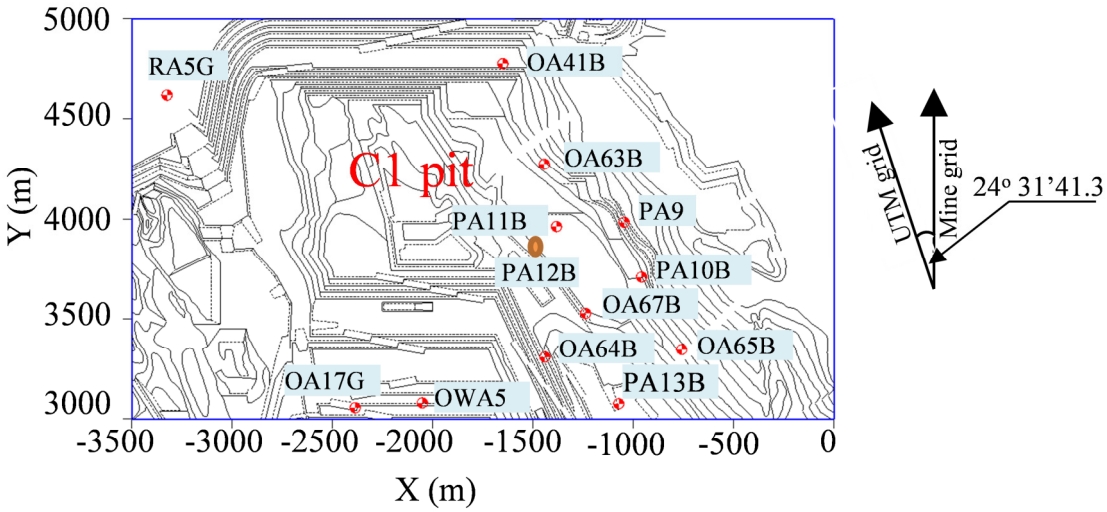

Figure 6.8 Observation wells used in the model calibration for steady-state and transient condition, pumping well (PA12B), and mining plan in 1998 used as background.

Table 6.4 The formation lithology of observation wells.

ID	Formation Lithology		
PA9	Limestone	OA17/2G	Sandstone
PA10B	Limestone	OA64B	Limestone
PA11B	Limestone	OA41B	Limestone
PA13B	Limestone	OA63B	Limestone
OWA5	Limestone	OA65B	Limestone
RA5G	Argillite	OA67B	Limestone

6.4.8. Model calibration

In order to assign the hydraulic properties from the initial model parameters, the calibration is adopted to process the initial model parameters. Those parameters for the calibration were hydraulic properties, and boundary conditions to obtain a suitable agreement between the computed and observed results of the groundwater flow system (Hanna et al. 1994).

The model calibration was achieved both for the steady state simulation and transient simulation. Specifically, the calibration is the process of modifying or improving the input data to reach the acceptable agreement between the model simulation and the observed data in groundwater flow system (ASTM 1996). Hence, the aim of calibration is very important for the model simulation to reach the suitable approximation of real and computed head distribution of the C1 pit. The trial and error were operated until the acceptable results were met for all calibrations.

The model calibration was assessed using the specified statistical criteria such as (i) high magnitude of R^2 values, (ii) low value of root mean square error, and (iii) low percentage value of relative root mean square error.The formula of root mean square error (RMSE) and relative root mean square error (RRMSE) (Moriasi et al. 2007) are shown in Equation (6.1)–(6.2) below:

$$\mathrm{RMSE} = \sqrt{\frac{1}{n}\sum_{i=1}^{n}(Y_i - X_i)^2} \tag{6.1}$$

$$\mathrm{RRMSE} = \frac{100}{\overline{X}_i}\sqrt{\frac{1}{n}\sum_{i=1}^{n}(Y_i - X_i)^2} \tag{6.2}$$

where Y_i and X_i are the predicted and observed values, respectively; $\overline{X}_i$ is the observed mean value; and n is the number of samples.

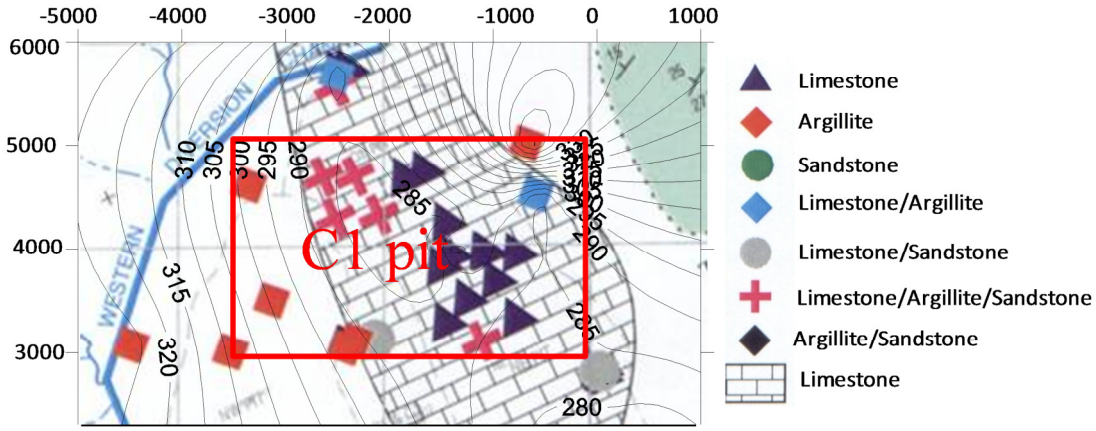

Figure 6.9 Initial head condition of Mae Moh mine in 1995 (Courtesy of Electricity Generating Authority of Thailand, EGAT).

6.4.9. Steady-state calibration

The steady state calibration was performed to balance the observed potentiometric head distribution by presuming that there is no pumping condition. The potentiometer heads of each observation were averaged for steady state calibration. Steady state model calibration was conducted to obtain starting head for the transient model calibration. Steady state calibration was successfully accomplished by adjusting the input aquifer parameters and boundary conditions using several trial and error methods.

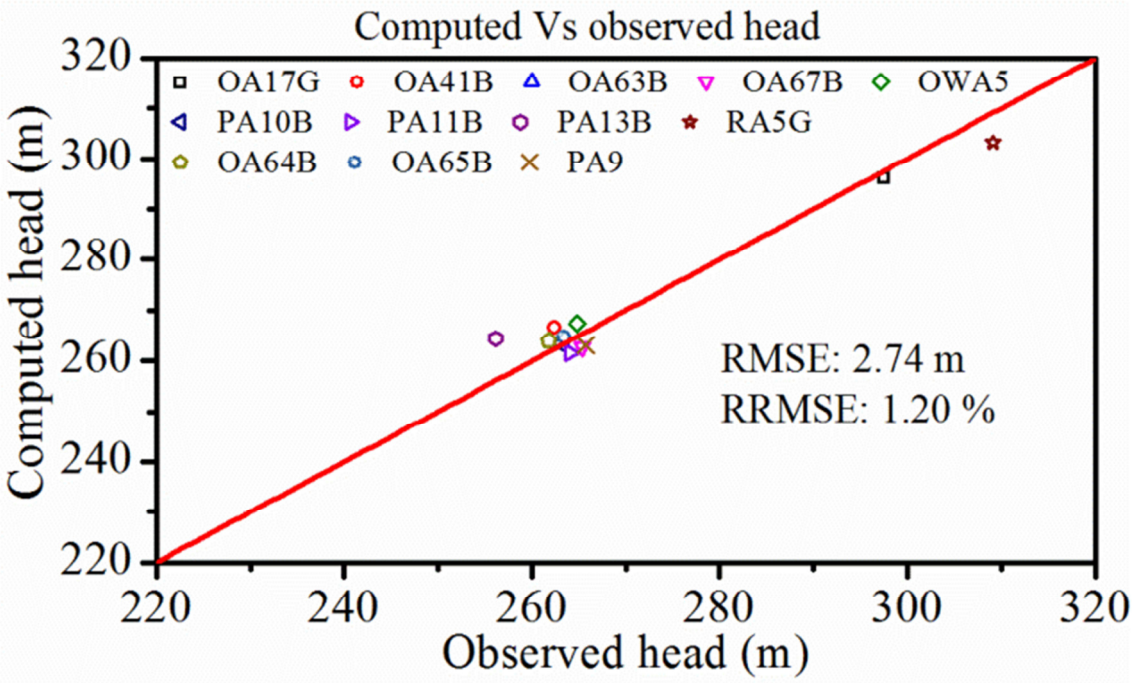

Figure 6.10 Groundwater flow modeling: Steady-state calibration.

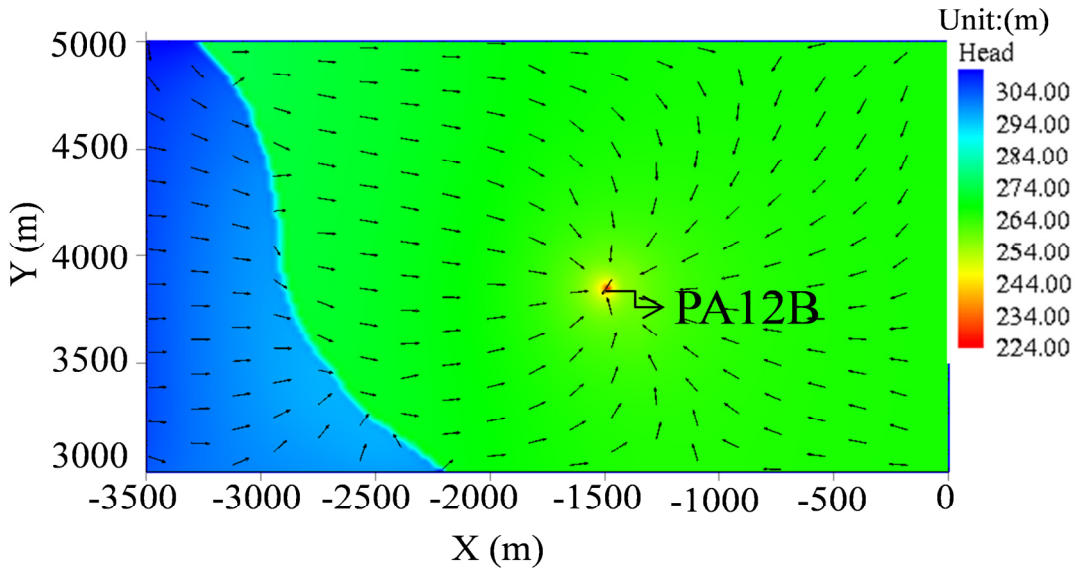

Figure 6.11 Steady-state simulation of head distribution on top limestone layer.

Figure 6.10 demonstrates the scatter plots between the computed and observed head values. The observed heads were on the x-axis, while the computed ones were on the y axis. Each of the scatter points on the x-axis depicts the potentiometric heads from the

observation good data. The points that represent the best calibration should be in a minimum level of scattering. This implies that the point should be neighbored to the diagonal line of the perfect fit through the origin. The result reveals that the computed heads are in an acceptable agreement with the observed heads as the data points were almost located on the diagonal line, having RMSE=2.74 m and RRMSE= 1.20%. The result of potentiometric head distribution on the top limestone layer obtained from the steady-state calibration is presented in Figure 6.11. The potentiometric head varies from 224 m to 310 m. The simulated groundwater flow direction is from the northwest toward the center of the basin. The potentiometric head is very low around the pumping well (PA12B).

6.4.10. Transient Calibration

Even though the steady state calibration could be used in modeling practice, a transient calibration should be conducted because groundwater flow behavior is varied by nature and frequently by human activities. Thus, the transient calibration must be operated after the steady state calibration to obtain practical model simulation.

The computed heads were compared with the observed heads during transient calibration for 365 days. Also, the trial and error method were operated to achieve the model in order to minimize the difference between the computed and observed heads. At this process, the aquifer parameters were adjusted within an acceptable range. Some input parameters were not adjusted at the same time for the model simulation as they may affect the model simulation. The prediction might not able to identify to reach the final result. As mentioned, the computed head distributions from steady state calibration were used as the starting potentiometric heads for transient calibration. As shown in Figure 6.12, the transient calibration was successfully met the requirement of statistical criteria with RMSE=5.317 m and RRMSE=2.05%. Hydrographs of the observations wells display an acceptable agreement between the observed and computed potentiometric head distribution during the simulation period of 365 days. The computed and observed heads were slightly different because the input aquifer properties were slightly different from the actual properties that are very difficult to determinate precisely.

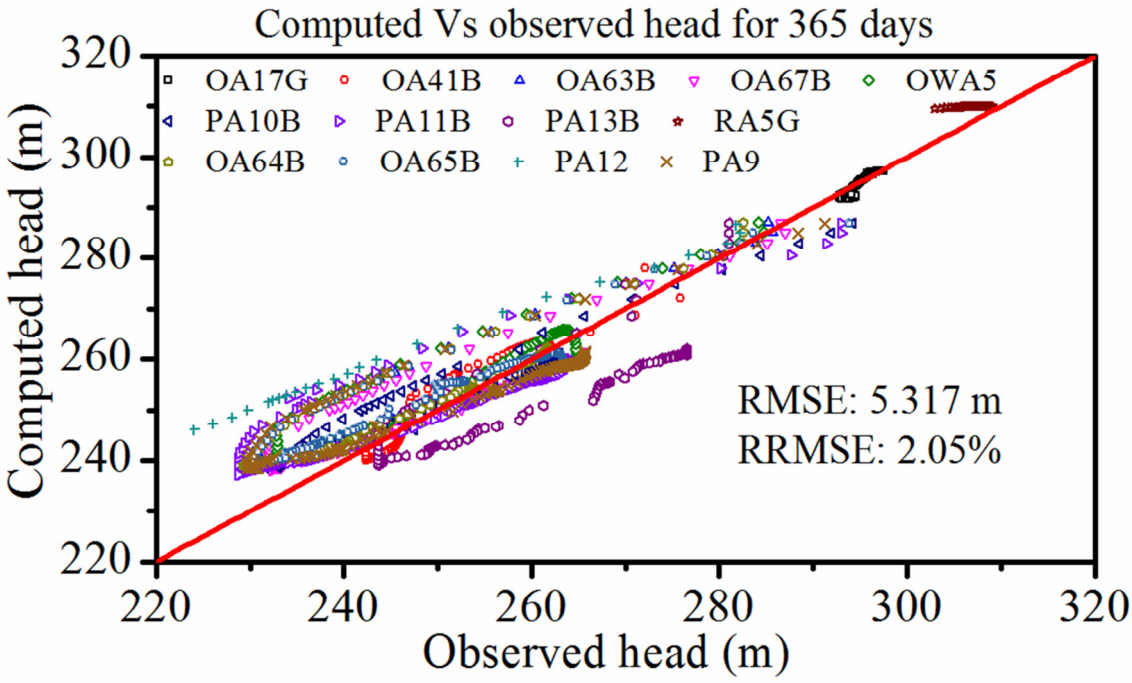

Figure 6.12 Groundwater flow modeling: Transient calibration.

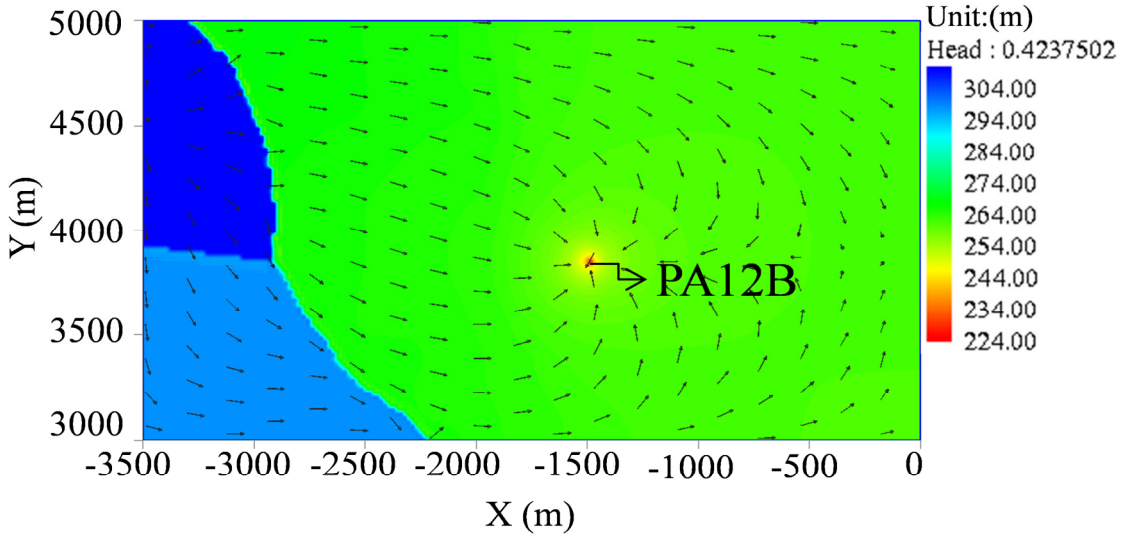

Figure 6.13 Transient simulation of head distribution for the first stress period (1 day) on top limestone layer.

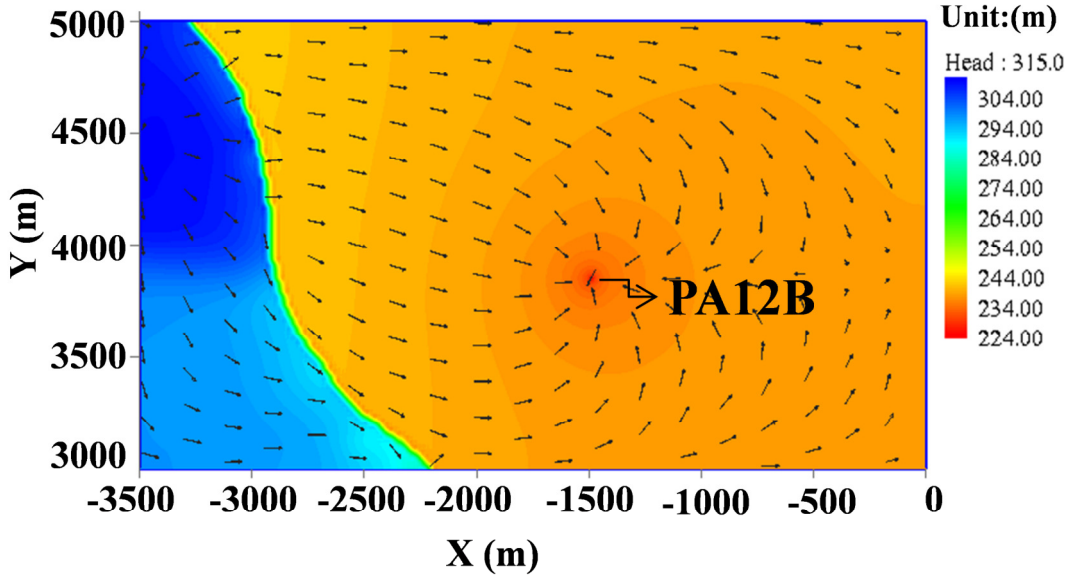

Figure 6.14 Transient simulation of head distribution in 310 on top limestone layer.

Figure 6.13–Figure 6.14 illustrates potentiometric head distributions in the basement formation (top of limestone) for the transient calibration for one year. The pumping well (PA12B) was used to lower the pressure at C1 pit to open the value of observation head. The pumping state was starting from the first day until 150 days then the pressure was recover until 365 days as shown in Figure 6.15.

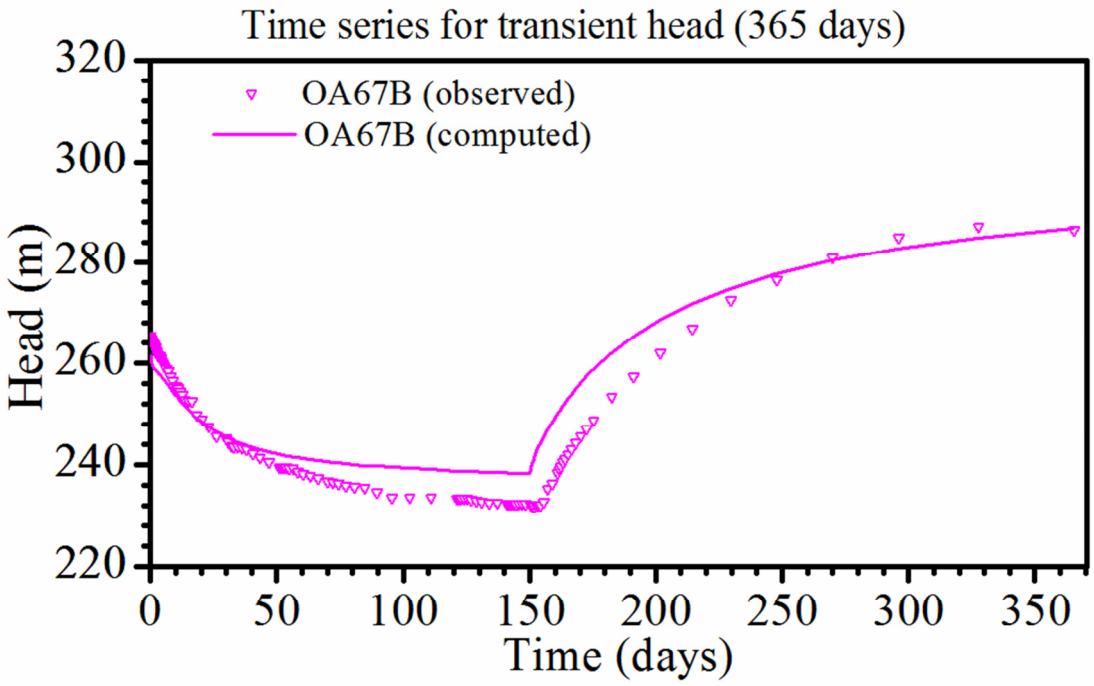

Figure 6.15 Time series for transient head calibration

6.5. Groundwater flow modeling for Mae Moh basin

Because the boundary head of C1 pit was determined by monitoring well around the model boundary, there is a limitation to get the correct boundary condition. For this reason, the groundwater modeling of the Mae Moh basin is needed to take into account for precise boundary condition. The Mae Moh basin is located in Lampang province in North Thailand, covered an area of more than 32 km^2 as displayed in Figure 6.16.

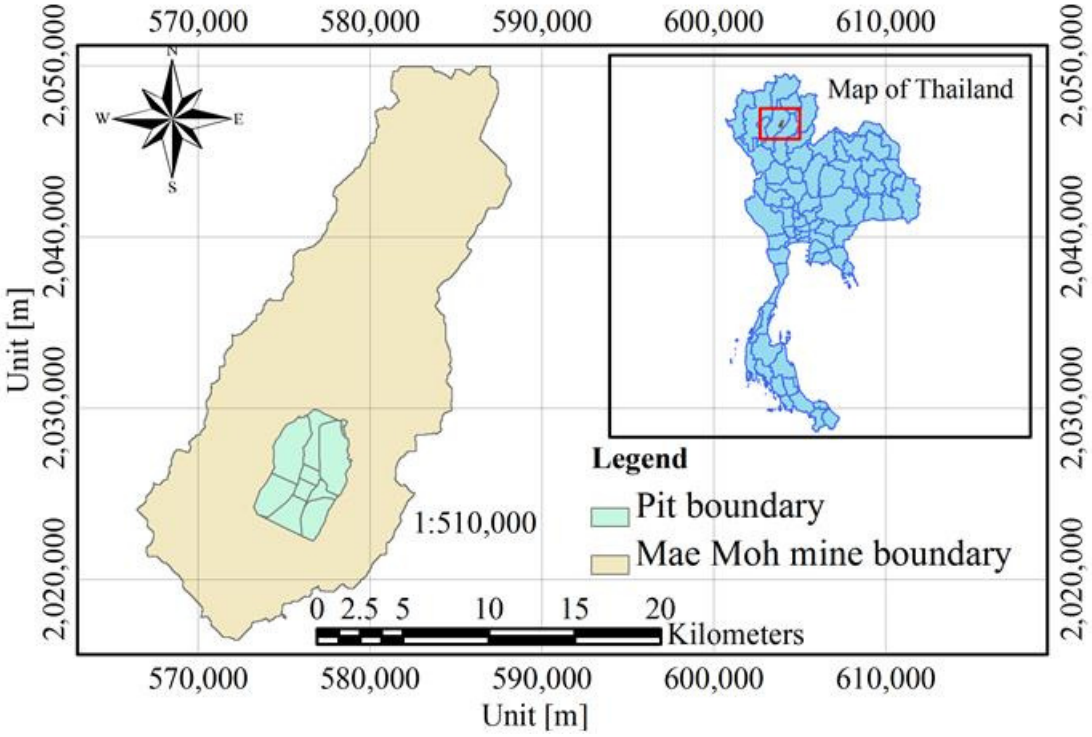

Figure 6.16 Location of Mae Moh basin (reproduced Electricity Generating Authority of Thailand, EGAT).

6.5.1. Conceptual model

A conceptual groundwater model was created as a basic graphical representation of the complex natural aquifer system within the Mae Moh basin. The elements of the conceptual model included defining the extents and characteristics of the aquifer system and developing an understanding of groundwater flow directions, sources, and sinks. The conceptualization took into consideration the overall objective of the model, the schedule and resources for reaching the objective, and the available hydrogeologic data.

The model area covers the whole Mae Moh basin including the open pit mine in Mae Moh basin as illustrated in Figure 6.17. The basin is bounded on east and west by steep rugged sub-parallel mountain ranges. In the north, the basin is enclosed by north east trending mountain range. Surface of these ranges mainly consist of Triassic limestone. The southern boundary of the basin is not enclosed and is formed by flat lying Pleistocene basaltic lava.

The original ground surface of the Mae Moh basin is flat to gentle rolling consisting of Tertiary rocks and overlying younger sediments. The average elevation of the mining area is about 330m, MSL. The groundwater flow in the Mae Moh Aquifer system converges from mountain ridges in east and west toward the flat area in the middle of the basin where most of the pumping occurs. The 3D stratigraphy of Mae Moh basin is shown in Figure 6.18.

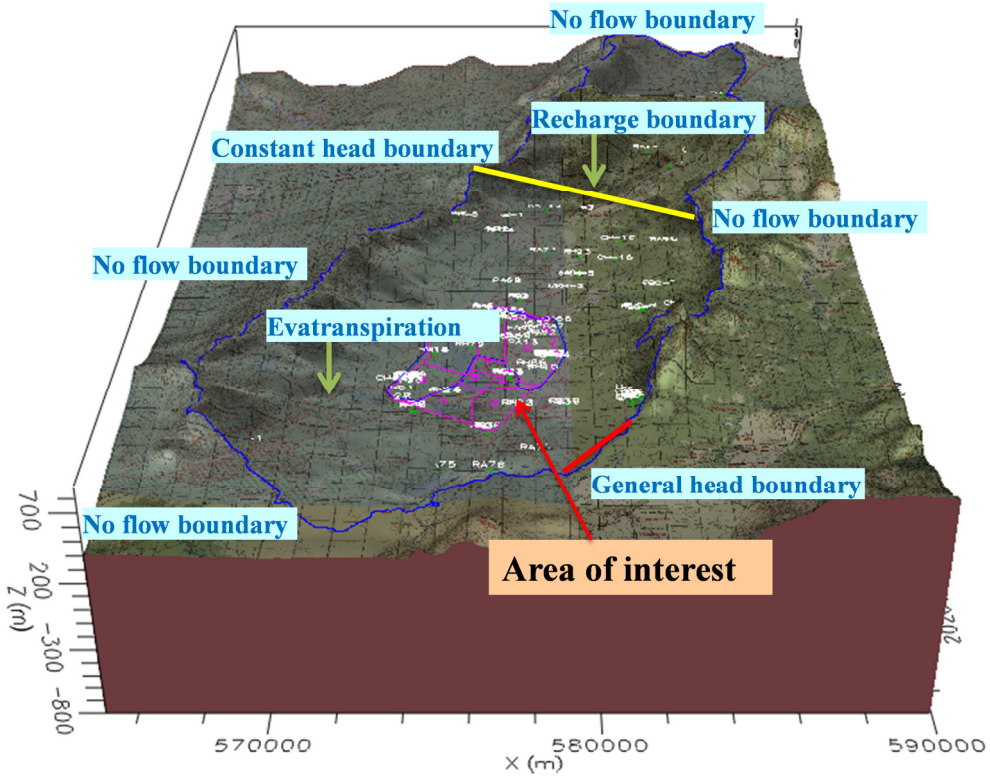

Figure 6.17 Conceptual model of Mae Moh basin

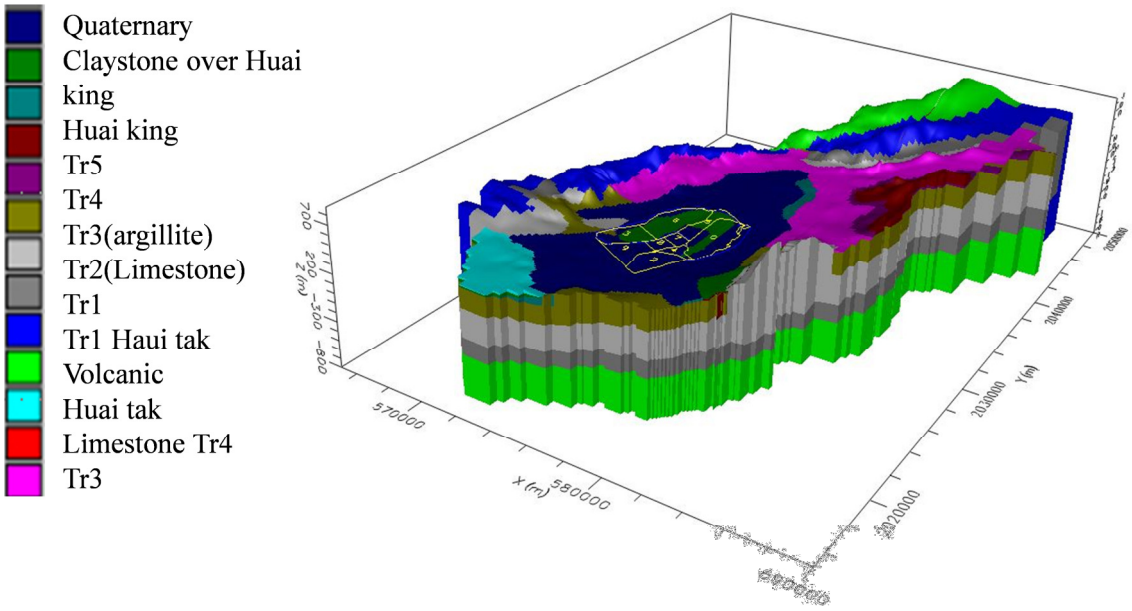

Figure 6.18 Model stratigraphy of Mae Moh basin

The conceptual model was developed with the following assumptions:

- The surficial aquifer was divided into zones of coarse material assigned with relatively high hydraulic conductivities and fine material attached with relatively low hydraulic conductivities.
- The Basement limestone aquifer was assigned a decreasing hydraulic conductivity with increasing depth.
- The groundwater flow direction of the basin has been assumed by considering the topography of the Basin and potentiometric head distribution within the mine area.

After completion of the construction of the conceptual model, appropriate modeling software has been selected, and the features of the conceptual model have been transferred to an input file that defines the mathematical model.

6.5.2. Model boundary

Constant head boundary

Appropriate boundary conditions were specified for numerical calculation based on the potentiometric head distribution along the perimeter of the Model domain. Considering

the constant head values of the hydrographs of observation boreholes along the perimeter of the model domain, constant head boundary conditions were assigned to the Huai King Formation and Basement formation.

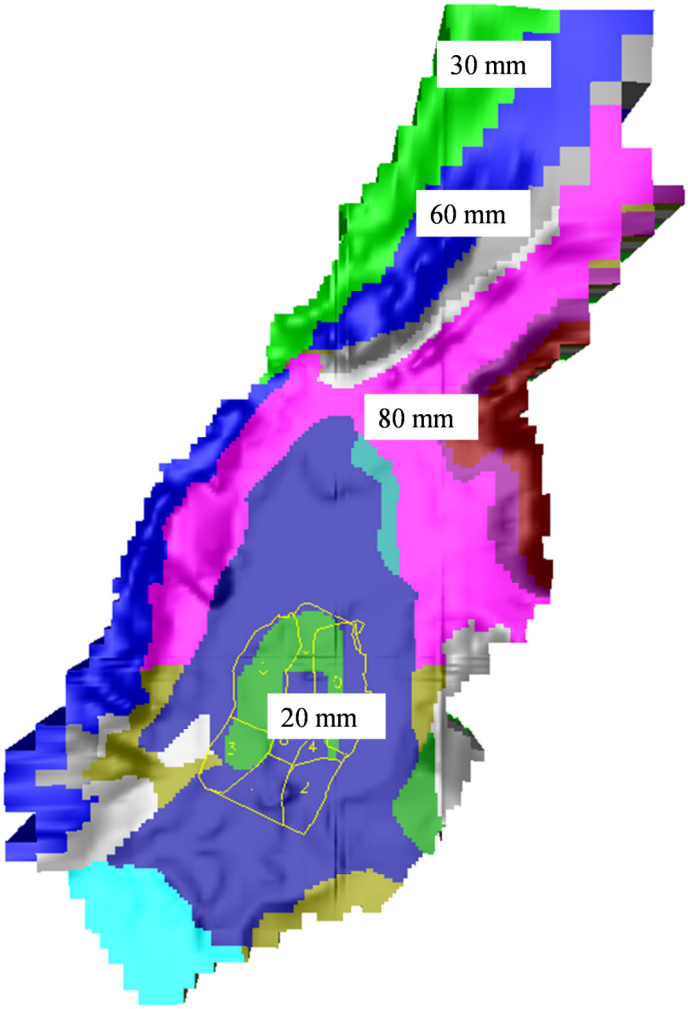

Figure 6.19 Recharge boundary.

Groundwater recharge

Groundwater recharge is considered from two sources, rainfall recharge that has been infiltrated into the ground, and water bodies within the model domain as illustrated in Figure 6.19. Rainfall recharge was simulated in the model and assumed that it was only infiltrated into the model in areas where no tertiary sediments are present. Hence, rainfall recharge was assigned to the area of 342.77 km^2.

Constant head boundary

The general head boundary (GHB) is head-dependent recharge or discharge across an aquifer boundary. Proper boundary conditions were defined for mathematical computation according to the potentiometric head distribution along the boundary of the model. The general head values of the hydrographs from observation borehole logs along the model domain boundary were selected for GHB.

6.5.3. Steady sate calibration

Calibration is the process of adjusting or altering model input parameters to achieve a desired degree of correspondence between the model simulation and the actual groundwater flow system. For this reason During model calibration, the aim was to achieve the best match between actual and modeled groundwater head distribution of the Mae Moh basin. Model calibration was performed for steady state condition.

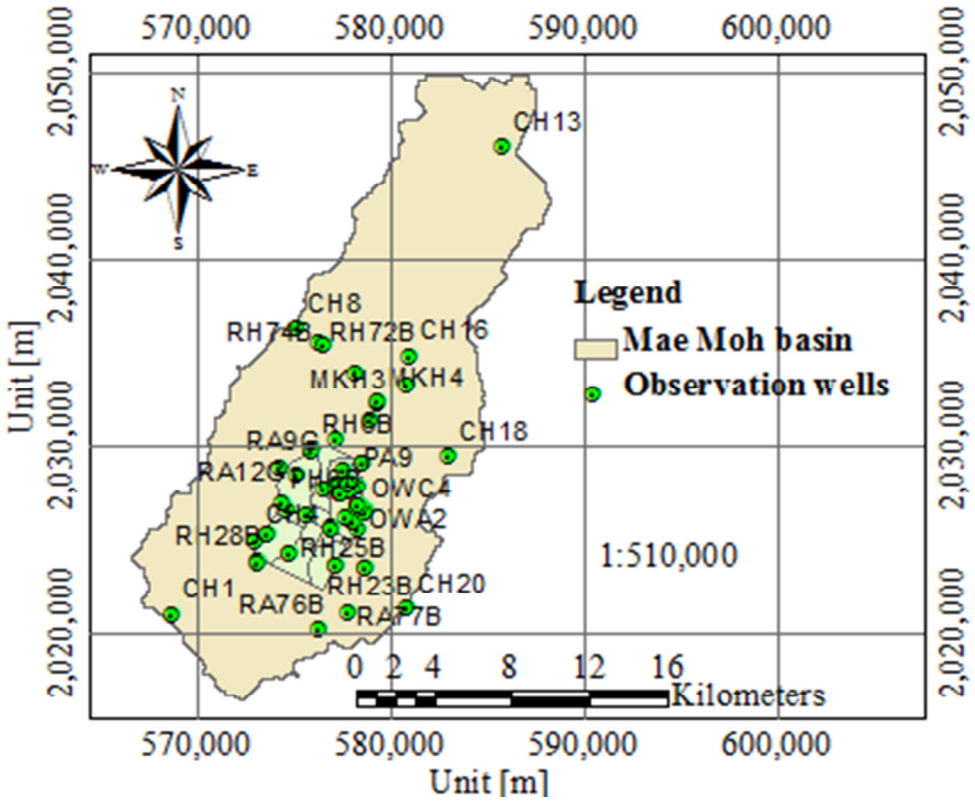

Figure 6.20 Observation well in Mae Moh basin.

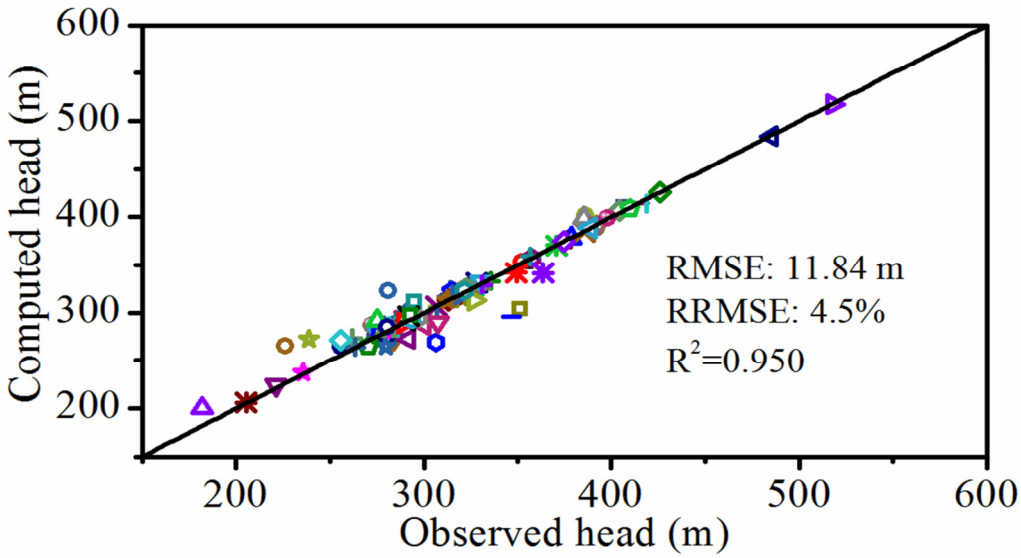

Figure 6.21 Steady-state calibration in Mae Moh basin.

Steady state model calibration was carried out prior to the transient model calibration. This was conducted by using the potentiometric head distribution of 87 observation wells during the first half of 1994, within the basin as shown in Figure 6.20. The initial potentiometric heads for the steady state calibration were assigned according to the initial head of Mae Moh basin in 1994. Steady state calibration was achieved by altering the input aquifer parameters and boundary conditions by trial and error method until model simulated observed data into a satisfactory level. During steady state calibration computed potentiometric heads were compared with the observed heads as displayed in Figure 6.21. Then the aquifer parameters were modified within a reasonable limit by trial and error method to minimize the difference between the observed and calculated hydrographs. The value of input parameters of the groundwater modeling of Mae Moh mine is shown in Table 6.5.

Figure 6.21 demonstrates the scatter plot between computed and observed head values.

The observed heads were on the x-axis, while the computed or heads were on the y axis. Each of the scatter points on the x-axis depicts the potentiometric heads from the observation good data. The points that represent the best calibration should be in a minimum level of scattering. This implies that the point should be neighbored to the diagonal line of the perfect fit through the origin. The result reveals that the computed heads are in an acceptable agreement with the observed heads as the data points were almost located on the diagonal line, having RMSE=11.84 m and RRMSE= 4.5%. The computed potentiometric head distribution on the top of the basement formation resulting from steady state calibration is displayed in Figure 6.22. The computed potentiometric head varies from 200 m to 600 m.

Table 6.5 Modeled hydraulic parameters (after calibration).

	Before calibration				
	k_h	k_v	S_s	S_y	Porosity
Layer	m/d	m/d	1/m	-	-
Quaternary	2.9×10^{-5}	2.9×10^{-6}	2×10^{-5}	0.2	0.25
Claystone over Huaiking	1.29×10^{-5}	1.29×10^{-6}	2×10^{-5}	0.2	0.25
Huaiking	3.1×10^{-5}	3.1×10^{-6}	2×10^{-5}	0.2	0.25
Tr5	1.5×10^{-5}	1.5×10^{-6}	2×10^{-5}	0.2	0.25
Tr4	1.2×10^{-5}	1.2×10^{-6}	2×10^{-5}	0.2	0.25
Tr3(argillite)	2.25×10^{-5}	2.25×10^{-6}	2×10^{-5}	0.2	0.25
Tr2(Limestone)	2.5×10^{-4}	2.5×10^{-5}	2×10^{-5}	0.2	0.25
Tr1	3.8×10^{-5}	3.8×10^{-6}	2×10^{-5}	0.2	0.25
Tr1 Hauitak	1.4×10^{-5}	1.4×10^{-6}	2×10^{-5}	0.2	0.25
Volcanic	1.2×10^{-5}	1.2×10^{-6}	2×10^{-5}	0.2	0.25
Huaitak	1×10^{-5}	1×10^{-6}	2×10^{-5}	0.2	0.25
Limestone Tr4	0.0115	0.0115	2×10^{-5}	0.2	0.25
Tr3	1.5×10^{-5}	1.5×10^{-6}	2×10^{-7}	2×10^{-5}	0.25

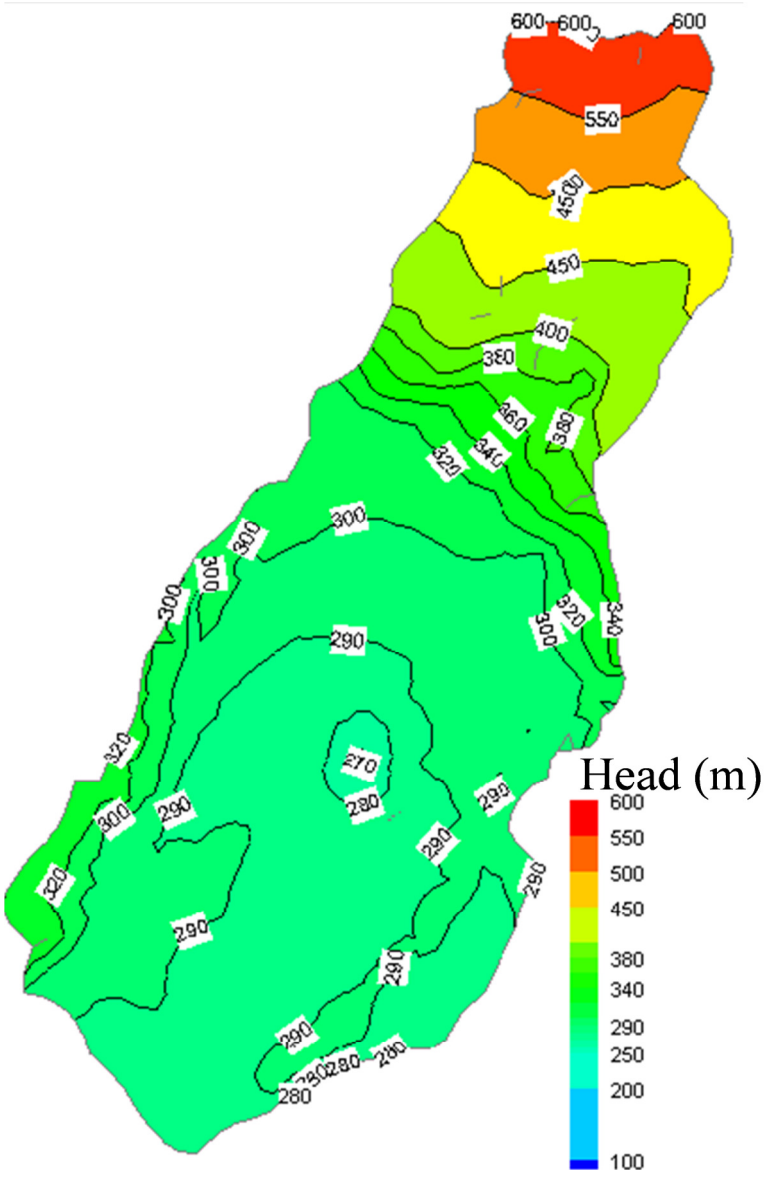

Figure 6.22 Steady state simulation in Mae Moh basin.

6.6. Water treatment plant

Arsenic (As) is a toxic metal that naturally appears in groundwater as oxyanion compounds. The arsenic removal mechanism is explained based on the report/data of the Mine Environmental Management Department, EGAT [9]. The water treatment plant utilizes the chemical process to remove the existing arsenic in the underground water. The process starts from the pumping of underground water from the collecting sump to the holding pond and then pumping water to rapid mixing tanks for the pH

adjustment process using sodium hydroxide, followed by the reaction tank where the following equations react the ferric chloride (FeCl3). Note that the pH of Mae Moh underground water is usually around 7.5-8.5; for this reason, NaOH is practically unused in the water treatment process of Mae Moh mine.

$$FeCl_3 + 3(H_2O) \rightarrow Fe(OH)_3 + 3H^+ + 3Cl^- \quad (6.3)$$

$$Fe(OH)_3 + HAsO_4^{2-} + 2H^+ \rightarrow FeAsO_4 \cdot 2H_2O + H_2O \quad (6.4)$$

After the process, the water will be flowed out to the slow mixing tanks to collect the precipitated arsenic compounds before flowing into the sedimentation tanks to collect the sediments deposited at the bottom of the tanks. The water will be pumped to sludge thickening tanks and then pumped to sludge drying beds. The clear water on the upper portion will be spilled over the system for diversion to the outsides. Details are described in Table 6.6 and Figure 6.23. Though amount of surface water seasonally changes, there is no influence of seasons to the running condition of the water treatment facility as the water is pumped from the sump and keeps in the holding pond before feeding water to the water treatment plant. The water treatment plant is fully operated. For this reason the amounts of ferric chloride (0.01% by volume of water treatment), arsenic concentration or treatment efficiency are almost constant all year round.

Table 6.6 Performance of water treatment plant of Mae Moh lignite mine (as of 2013) (Sourced from the data of Mine Environmental Management Department, EGAT).

Maximum capacity	12,000 m^3/day
Amount of ferric chloride	1,000 kg/day ($FeCl_3$ 40% w/w 1.8 m^3/day)
Dry weight of sludge	800 kg/day
Treatment efficiency	greater than 95%
Cost of treatment	3 Baht/m^3 (about 9 JPY/m^3 or 0.10 US$/$m^3$)
Inflow of arsenic	200-500 μg/L
Outflow of arsenic	less than 10 μg/L

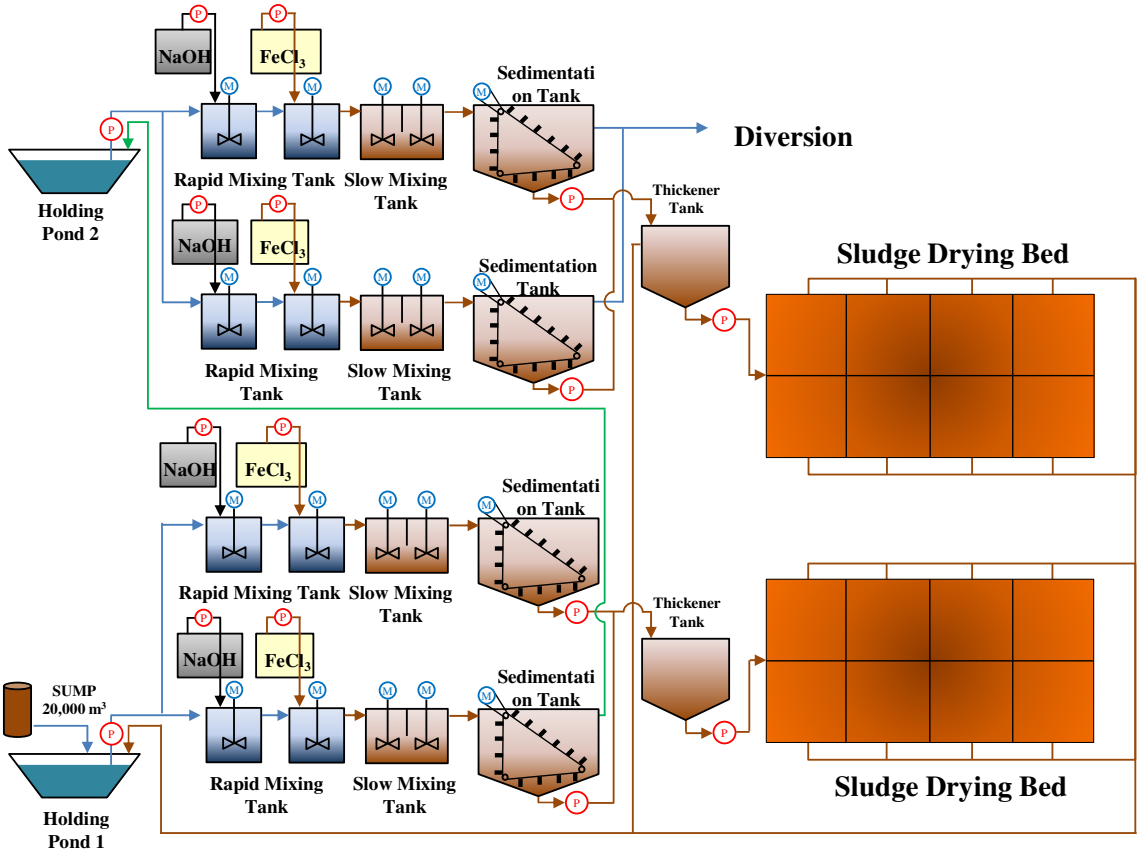

Figure 6.23 Flow diagram of water treatment plant of Mae Moh lignite mine (as of 2013) (Reproduced from the chart of Mine Environmental Management Department, EGAT).

6.7. Conclusions

The study of underground mining resulting from field investigation was reported. The study reveals that the underground water influences the magnitude and extent of strata depressurization, which have the potential impact on the Mae Moh area. The monitoring program of underground water is necessary to preserve long-term usage of the lignite mine. The analysis of floor heaving was carried out in the next chapter, but in the paper we aimed to report not only the groundwater modeling but also the groundwater treatment plant. Further publication reporting the evaluation of floor heaving will refer to the groundwater modeling reported in this paper.

The treatment efficiency study showed that more than 95% of the arsenic can be successfully removed using ferric chloride. To make some water quality parameters

conformable to the Thai stream standard, the arsenic concentration remains below 10 μg/L after treatment. The arsenic removal process and the performance of water treatment plant at Mae Moh mine could provide assurance to the community that this potential risk has been minimized. In geotechnical engineering viewpoint, the site perfectly shows how stability can be linked to the water environment.

For general viewpoint, this site shows a good example of how the geotechnical engineering problem can be linked to the environmental engineering problem. Therefore, we can realize that a solution to one problem might cause another problem and engineers/experts in different fields are required to work together, share data and exchange opinions. The scope of this paper is to develop the 3D groundwater modeling for future planning, as well as the field report of water treatment plant. The water balance analysis to show the relationship of rainfall to the other major processes (runoff, infiltration, evaporation) in the basin and hence possible recharge to the groundwater should be considered for further study. In addition, the effect of the piezometric head upon removal of the overburden through mining over the years could also be considered for future research.

CHAPTER 7 FLOOR HEAVING ANALYSIS OF MAE MOH OPEN PIT MINE, THAILAND

7.1. Introduction

Situated in Lampang province, the Mae Moh open-pit lignite mine covered an area of more than 32 km^2. The Mae Moh mine is operated since 1955, considered as the one of the largest open pit lignite mines in Southeast Asia. The need of capacity supply in the region has been increased rapidly. For this reason, the lignite coal mine that located at deep subsurface is also increased. The groundwater problem at Mae Moh mine has drawn much attention because the mining excavation goes deeper; thus, detailed investigations of hydrogeological conditions are required. Many groundwater investigations are continuously conducted by EGAT to have a better understanding of the effect of deep excavation. The result shows there is the potential for groundwater flow from the basement formation when mining is deepened. This increasing of groundwater flow affects mining and creates the potential of floor heaving. For this reason, prediction of the groundwater flow behavior beneath the mine is very important and the most notable effects of groundwater and floor heaving.

7.2. Calculation of critical area

The information on the potential of floor heaving developed at deep open pit mine specially in the deep excavations is one of the most important source to design for future excavation planning and also to confirm the safety and to maintain the further excavation. Stability analysis is carried out to find the location of critical area in the center pit (C1) by considering the influence of the groundwater pressure. Stability analysis is calculated according to the groundwater modeling of pressure effect on deep open-pit mining against floor heaving at the Mae Moh Mine (2007-2015) by Touch et al. (2014). The model comprises of three aquifers and one aquitard. The model boundary was defined as 3.5 km × 2 km as displayed in Fig.1, which were split into 9 material types and grid cell of 100 rows, 190 columns, and 15 layers. The main formation concerned about groundwater effect is basement formation, which contains

limestone and argillite. Because 3D groundwater modeling was conducted based on the previous study of Pongpanlarp (2007), the model simulation and stability analysis were also started from 2007–2015. The factor of safety and floor heaving potential line were also calculated from 2007–2015. The principle of the calculation of factor of safety is based on Figure 7.1. The piezometric head, the thickness of the under burden were needed to be identified. Principally, the piezometric head of the basement in particular limestone were obtained from the 3D groundwater simulation from 2007–2015. Additionally, the thickness of the under burden was determinate from the surface elevation of the deep open-pit mine and the top elevation of the under burden (limestone). Finally, the factor of safety is calculated as shown below.

$$Factor\ of\ Safety = \frac{Resisting\ force}{Driving\ force} = \frac{\gamma_s h_s}{\gamma_w h_w} \tag{6.5}$$

γ_s = unit weight of limestone (20 kN/m^3)

h_s = thickness of under burden (m)

γ_w = unit weight of water (10 kN/m^3)

h_w = pressure head (m)

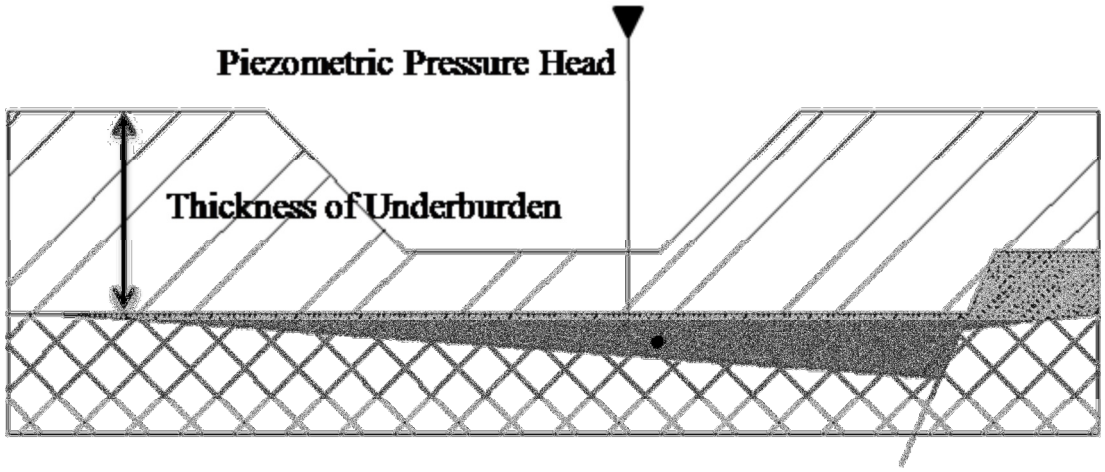

Figure 7.1 Schematic diagram of factor of safety

The floor heaving potential line is calculated for each cross-section of the model area. As an example, Figure 7.2 illustrates the potential of floor heaving in the critical area

for the year 2007 and 2015. In addition, the factor of safety was also examined for each cross-section. Upon the completion of the calculation of each factor of safety from each cross-section, the contour map of the factor of safety was computed as illustrated in Fig. 6 for 2015. The critical area is enlarging from time by time. Therefore, the dewatering process is needed to reduce the water pressure from limestone layer. New simulation with the artificial pumping wells will be conducted.

The critical area was calculated according to the mining plan in 2007 and 2015. Mine will be dumped back soon; not leave it as it is for the next 40 years. That is why a long-term condition is not considered. Figure 7.3– Figure 7.4 illustrate the mining plan of Mae Moh mine in the year of 2007 and 2015, respectively. When there is an increasing of the generating capacity, the large and deep excavation (more than 300m) to get sufficient energy resources are needed. Therefore, there is a decreasing of the overburden pressure on aquifer layer. Potential of floor heave by groundwater will occur. As the result, it is needed to control the groundwater considering the other problems.

The results of the calculation of the factor of safety for 2007 and 2015 are illustrated in Figure 7.5–Figure 7.6. The factor of safety was calculated for every cross section of the study area (C1 pit). The area that has the factor of safety less than 1 was identified.

- The critical area according to the 40-year power plant are:
  - ✓ In 2007: N35-N40, W10-W23.
  - ✓ In 2015: N30-N40, W10-W23.

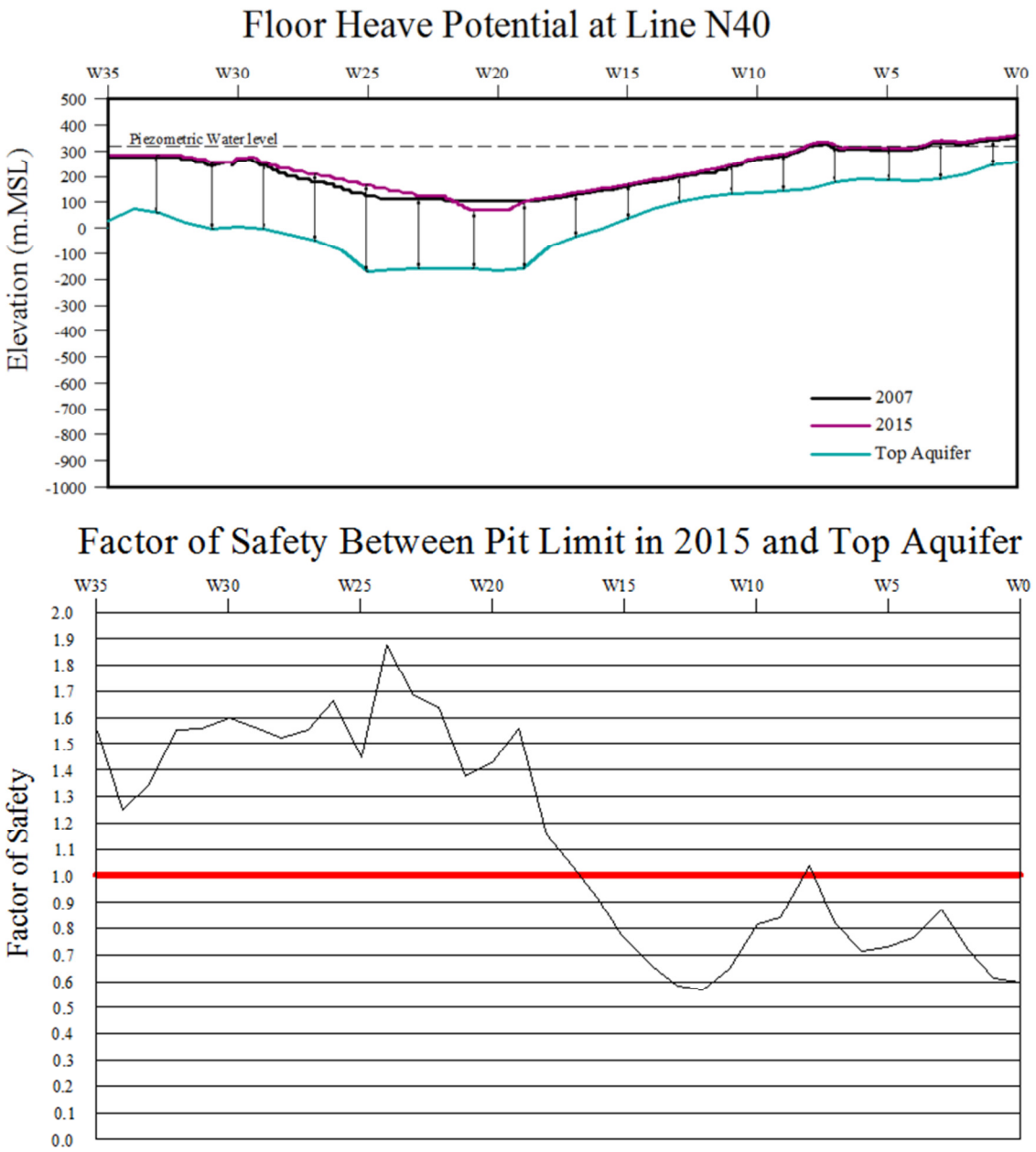

Figure 7.2 Cross-section along N40

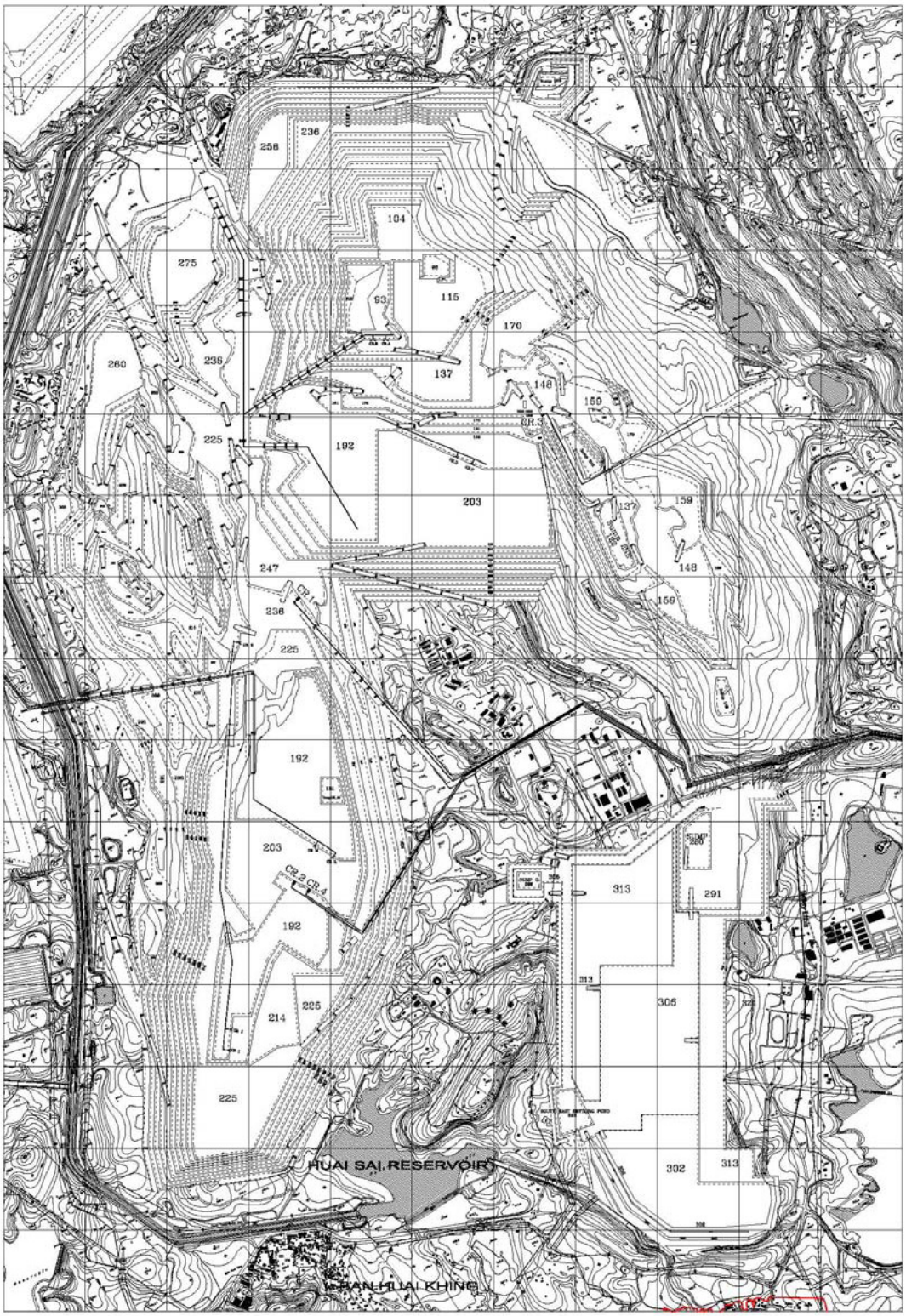

Figure 7.3 Mine Plan for Power Plant in 2007

Figure 7.4 Mine Plan for Power Plant in 2007

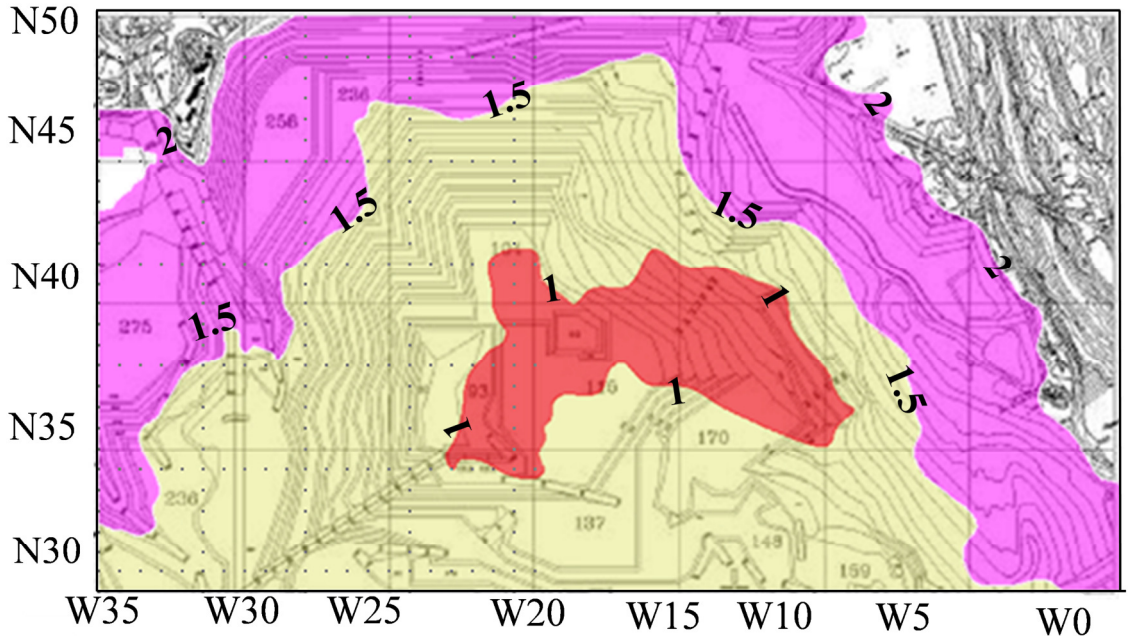

Figure 7.5 Boundary of critical area in C1 pit in 2007

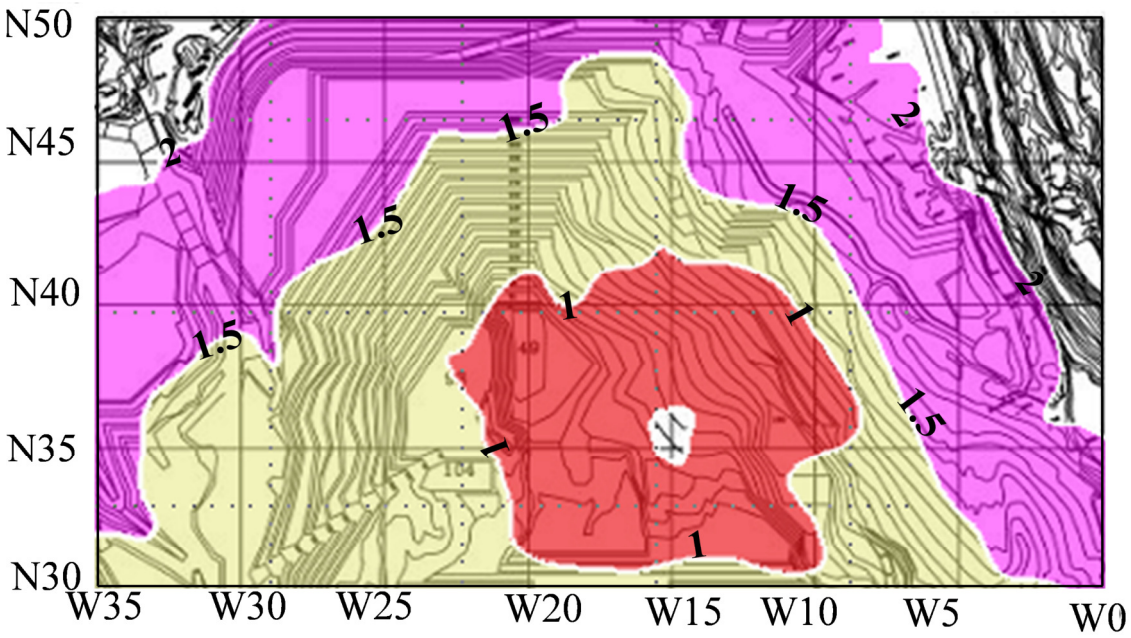

Figure 7.6 Boundary of critical area in C1 pit in 2015

7.3. Dewatering Plan

The dewatering is needed to be conducted to reduce pressure on the critical area that was already identified in the previous section. The prediction run result for the next 5 years (2007 to 2012), according to mine planning for 40 years power plant, has shown

that the critical area in the year 2007 will be in N35-N40, W10-W23 area based on mine grid, while the critical area in the year 2015 will be in N30-N40, W10-W23. Groundwater piezometric head required in the year 2007 will be + 200 m MSL, which will be the same in the year 2015. Minimum groundwater discharge rate required for the safety factor is greater than 1. Three pumping wells were installed in the critical area as shown in Figure 7.7 to reduce the water pressure from the deep aquifer in particular limestone layer.

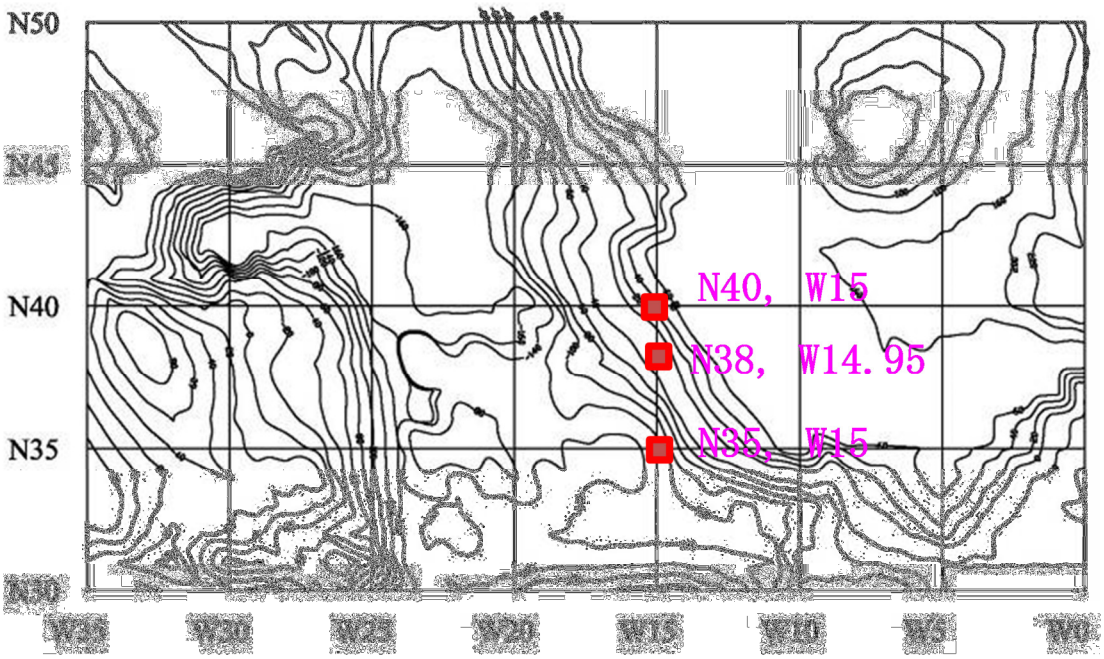

Figure 7.7 Pumping Location

Model pumping 8 years (2920 days) varies pumping rate

- Pumping rate 3,000 m^3/day/well (3 well = 9,000 m^3/day)
- Pumping rate 4,000 m^3/day/well (3 well = 12,000 m^3/day)
- Pumping rate 5,000 m^3/day/well (3 well = 15,000 m^3/day)
- pumping rate 6,000 m^3/day/well (3 well = 18,000 m^3/day)

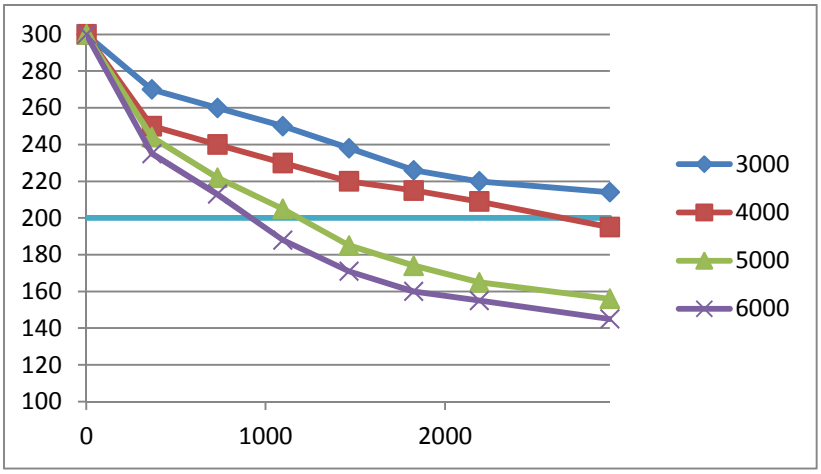

Figure 7.8 Prediction of Pumping Rate from Model

7.4. Conclusion

The main conclusions of this chapter follow:

- The critical area where ***the factor of safety <1*** were identified.
- The critical area according to the 40-year power plant are:
  - ✓ In 2007: N35-N40, W10-W23.
  - ✓ In 2015: N30-N40, W10-W23.
- For dewatering is 4,000 m^3/day/well (3 wells = 12,000 m^3/day)
- The groundwater modeling should be updated from time to time to monitoring the effect of the excavation.